

A Numerical Study on Design of Coastal Groins

S. Eslami^{1,2}, Leo C. vanRijn¹, D.J. Walstra^{1,2}, A.J. Luijendijk¹, M.J.F. Stive²

¹Deltares|Delft Hydraulics, Section Hydraulic Engineering (HYE), P.O.BOX 177, 2600 MH Delft, the Netherlands, TEL: + 31 (0)88 335 8273, fax : +31 (0)88 335 8582; email: Sepehr.EslamiArab@deltares.nl

²Delft University of Technology, Department of hydraulic Engineering, Chair of Coastal Engineering, Stevinweg 1, 2628 CN, Delft, the Netherlands TEL: +31 (0)15 2782811; email: D.J.R.Walstra@tudelft.nl

ABSTRACT

Numerical models become attractive means of study, when considering the limited knowledge and guidance on functional design of coastal groins. In the present article, a process-based 3D numerical model (Delft3D) is verified against two different datasets. For application on design of straight open (normal) groins, Badiei et. al. 1994 laboratory measurements, and in case of T-Head groins Ozolcer et. al. 2004 field measurements are considered. In case of normal groins, the model showed good agreement with the observations, hence, a design exercise and method has been developed. In case of T-Head groins, the model showed sensitivity to the numerical representation of the structure, while still satisfactory resemblance was perceived. Comparing to the present design rules, application of a numerical study is of crucial importance.

INTRODUCTION

Groins are popular means of coastal protection against erosion and are found along the coast worldwide, although according to CEM (Coastal Engineering Manual 2003), “they are probably the most misused and improperly designed of all coastal structures”. Groins, albeit having a simple concept, their interaction with the beach is complex, and existing functional design guidance is limited. The recent developments in numerical modeling, has provided better tools to study the hydrodynamic and morphological phenomena in presence of groins to find more sophisticated design approaches. Usage of straight open groins has shown a variety of failure mechanisms worldwide. Therefore, as an alternative, T-Head groins seem to be showing more promising behavior when coastline protection/generation is of highest priority. Examples of successful T-head groin fields can be found in Argentina (personal contact Leo vanRijn) and Turkey.

A groin simply blocks part of alongshore sand transport and causes it to accumulate in a fillet on the groin's up-drift side. This accumulation reorients the shoreline and reduces the angle between the shoreline and the prevailing incident wave direction. The reorientation reduces the local rate of alongshore sand transport to produce accumulation and/or redistribution of sand up-drift of the groin. Wave diffraction causes reduced wave energy in the lee of the groins relative to the mid-compartment, mean water-level setup gradients, and setup induced currents behind the groin. These contribute to complex current circulation patterns that move sediment alongshore and offshore along the lee side of the groin (Dean 1978). The

strength of these internal current patterns depends on groin plan-form geometry, but also on groin cross-sectional elevation and permeability across the surf zone. For normal wave incidence, the groin system can create strong local currents and rip currents, which add to the offshore movement of beach material during more extreme situations; therefore, the expectation is by construction of T-Head groins, and reducing wave transmission and increasing wave asymmetry, cross-shore sediment transport is interrupted.

Hanson & Kraus 1989, using GENESIS (a coastline model) introduced four key parameters in functional design of groins:

1. Groin Bypassing; depth at groin tip/breaking wave height (or the ratio between the length of the groin and the width of the surf-zone L_g/L_b)
2. Permeability factor; representing groin elevation and groin porosity
3. Ratio of net transport/gross rate
4. Ratio of distance between the groins over the groin length; a value of 2-3 is proposed by SPM (Shore Protection Manual 1984) for the proper functioning of shore normal groins.

However, in such models, a realistic distribution of long-shore current and sediment transport across the surf zone, cross-shore sediment transport, beach profile shapes with bars and troughs and other phenomena are missing. Therefore, with modern process-based two/three-dimensional morphological models, better understanding of groins for purpose of functional design is envisaged.

Description of the Model

In this study, the process-based model Delft3D is employed for hydrodynamic and morphological simulations. The model includes various modules such as, Delft3D-FLOW for 2 or 3-dimensional simulations of flow and sediment transport and Delft3D-WAVE for wave propagation simulations that runs online with Delft3D-FLOW providing wave forcing for the flow module.

Delft3D-WAVE runs the phase averaged spectrum model SWAN (see Holthuijsen et al. 1993). SWAN, in fact, solves the conservation of action density over the wave grid. Usually, the spectrum wave models determine the evolution of the action density $N(\bar{x}, t; \sigma, \theta)$ in space, \bar{x} , and in time t . Where, σ is the frequency (as observed with a frame of reference moving with current velocities) and θ is the wave direction normal to the wave crest of each spectral component. The action density is a realization of energy density $E(\sigma, \theta)$, while $N = E / \sigma$. The advantage of the action density is based upon its conservation during propagation in the absence of ambient current, whereas energy density is not (Whitman, 1974).

Delft3D-Flow module solves the non-linear unsteady shallow water equations derived from the three dimensional Navier-Stokes equations for incompressible free surface flow, under the Boussinesq assumption, in two (depth averaged) or in three dimensions. This system of equation consists of horizontal equation of motion, continuity equation and conservation of constituent (in our case sediment). In Delft3D-Flow, the 3D turbulent eddies are computed by means of an algebraic $k-\epsilon$ turbulence model, where, k is the turbulent kinetic energy, and ϵ is the dissipation rate of kinetic energy. To account for sediment transport, this module computes the

sediment transport and its gradients using Vanriijn 2004 formulation (see also van Rijn 2006). The advantage of this formulation is the decomposition of different sediment transport components. These components are bed load and suspended load, while each of them has a wave related and a current related contribution. The approach provides useful calibration tools (a coefficient for every component) to adapt different physical conditions (for further information see Lesser et al. 2004).

VALIDATION OF THE MODEL IN CASE OF STRAIGHT OPEN GROINS

Badiei et al. 1994 employed a series of mobile bed process physical models to investigate effects of groins on evolution of shore morphology under attack of waves approaching with an angle towards the shoreline. Their observations have been used to verify the model performance in application of straight open groins with grain size of $D_{50}=0.2\text{mm}$. The tests start with a straight beach and a constant slope of 1:10 exposed to waves with $H_s=8\text{cm}$, $T_p=1.15\text{sec}$ and an angle of 11.6 degrees relative to normal to the coast for 4 hours to get some bar and trough in cross-shore direction (NT1 test). After 4 hours, the basin is surveyed to measure the beach response and the groins with different lengths are placed afterwards (called NT4 test when $L_g/L_b=1.4$ and NT5 when $L_g/L_b=0.8$). The experiments continue for another 8 hours in presence of groins. A similar approach is considered in the numerical verification of this study.

The primary tests showed that the model was not capable of simulating in the laboratory scale and a scale-up to prototype was needed. The scaling up formulation of van Rijn 2009 is used for this purpose and everything is scaled up for 25 times. Eventually, a coast with 1:10 slope and sediment size of 0.2mm is considered, which is exposed to a wave field with $H_s=2\text{m}$ and $T_p=5.6\text{sec}$ in prototype with the same approach angle of 11.6 degrees as in laboratory scale.

Initially, the model is verified for no-groin situation (NT1 test). In this phase, a calibration, for the sediment transport coefficients, has been carried out to fit the computed cross-shore profile with the measured profile. Figure 1 shows the measured and simulated profiles.

The figure shows an overestimation of accretion on the coastline and a clear bar and trough, while in the lab a step is more distinguished. This is due to the fact that 8cm wave height in the laboratory hardly moves the sediment size of 0.2mm; therefore, most of the bed changes occur close to the coastline due to higher turbulence, while in prototype the model shows a clear offshore sediment exchange, since a wave height of 2m is attacking the coast.

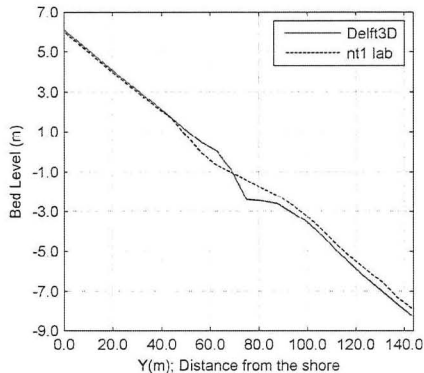


Figure 1, bed level after 4 hours in laboratory and prototype

In general, there is hardly any beach in the nature with $D_{50}=0.2\text{mm}$ and a 1:10 slope; the significant changes happening in the simulation are clearly representing the physics of prototype scale that are not present in the lab scale. Accepting the computed profile, the groins are then placed in the model. The groins are represented as so-called thin-dams that do not let any flow exchange or energy transfer (in wave simulations) between two adjacent grids. No permeability or overflowing is considered in these simulations. The model has been calibrated again for the sediment transport contributions. The *net* (NT4/NT5-NT1) computed sedimentation and erosion is given in Figure 2 below for NT4 & NT5 tests.

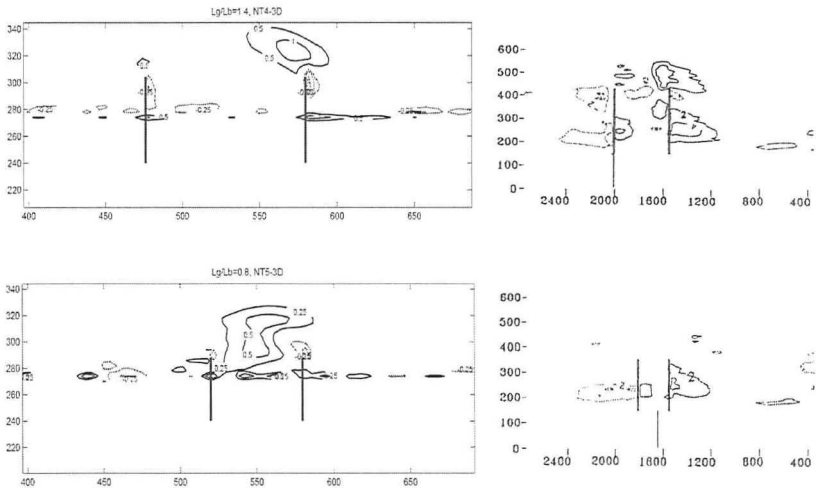


Figure 2 *net* computed effect of the groins for NT4 (upper left in m) and NT5 (lower left in cm) vs. laboratory measurements of Badiei et al. 1994 on the right; Note the scale difference in laboratory and prototype (0.5m contour line in prototype is compared with 1cm contour line in the lab)

The model shows relatively good performance for longer groins (NT4), but not a satisfactory for shorter groin. This can be explained in the initial profile. The computed initial profile (see Figure 1) has a steeper foreshore, which results in larger undertow velocities, especially along the groin, and eventually stronger bypassing at the tip of the right groin. The resemblance in case of longer groin is due to the fact that the alongshore transport is completely diverted offshore, due to extension of the groins outside the surfzone, and the difference in the initial foreshore slope is not an issue anymore. Note that, similar simulations in two-dimensional domain did not provide any better tool since the cross-shore processes were not properly included. This verification shows that a process-based model can be used to simulate morphological effects of the groins with extra caution on the sediment transport formulation used and calibration of the model with sufficient knowledge of present physics in the problem.

APPLICATION OF THE MODEL ON DESIGN OF A GROIN FIELD

Based on the validation in previous section an exercise is introduced to challenge the model and its applicability on design of a groin field. A Dean equilibrium cross-shore profile is considered. The beach is open to 1m waves with $T_{peak}=5$ sec. the waves are approaching the coast with an angle of 15 degrees with respect to the coast normal. The groins are placed in such a way that they hold a constant ratio of distance over length (L_g/D). The simulations were run for 45 days.

Primarily, the model must be calibrated to keep an equilibrium no-groin condition. The main calibration factors are coefficients of the vanRijn sediment transport formulation. These coefficients are:

- **SUS:** coefficient for current-related suspended sediment transport (0.4)
- **BED:** coefficient for current related bed load sediment transport (0.2)
- **SUSW:** coefficient for wave related suspended sediment transport (0.1)
- **BEDW:** coefficient for wave related bed load sediment transport (0.3)

The aforementioned calibration coefficients result in the cross-shore sediment contributions given in the Figure 3 below:

The Figure shows that the strongest cross-shore sediment transport contribution is current related suspended sediment transport, but by calibrating the coefficients an even offshore and onshore sediment transport is achieved. The combination of the given coefficients contribute to the cross-shore profile given in the figure 5 below showing little changes in the cross-shore direction.

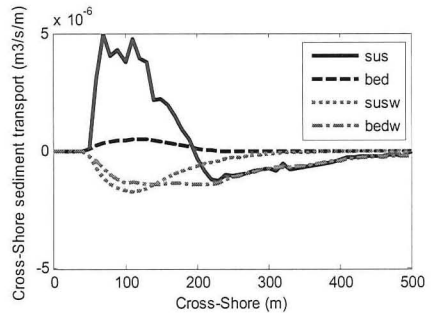


Figure 4 Cross-shore transport contributions (Positive offshore directed)

The sedimentation shown in the figure will be subtracted from the results in presence of the groins to achieve the net effect. Three different types of groins are considered in our case to trap sediment. One is extended outside the surf-zone ($L_g/L_b=1.2$), one is extended until the breaker line, and one is entirely inside the surf-zone ($L_g/L_b=0.8$); where L_b is width of the surf-zone. Three length over distance ratios are considered as well (0.2, 0.4 & 0.8).

Based on the above calibration, a number of tests (see Table 1) for different groin combinations are carried

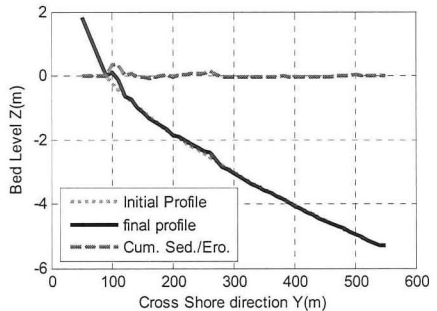


Figure 5, Initial and simulated cross-shore profile and the corresponding net sedimentation and erosion

out and some simulation results for one of the tests where the groins are not extended out of the surfzone (the most complicated physics are present) is presented below. Figure 6 shows the flow pattern around the groins, as a result of wave forcing (the only forcing on the system) and Figure 7 is the resulting bathymetry that can be compared with the initial bathymetry with completely parallel contour lines.

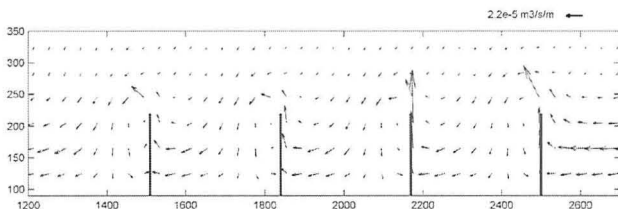


Figure 6, The alongshore flow pattern in presence of the groins (every 5 grid cell)

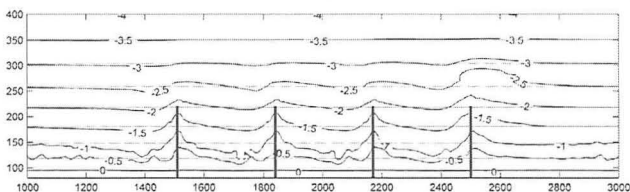


Figure 7, The net changes of the bathymetry in presence of groins after 45 days (black solid contour lines), and the initial profile (red dashed lines)

The above figures show a qualitatively good agreement between simulations and expected profiles and patterns in the nature (e.g. see CIRIA 1990 or CEM 2003), but, there is still a high level of uncertainty in quantitative comparison due to limited data. Based on these simulations, the velocity vectors bringing sediment into the system are weaker than the vectors carrying sediment offshore. The sediment grains carried offshore accrete as soon as they reach hydro-dynamically smoother areas. This offshore-directed sediment loss from the system is compensated by wave asymmetry (wave related sediment transport contributions, SUSW & BEDW, follow the wave propagation direction). To what extent this compensation occurs is highly dependent on local hydrodynamic characteristics in the nature, which must be seen in the calibration parameters (where the uncertainties arise). However, given all the uncertainties in sediment transport simulations, because of relatively acceptable hydrodynamic simulation, a general trend in the system can be seen, which makes it possible to compare different groin fields that share the same beach (different possible scenarios). Table 1 makes a quantitative comparison between different scenarios, and some of the quantities presented in the table are introduced below:

- **Trap1** gives the total accretion in between the groins and upstream of the first groin, the area covers $X=1500-2700\text{m}$
- **Trap2** shows accretion only in between the groins; $X=1500-2500\text{m}$
- **Total Vol.** is the cumulative volume that the groins encompass. Bounded to the 0m contour line and is extended offshore of the groin-head.

- **Cum. Length** no. of Groins X groin length, signifying construction costs
- **Trap1/cum. Length** symbolizing cost/benefit (trapping is treated as benefit)

Table 1 quantitative prediction of the groin fields performance (by Delft3D)

ID	Lg/Lb	Lg/D	Lg (m)	D (m)	No. of Groins	Trap1 (m3)	Total Vol.(m3)	Trap1/ tot.vol.	cum. length	trap1/ cum length	Trap2 (m3)
out1	1.2	0.2	200	1000	2	1383	419461	3.30E-03	400	3.46	-1950
out2	1.2	0.4	200	500	3	2307	419461	5.50E-03	600	3.85	-1065
out3	1.2	0.8	200	330	5	3220	419461	7.68E-03	1000	3.22	-194
break1	1	0.2	160	800	2	1491	281473	5.30E-03	320	4.66	1001
break2	1	0.4	160	400	3	1913	281473	6.80E-03	480	3.99	1393
break3	1	0.8	160	200	6	5169	281473	1.84E-02	960	5.38	2040
in1	0.8	0.2	130	650	2	87.4	192520	4.54E-04	260	0.34	114.5
in2	0.8	0.4	130	325	4	993.05	192520	5.16E-03	520	1.91	-1763
in3	0.8	0.8	130	163	7	2095	192520	1.09E-02	910	2.30	-732

The above quantitative comparison shows that trapping always improves with increasing the number of groins (Lg/D) for all groin-lengths; and is a small fraction of the total volume to be protected (hardly 1%). When the groin length and width of the surf-zone are similar accretion is maximized. The simple cost/benefit analysis shows that although increasing the number of groins improves performance of the system but it might be not always feasible (e.g. compare in2 and in3); of course, the value of the coast line might weight the analysis differently. The choice of Lg is relatively important, given that it might result in significant changes in the cost/benefit analysis (e.g. compare break3 and in3). Similar analysis can be done for different beaches and provides useful information in functional design phase.

VALIDATION OF THE MODEL IN CASE OF T-HEAD GROINS

Representation of complex structures in numerical models is a challenging task. T-Head groin is often recognized as an alternative for normal groin when the performance of normal groins is not convincing. Unfortunately, there are not many reliable datasets on application of T-Head groins. Hanson and Kraus 2001 studied the functionality of T-Head groins along Florida coast. Dabees & Humiston 2004 did a numerical study on design of a system of T-Head groins for Gasparilla Island project, near the gulf coast of Florida, using simple morphological models, and recommended usage of these models for functional design optimization.

Ozolcer et al. 2006 deep sounding measurements of a coast in Trabzon province, Turkey, is used to verify the applicability of Delft3D. Further attention is paid on representation of the T-Head groins in the model. A beach with parallel contour lines and a slope of 1:100 is exposed to a wave field with $H_{m0}=1\text{m}$ and $T_{m-1,0}=5\text{sec}$. The waves approach the coast under an angle of 15 degrees relative to the coast normal. The bathymetry was the result of a survey six months after construction. A calibration was needed before the simulations to find the proper sediment transport coefficients to hold the least cross-shore sediment exchange (The result was $SUS=0.2$, $SUSW=0.2$, $BED=0.2$, $BEDW=0.1$). Simulating the T-Head groins with the thin dams (See section for validation of normal groins) results in strong eddies in

the shadow zones of the T-heads, due to zero friction in between the wall and the body of water. Various measures were considered to overcome the drawback:

1. Increasing bed roughness locally to compensate for lack of wall roughness
2. Placing the real body of the groin in the bathymetry (as an un-erosive bed change) (4X4m grid cells)
3. Applying a wall roughness
4. Placing the real body of the groins with higher resolution (2X2m grid cells)

The surveyed bathymetry is shown in Figure 8 below:

Post-processing of different alternatives above showed that locally increased bed roughness might improve the flow pattern, but as it explicitly results in an increase of bed shear stress, it creates large gradients in sediment transport, which might result in either not smooth bed changes or numerical instabilities. Application of a wall roughness was potentially a good solution to damp strong eddies, but the current interpretation of the wall roughness needs a very large simulation area to avoid up-drift boundary effects. The most promising alternative is to simulate the real body of the groin in the bathymetry. It improved the flow pattern simulations qualitatively, due to a) reduction in the length of the T and the trunk part of the structure because of the thickness b) gradually varying flow field in between and outside the groin field. But, the smooth bed level changes were only comparable to the field survey (also quantitatively) when using higher resolution (20 computation grids along the groin). The resulting flow and sediment transport patterns are shown in the Figure 9 below:

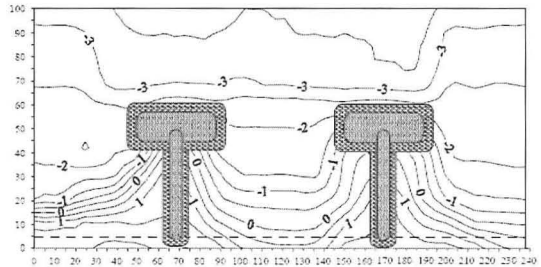


Figure 8. The surveyed bathymetry of the T- Head groin field by Ozolcer et al. 2004

It improved the flow pattern simulations qualitatively, due to a) reduction in the length of the T and the trunk part of the structure because of the thickness b) gradually varying flow field in between and outside the groin field. But, the smooth bed level changes were only comparable to the field survey (also quantitatively) when using higher resolution (20 computation grids along the groin). The resulting flow and sediment transport patterns are shown in the Figure 9 below:

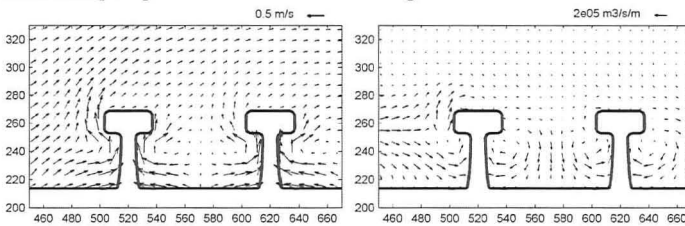


Figure 9. Sediment transport pattern following the Lagrangian velocity field vectors (right), Eulerian velocity field vectors (Left). The vectors are every 5 grid cell

The above flow and sediment transport fields (for further illustration on Eulerian and Lagrangian velocities see Walstra et al. 2000 and Groeneweg 1999) resulted in the final computed bathymetry as Figure 10 below.

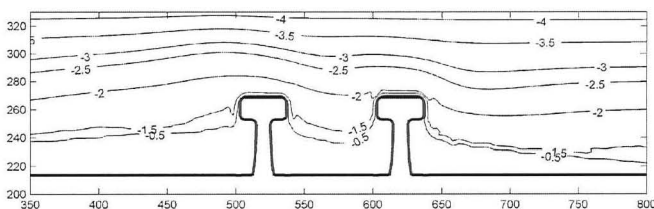


Figure 10 , The simulated bathymetry by Delft3D, starting from a constant slope cross-shore profile after 6 months

The above figure resembles the expected bathymetry of Figure 8 in a reasonable manner both qualitatively and quantitatively, although showing difficulty of such simulations in general. The problem of a high resolution grid which means more computation time may be solved with local nesting of the grid.

CONCLUSIONS AND RECOMMENDATIONS

A process-based numerical model is verified against available datasets for application on simulation of straight open groins (against laboratory measurement), and T-Head groins (against field measurement). Based on the qualitative comparison made in case of normal (straight open) groins, an exercise is introduced on design of a groin field to trap sediment; showing a relatively proper approach to overcome the difficulties on functional design of the groin fields, although a lot of uncertainties are still present, both, in the model and in our understanding of the nature.

Delft3D was able to reproduce the major physical processes in presence of normal groins when verifying against Badiei et al. 1994 experiments. It also showed sensitivity of the model to different parameters such as various coefficients of VanRijn's sediment transport formulation, bed slope (important in cross-shore processes) and sediment size. Although, the laboratory case is hardly representing the nature (There is hardly any beach with a 1:10 slope having grain size of 0.2mm in the nature), a general trend was observed in this study. In the next step, having a numerically generated cross-shore profile with a bar and trough, two combinations of groins with a constant ratio of length over distance (L_g/D) were simulated. The model results were qualitatively similar to the observed bed changes in case of long groins that are extended outside the surf zone ($L_g/L_b=1.4$). In case of shorter groins ($L_g/L_b=0.8$), when sediment bypassing was present, bed slope played an important role and different initial profile in simulation and laboratory explained the difference in simulation and measurement. Calibration of Delft3D for this case confirmed sensitivity of the model to sediment transport coefficients.

In the next phase, an exercise was introduced on design of groin fields. A Dean equilibrium profile was considered and different groin lengths and distances were tested and compared qualitatively with the expected flow patterns and bed changes. The flow patterns showed reasonably good agreement with what has been studied in different reports (e.g. CIRIA and CEM 2004). The exercise showed a possibility to assess performance of a groin field in functional design phase, using a process-based 3D model. Parameters, such as permeability of the groin, are not present in the flow model, while increased permeability is envisaged to improve trapping by reducing

the offshore directed velocities (addressed by Kraus et al. 1994). The same exercise can be considered for a T-Head groin field.

Delft3D was also verified against a field case in Trabzon province of Turkey, on the Black Sea coast. The main purpose of this study was to find the best way to represent T-Head groins in a model from both hydrodynamic and morphological point of view. The model tends to overestimate eddies in the shadow zone of the structure and to overcome the problem some measures were examined. Increased bed roughness along the trunk of the structure is an effective way to damp these eddies, but had direct influence on bed shear stress, therefore, high gradients and potential numerical instabilities did not provide an attractive approach for our purpose. Wall roughness was another effective tool, but its upstream boundary effects calls for larger simulation grid. It was shown that the precise body of the groins as an un-erosive bed level change resulted in the best hydrodynamic pattern and morphological response compared to the measurements, especially when employing higher resolution (more than 20 grid cells along both dimensions of the structure).

REFERENCES

- Badiei P., J. William Kamphuis, David G. Hamilton, 1994 "Physical Experiments on the Effects of Groins on Shore Morphology", Proc. ICCE 1994, pp 1782-1796
- Briggs, M.J., Thompson, E.F., Vincent, C.L., 1995. Wave diffraction around breakwater. *Journal of Waterway, Port, Coastal, and Ocean Engineering*, ASCE 121 (1), 23-35.
- Mohammad A. Dabees, Brett D. Moore & Kenneth K. Humiston, "Enancement of T-Groin's design to improve downdrift Shoreline Response", Proc. ICCE 1994, pp 2423-2435
- Fredsoe, J., 1984. "Turbulent boundary layer in wave-current interaction". *ASCE Journal of Hydraulic Engineering* 110, 1103-1120.
- Goda, Y., 2000. *Random Seas and Design of Maritime Structures*. World Scientific, Singapore.
- Hulsbergen C.H., Bakker W. T. Van Bochove G. (1976). "Experimental Verification of Groyne Theory", Proc. 15th Coastal Engineering Conf. pp 322-335
- Ilic, S., Chadwick, A.J., Fleming, C., 2005. Detached breakwaters: an experimental investigation and implication for design -Part1- hydrodynamics. *Proceedings of ICE, Maritime Engineering*.
- Ilic, S., A.J. van der Westhuysen, J.A. Roelvink, A.J. Chadwick, 2007, Multidirectional wave transformation around detached breakwaters", *Journal of Coastal Engineering* 54, 775-789
- Kraus N. C., Hans Hanson, Blomgren H. S., 1994, "Modern Functional Design of Groin Systems", Proc. ICCE 1994, pp. 1327-1342
- Kraus N. C., Hans Hanson, 2001, "Chronic Beach Erosion Adjacent to Inlets and Remediation by Composite (T-Head) Groins", US Army Corps of Engineers
- Mory, M., Hamm, L., 1997. Wave, set-up and currents around a detached breakwater submitted to regular and random wave forcing. *Coastal Engineering* 31, 77-96.
- Ozolcer, I. H. , Komurcu, I. K., Birben, A. R., Yusek, O., Karasu, S., 2006, "Effects of T-Shape Groin Parameters on Beach Accretion", *Journal of Ocean Engineering* 33 pp 382-403
- SWAN user Manual, Technical Documentation (Holthuijsen et al.)
- US Army Corps of Engineers, *Coastal Engineering Manual* (2003)
- US Army Corps of Engineers, *Shore Protection Manual* (1984)
- Leo C. van Rijn, 2009, "Prediction of Dune Erosion due to Storms", *Journal of Coastal Engineering* 56 pp 441-457
- Walstra, D.J.R., Roelvink, J.A., Groeneweg, J., 2000. "Calculation of wave- driven currents in a 3D mean flow model". Edge, B. *Coastal Engineering* vol. 2. ASCE, New York, pp. 1050- 1063.
- Whitham, G.B., 1974: *Linear and nonlinear waves*, Wiley, New York, 636 p.

Effect of Sheetpile Configuration on Seepage beneath Hydraulic Structures

Ashraf A. Ahmed¹ and Azza M. Elleboudy²

¹Associate Professor, Department of Civil Engineering, Faculty of Engineering, Benha University, 108 Shobra St., Cairo 11629, Egypt; PH (202) 2672-1922; email: ashraf.elkholy@gmail.com

²Professor, Department of Civil Engineering, Faculty of Engineering, Benha University, 108 Shobra St., Cairo 11629, Egypt; PH (202) 2526-4224; email: prof.azza@feng.bu.edu.eg

ABSTRACT

This paper investigates the influence of various sheetpile configurations on the seepage losses, the uplift force on downstream apron of floor, and the exit gradient at the end toe of the apron. A computer program, utilizing the finite element method and based on the fixed mesh approach, was used to locate the free surface of water. The model was applied to investigate seepage below and around a hydraulic structure. Several configurations of the sheetpile driven under the structure were analyzed. Results showed that when the sheetpile confined the downstream apron of the floor from all sides, it has dramatically reduced the exit gradient. In return, this was accompanied by some increase in the uplift pressure force acting on the structure. Other configurations that needed more sheetpile material had little effect on the uplift force and exit gradient.

KEYWORDS: Unconfined seepage; Uplift force; Exit gradient; Finite element; Seepage losses.

INTRODUCTION

Hydraulic structures built over pervious soil strata should be secured against uplift forces acting on the floor of the structure and against the phenomenon of piping. For this purpose, design engineers always provide the floor of the structure with one or more sheetpile to reduce the uplift force and exit gradient at the downstream toe of the apron (Cedergren, 1989). This is because the consequence of piping and erosion, resulted by letting the exit gradient approaches its critical value, can be very severe and may lead to complete failure of the structure (Griffiths and Fenton, 1998).

Researchers follow a conventional analysis when studying seepage flow under hydraulic structures: only the flow beneath the floor has been considered with complete disregard to the water seeping through the banks of the canal. The main reason for this is because most of these analyses are two-dimensional (2D). Even though in three-dimensional (3D) analysis (e.g. Ahmed et al., 2007a; Griffiths and Fenton, 1997, 1998), the water seeping through the banks was overlooked. This leads to limitations in the investigation of sheetpile configuration. The sheetpile position,

considered in most of the previous studies, is one or more sheetpile driven beneath the floor of the structure and extends laterally in the out-of-plane direction across the floor width.

The main objective of the current research was to investigate the influence of different sheetpile configurations on seepage losses, the uplift force, and the exit gradient at the end toe of the apron. The canal width/differential head ratio was constant. In each case, the 3D results were compared with that obtained from the 2D analysis.

MATHEMATICAL BACKGROUND

Residual Flow Procedure (RFP)

The RFP presented herein, which was used to locate the free surface, follows closely Bathe and Khoshgoftaar (1979), Desai and Li (1983), and Desai and Baseghi (1988). The partial differential equation that governs steady incompressible fluid flow through porous medium can be written as:

$$\text{div} (k \text{ grad } \phi) = 0.0 \quad (1)$$

where, k = hydraulic conductivity of the medium, $\phi = P/\gamma + Z$ = total fluid head, P/γ is the pressure head, Z is the elevation head, and γ is unit weight of fluid. The pseudo-functional, U , for the steady state flow can be expressed as:

$$U = \frac{1}{2} \iiint_v k \left[\left(\frac{\partial \phi}{\partial x} \right)^2 + \left(\frac{\partial \phi}{\partial y} \right)^2 + \left(\frac{\partial \phi}{\partial z} \right)^2 \right] dx dy dz \quad (2)$$

Applying the RFP yields the element equations:

$$[k_s]^e \{q\} = \{Q_r\}^e \quad (3)$$

Where $[k_s]^e$ is the element hydraulic conductivity matrix at saturation, $\{q\}$ is the vector of nodal fluid heads of element, and $\{Q_r\}^e$ is the element residual flow vector composed as,

$$\{Q_r\}^e = [k_{us}]^e \{q\} \quad (4)$$

Where $[k_{us}]^e$ is the unsaturated hydraulic conductivity matrix. The assembly over elements yields:

$$[K_s] \{r\} = \{R_r\} \quad \text{on the entire domain} \quad (5)$$

Where $[K_s]$ is the overall hydraulic conductivity matrix at saturation, $\{r\}$ is the overall nodal fluid head vector, and $\{R_r\}$ is the overall residual flow vector. Eq. 5 is a system of nonlinear equations.

For the free surface flow through the banks, the hydraulic conductivity was taken according to Bathe and Khoshgoftaar (1979):

$$k = \begin{cases} k_s & P \geq 0 \\ k_s / 1000 & P < 0 \end{cases} \quad (6)$$

A detailed model description, verification, and applications can be found in Ahmed et al. (2007a, b)

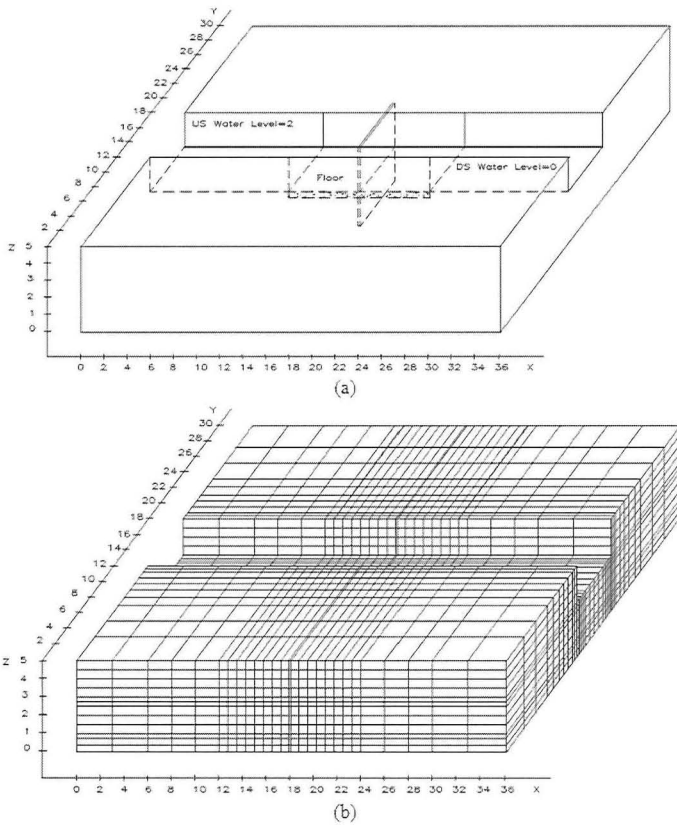
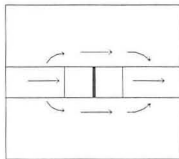


Figure 1. Isometric view and finite element mesh for the application problem.

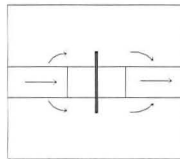
APPLICATION PROBLEM AND ANALYSIS PROCEDURE

Figure 1-a shows an isometric view of the problem: a hydraulic structure resting on a pervious homogenous isotropic soil of depth 3 m, and hydraulic conductivity 5×10^{-4} m/sec. A sheetpile of penetration depth 2 m is driven underneath the structure. The length of the modeled zone was 36 m, considering two vertical impervious boundaries 18 m upstream and downstream the sheetpile. No appreciable change was observed in results when the domain length was extended beyond 36 m. The banks of the canal extended 12 m each side and its top level was 2 m above the bed level of the canal. The floor of the structure was 12 m in length and extended 6m across the canal width. The side retaining walls of the structure rose up to the bank level. The seepage flow occurs due to a differential head of 2 m between the upstream and the downstream sides of the structure. Figure 1-b shows the finite element mesh used in the analysis. The total number of nodes was 10780 and the total number of elements was 9072.

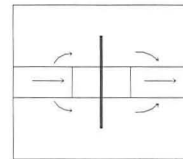
The problem was studied by considering different values of the width of the sheetpile driven under the floor. These cases are $W/B = 1, 2, 3$ and 5, where B is the width of the canal (6 m), and W is the total width of the sheetpile. In all cases, the sheetpile was symmetric about the canal centerline and extended vertically up to the top level of the banks. The problem was then studied for another two cases. In the first case, the sheetpile confined the downstream floor from three sides then in the second case, the sheetpile confined the downstream floor from all sides. Figure 2 illustrates the various cases.



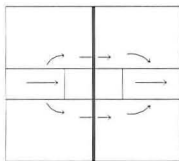
(1) Width of sheetpile = canal width
($W/B = 1.0$)



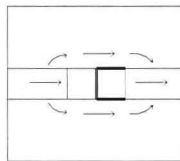
(2) Width of sheetpile = 2 X canal width
($W/B = 2.0$)



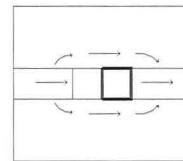
(3) Width of sheetpile = 3 X canal width
($W/B = 3.0$)



(4) Width of sheetpile = 5 X canal width
($W/B = 5.0$)



(5) The sheetpile confines the DS
floor from 3 Sides



(6) The sheetpile confines the DS
floor from 4 sides

Figure 2. Different arrangements for sheetpile driven under the structure.

BOUNDARY CONDITIONS

The bed level of the canal was taken as the reference level. The bed and vertical sides of the canal on the upstream side were modeled as prescribed head boundaries where the head equaled 2.0 m. The bed of the canal on the downstream side was also modeled as prescribed head boundary with zero head. The exit surface was represented along the downstream vertical sides of the canal since flow could possibly exit anywhere along these faces. All the external vertical boundaries, the bottom boundary, the floor, and the retaining walls were modeled as impermeable boundaries.

RESULTS AND DISCUSSION

Figure 3 shows the change in exit gradient at the end of the downstream floor apron along the channel width. The exit gradient attained its maximum value at the canal edges not at the centerline, as it has traditionally been thought. It can also be noticed that there was a significant reduction on the exit gradient when the sheetpile confined the downstream apron from all sides. Moreover, when the sheetpile confined the downstream apron from three sides only as in case 5, it introduced no appreciable change in the exit gradient compared with case 1 although the length of the sheetpile used was 3-times more. The same applies to case 4; there was no appreciable change in the exit gradient compared with case 1 although the length of the sheetpile used in case 4 was 5-times more.

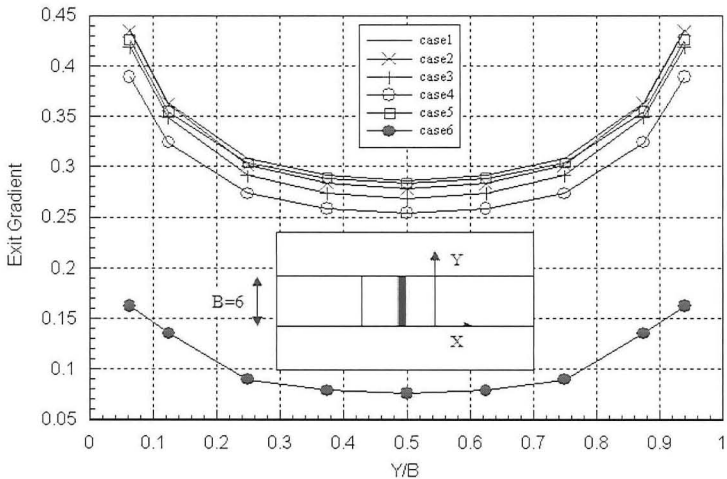


Figure3. Change in exit gradient along the canal width.

Figure 4 depicts the change of the flow rate, the uplift force under the downstream floor apron, and the exit gradient measured at the edge of the canal, for the different cases. The vertical axis represents the flow rate, the exit gradient, and the uplift force of the modeled 3-D cases normalized to their values obtained from the 2-D solution of this problem. The flow rate was calculated by considering only the part flowing under the floor of the structure. This was done to facilitate comparison between the different 3-D cases and the 2-D solution. The normalized values of the flow rate were less than unity. It is because part of the seeping water flows through the banks. The flow rate steadily increased as the W/B value increased. This is because the open space of the banks was gradually decreased as the width of the sheetpile increased. When the sheetpile covered the entire width of the modeled domain (case 4), the conditions approached the 2-D solution. Obviously, the effect of increasing the sheetpile width did not introduce a noticeable change in the flow rate.

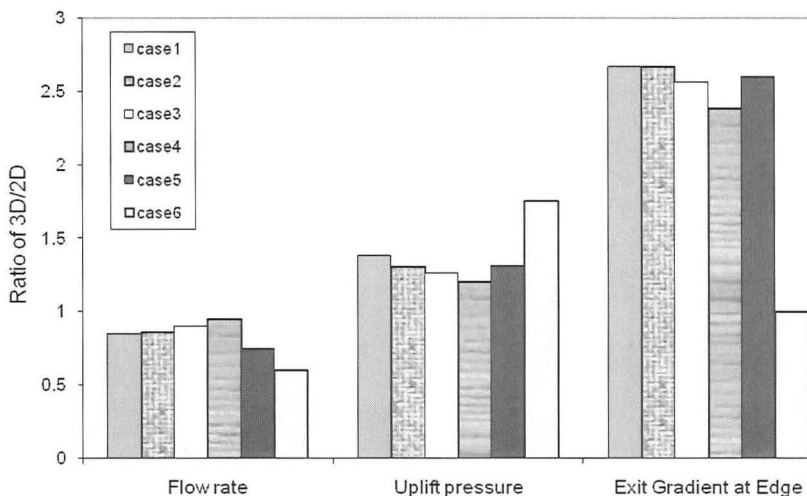


Figure 4. Change of flow rate, uplift pressure, and exit gradient with sheetpile configurations.

The uplift force increased to reach 140% for case 1 and 175 % for case 6 relative to their corresponding values obtained from the 2-D solution (Fig. 4). This increase in the value of uplift pressure in case 6 than in case 1 is because the way the water has to travel under the floor of the structure is longer for case 6 than case 1. This can be clarified by referring to the distribution of the uplift pressure under the floor according to the method of Bligh (Leliavesly, 1965). The uplift pressure distribution is shown in Figure 5-a for case 1, and in Figure 5-b for case 6. The value

of the uplift pressure h_2 at the end toe is greater in case 6 than in case 1, while it has same value h_1 at the middle sheetpile. In other words, the area the uplift pressure acted upon, which determines the uplift force, is greater for case 6 than case 1. Obviously in Figure 4, the effect of increasing the sheetpile width (cases 1 to 5) did not introduce a significant reduction in the uplift force.

The relative value of the exit gradient increased markedly to reach about 270% for the case $W/B=1$. For all cases, with the exception of case 6, the value of the exit gradient is very high compared to the corresponding value obtained from the 2-D solution of the same problem. This illustrates that values obtained from the 2-D solution are sometimes in great error. The reason of this increase in the exit gradient produced from the 3-D solution is because of the water flow through the banks, which is not considered in the 2-D solution.

When the sheetpile confined the downstream floor apron from all sides (case 6), the exit gradient was dramatically reduced. This dramatic reduction in the exit gradient is attributed to increasing the length through which water percolates, while the differential water head is constant. The practical consequence of this reduction in the exit gradient is clear, that the safety of the structure against piping and percolation increases. Obviously, if the sheetpile was driven under the floor as in case 6, it is more effective than other cases, such as case 4, although less sheetpile material is used in case 6 than in case 4.

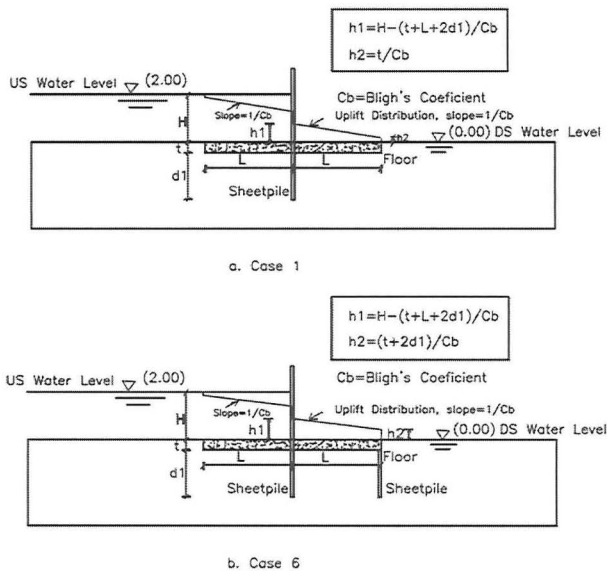


Figure 5. Change of exit uplift force with different sheetpile arrangements.

CONCLUSIONS

A number of numerical analyses were carried out to study the influence of different sheetpile configurations, constructed beneath the floor of a hydraulic structure, on seepage losses, uplift force, and exit gradient. It was observed that extending the sheetpile laterally through the banks of the canal has no appreciable influence on either uplift force acting on the structure or the exit gradient at the end toe of the floor. It only caused much more consumption of the sheetpile material with no noticeable gained benefits. It was also found that driving a sheetpile under a hydraulic structure that surrounds the downstream floor apron from all sides, has greatly reduced the exit gradient at the end toe of the floor. However, this was accompanied with some increase in the uplift force.

REFERENCES

- Ahmed A. A., Soliman , A. M., and Bazaraa, A. S. (2007a). "3-D steady analysis of leaky hydraulic structures: 1. Leaky sheetpiles." *Journal of Engineering and Applied Science* 54 (2):141-157.
- Ahmed A. A., Soliman , A. M., and Bazaraa, A. S. (2007b). "3-D Steady analysis of leaky hydraulic structures: 2. Leaky dams." *Journal of Engineering and applied Science* 54 (3): 289-302.
- Bathe, K. J., and Khoshgoftaar, M. R. (1979). "Finite element free surface seepage analysis without mesh iteration." *Int. J. Numer. Analyt. Meth. Geomech.* 3: 13-22.
- Cedergren, H. R. (1989). "Seepage, Drainage, and Flow Nets." 3rd Edition, New York: Wiley.
- Desai, C. S., and Li, G. C. (1983). "A residual flow procedure and application for free surface flow in porous media." *Adv. Water Resour.* 6: 27-35.
- Desai, C. S., and Baseghi, B. (1988). "Theory and verification of residual flow procedure for 3-D free surface seepage." *Adv. Water Resour.* 11: 192-203.
- Griffiths, D. V., and Fenton, G. A. (1997). "Three-dimensional seepage through spatially random soil." *J. Geotechnical and Geoenvironmental Engrg.* 123: 153-160.
- Griffiths, D. V., and Fenton, G. A. (1998). "Probabilistic analysis of exit gradients due to steady seepage." *J. Geotechnical and Geoenvironmental Engrg.* 124: 789-797.
- Leliavesly S. (1965). *Design of Dams for Percolation and Erosion.* Chapman and Hall, London.

A Microscopic Study on Soft Rock Erosion by Using Particle Flow Simulation

Y.W. Pan^{1,2}, M. ASCE, J.J. Liao^{1,2}, P.C. Li², and G.W. Li¹

¹Department of Civil Engineering, National Chiao Tung University, Hsinchu, Taiwan 30010.

²Disaster Prevention & Water Environment Research Center, National Chiao Tung University, Hsinchu, Taiwan 30010.

ABSTRACT

Few existing erosion models have looked into the micromechanics of rock erosion. This study made use of particle flow simulation to model the erosion process of soft rock in microscopic scale which may be regarded as a “virtual erosion test”. In the simulation, rock material is modeled as a granular assemblage with inter-particle bonding; the erosion process is simulated as particles’ release due to de-bonding. Saltating abrasion can be a consequence of gravel traveling along with water flow and striking on the riverbed; the impact results in the local failure and causes abrasion. The major factors affecting the erosion rate are examined through a series of virtual erosion tests. Simulated results show that more de-bonded particles may occur for a condition with higher impact speed, higher impact angle, larger gravel size, higher Young’s modulus, or lower rock strength. It appears that particle flow simulation is able to capture the mechanism of abrasion by saltating gravel.

INTRODUCTION

Although rock bed is often considered a lot more resistant to erosion than alluvium, exposed soft-rock bed may be subjected to significant erosion (e.g., Huang, *et al.*, 2008). In several notable cases in Taiwan, intensive erosion occurred in soft rock river-bed soon after the boulder or gravel cover was eroded away as a result of the change in stream power due to an abrupt headcut because of a man-made cross-river structure or a sudden uplift by faulting. The continuous erosion in rock-bed may largely endanger the stability of cross-river structure such as bridge piers and weirs; it may also accelerate river-bed incision. The mechanisms for the scouring processes in soft rock deserve serious attention for engineering concerns.

Soft rocks belong to a category of weak rocks (ISRM, 1981), often considered as a “marginal” or “transitional” geo-material (i.e. between soils and brittle rocks) (Johnston, 1993; Oliveira, 1993). They usually present unfavorable characteristics including poor cementation, low strength and high deformability (Johnston, 1993) due to insufficient lithification. The outcrops in the northern and western foothills of Taiwan, composed mostly of weakly cemented sedimentary rocks formed in the epochs from late Miocene to Pleistocene, exhibit the typical characteristics of soft rocks. Their unconfined strengths are often under 25 MPa. For typical soft rock formations, the presence of fractures or joints is usually not very significant.

The mechanisms of rock erosion have been studied by many researchers (e.g., Whipple, *et al.*, 2000). In general, the major mechanisms of rock erosion can be classified into (1) hydraulic erosion of un-jointed intact rock, (2) hydraulic erosion of jointed rock masses (plucking), (3) abrasive erosion due to bed load or suspended load, and (4) cavitation. In some cases, dissolution and weathering of rock material can also result in the mass loss of rock material exposed in water current

Existing models for the erosion-rate estimation of rock-bed may be rational (e.g., Howard, and Kerby, 1983), empirical (Annandale, 2006) or mechanical-process based (e.g., Sklar and Dietrich, 2004). The hydraulic erosion rate of rock-bed is often described by an empirical erosion law that approximates the erosion rate as a power function of bed shear stress or stream power; these types of empirical law of erosion rate can be generalized into “stream-power family of models” (Whipple & Tucker, 1999). A model may also include a threshold shear stress for incision and may consider the influence of sediment load on incision rate. Many of these models are intended for describing erosion rate in a reach scale.

Index based model such as the one developed by Annandale (1995) is available for estimate the erodibility of rock-bed by hydraulic erosion in terms of the so-called “erodibility index”. The erodibility index takes into account major factors influencing the erodibility of rock-bed. Four indices include the material strength, block/grain size, joint strength, and joint structure of rock masses are taken into account. The definition of the erodibility index is the multiplication of these four individual indices. Annandale (2006) also suggested an empirical relation that correlates the erodibility index and the threshold stream power causing erosion.

Abrasive erosion or abrasion is a result of wearing by bed-load particles traveling along with current. In strong current, saltating bed-load particles may strike on the riverbed and cause the fracture and deaggregation of material on the

rock surface; this mechanism is called "saltation abrasion". The bed load may either provide a cover effect (protecting rock-bed from abrasion) or serve as a tool effect (enhancing abrasion) (Gilbert, 1877; Foley, 1980). The rate of saltation abrasion is affected by the grain size of bed load, the trajectory of particle, particle impact velocity, sediment flux, and the rock resistance to abrasion.

Sklar and Dietrich (2004) developed a mechanically based model for modeling the abrasion by saltating bed-load particles. The fundamental concept of this model states that the bedrock incision rate due to particle saltation can be expressed as the product of (1) the volume of removed (disintegrated) rock per particle impact V_i , (2) the rate of particle impacts per unit area per unit time I_r , and (3) the fraction of exposed bedrock F_e . The first term V_i depends on impact characteristics (impact energy level, impact direction, particle size, etc) and the rock resistance against particle impact; V_i is expressed as the transferred impact (excess) kinetic energy divided by the required energy to erode a unit rock volume ε_v . Sklar and Dietrich (2004) assumed that only the kinetic energy due to normal component of impact velocity is effective for saltating abrasion; the effect of cutting wear affected by the tangential component of impact velocity is neglected. The required energy ε_v is assumed proportional to the stored elastic strain energy relating to the tensile strength σ_T and Young's modulus E of rock material expressed as $\varepsilon_v = k_v \frac{\sigma_T^2}{2E}$ in which k_v is a proportionality constant. The second term I_r is a function of flux of bed load particles and the trajectory of particle motion. The last term F_e depends on sediment transport capacity.

The quantitative estimation of the bedrock incision rate based on this model relies on the close estimation of V_i which is very much related to the micromechanics of the rock material subjected to an impact loading. To date, very few studies have looked into the micromechanics of rock erosion. The present work attempts to model the saltation-abrasion process of soft rock in microscopic scale by using particle flow simulation to explore the fundamental mechanisms of abrasion due to gravel saltation on rock river-bed.

METHOD OF NUMERICAL SIMULATION

The particle flow simulation in this work made use of the code PFC^{3D} (ITASCA, 2006) that represents a granular material as an assemblage of spherical balls. PFC^{3D} belongs to the category of numerical method of distinct element methods dealing

with the mechanics of a dis-continuum (Cundall and Strack, 1979). The distinct element method is an explicit numerical method that successively solve for the Law of Motion for each particles and the inter-particle contact force-displacement relation in a particles' assemblage.

Modeling of Rock Material

In this study, a rock material is modeled as a particles' assemblage with assigned inter-particle bonding. The particles' assemblage contains roughly 11000 balls with radius in the range of 0.2 – 0.3 mm to model a virtual rock specimen of the size 150 mm by 100 mm by 80 mm bounded by walls. Fig. 1 shows the particles' assemblage used in this work. The target porosity is controlled by slightly expanding the particles' radius. Rock material with a specific set of macroscopic engineering properties can be modeled by assigning an appropriate set of microscopic parameters to the particles' assemblage. Required microscopic parameters may contain particle parameters including density, particle size, Young's modulus, and inter-particle parameters including bonding-strength parameters, contact stiffness, and contact frictional coefficient.

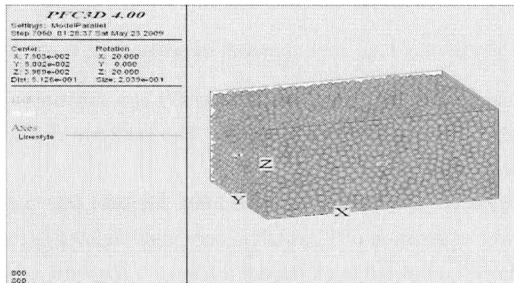


Figure 1. The assemblage of particles.

Microscopic parameters influence the macroscopic mechanical properties in predictable trends. Young's modulus is roughly proportional to the microscopic Young's modulus; also increases with an increase in either contact normal stiffness or friction coefficient. Poisson's ratio decreases with the increasing ratio between contact normal stiffness and shear stiffness. Unconfined strength is roughly proportional to the bonding strength. Friction angle increases with increasing frictional coefficient.

To model a rock material, the microscopic parameters were assigned so that the numerically simulated stress-strain curves for common laboratory tests (e.g., triaxial compression tests) can be close enough to the ones actually obtained by laboratory tests on the material. Soft rock often has its uniaxial compressive strength under 25 MPa. For illustration, Fig. 2 shows the stress-strain curves corresponding to three different uniaxial compressive strengths with a similar Young's modulus.

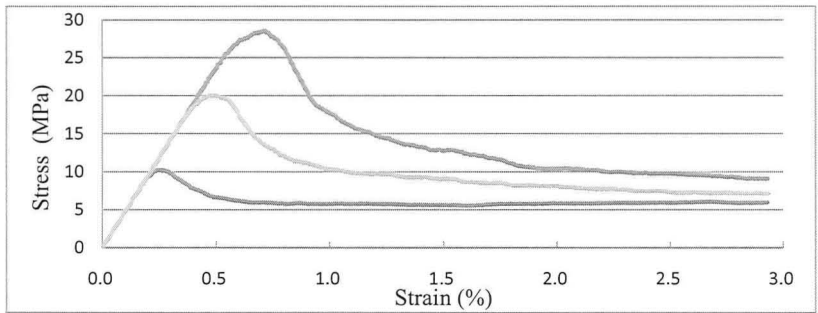


Figure 2. Simulated stress-strain curves for triaxial compression tests with various confining pressures.

Modeling of Rock Abrasion

The numerical simulation aims to model the process of rock erosion and can be regarded as a “virtual erosion test”. In the numerical simulation, the abrasion process is a result of particles’ release due to de-bonding. Both bed shear acting on the rock surface or impact arising from saltating gravel can trigger local inter-particle bonding failure so that results in rock erosion or abrasion. To model abrasion due to gravel saltation, a particle which is represented as a spherical ball, much larger than the sizes of grains (also represented by balls) of the rock material, was allowed to hit the surface of the virtual rock specimen. The generated stress wave, if large enough, may result in inter-particle de-bonding or breakage adjacent to the location of impact.

RESULTS OF SIMULATION

Fig. 3 demonstrates the simulated results for saltating abrasion in sequential stages. Fig.3(a)-(d), respectively, show the stage for the approaching gravel, the moment of impact, the rebound off the surface, and the flush-away of de-bonded

particles. As noted in Fig. 3, the impact of saltating gravel onto the rock surface results in a clustered zone of de-bonding particles under the impact point. Once de-bonded, those released particles can be moved away by water current so that causes erosion.

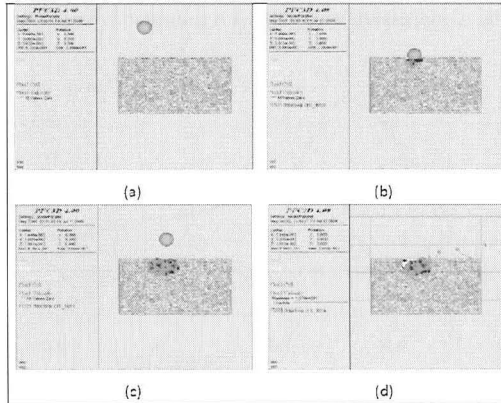


Figure 3. Simulated results for saltating abrasion in successive stages.

The amount of abrasion due to saltation is largely dependent on the transfer of impact kinetic energy and the rock resistance against abrasion. The transfer of impact kinetic energy is affected by the mass, the speed and the impact direction of the saltating gravel. Either a larger saltating particle or a higher traveling speed will have a higher kinetic energy so that will have a higher potential to damage the impacted rock surface.

According to the wear theory of Bitter (1963 a & b), the vertical component of velocity can produce the deformation and fatigue failure of material so that results in the so called “deformation wear”; while the tangential component of velocity can cause shearing failure of material so that results in the so called “cutting wear”. Impact at a higher angle (with respect to the tangential direction of contact force) has a higher normal component of velocity; and vice versa. The model of Sklar and Dietrich (2004) neglects the cutting wear of saltating gravel; only deformation wear is taken into account in their model. The rock resistance against abrasion is expressed as stored elastic strain energy in terms of $\epsilon_v = k_v \frac{\sigma_T^2}{2E}$ in their model.

This relation suggests that the required energy to erode a unit rock volume is proportional to the square of the tensile strength and inversely proportional to the Young's modulus of rock material.

To explore the factors affecting the potential abrasion due to saltating gravel, a series of simulation were carried out by changing a series of variables including the uniaxial compressive strength σ_c and modulus of rock material E , gravel size D , incident angle θ , and impact velocity U_i . The considered range of σ_c is within the typical strength of soft rock. The range of gravel size is within 10 mm and 40 mm. Two different incident angles, 30 degrees and 60 degrees with respect to the tangential direction are modeled. The modeled approaching velocity of saltating gravel is within 1 m/sec and 10 m/sec. The number of de-bonded particles after impact N_{db} for each case was counted to evaluate the potential erodible volume after the strike of a saltating particle. The average volume for each particle is about $6.54 \times 10^{-11} \text{ m}^3$.

Fig. 4 shows N_{db} versus gravel size with a same impact velocity at two different incident angles θ for various σ_c (under the condition of $U_i = 6 \text{ m/s}$). The solid curves and the dashed curves are for $\theta = 30^\circ$ and 60° , respectively. The 30° incident angle can be regarded as a low-angle impact; while the 60° incident angle can be regarded as high-angle impact. The comparison of the solid and dashed curves reveals that high-angle impact produces significantly more inter-particle de-bonding damage in the material than the case of low-angle impact. It is evident that normal component of impact velocity significantly does play a much more important role on saltating abrasion than the tangential component of impact velocity. Fig. 4 also reveals that rock material with a higher strength will have a higher resistance against abrasion so that N_{db} has a smaller value.

Fig. 5 shows N_{db} versus impact velocity for various gravel sizes (under the conditions of $\sigma_c = 12 \text{ MPa}$ and $\theta = 60^\circ$). It appears that N_{db} increases with impact velocity and gravel size. Saltating gravel with a higher impact velocity has a higher kinetic energy to break the inter-particle bonding adjacent to the impact point. A highly nonlinear increase of N_{db} with raising impact velocity is notable. It appears the impact gravel velocity plays a major effect on the de-bonding or breakage of rock material after saltating impact.

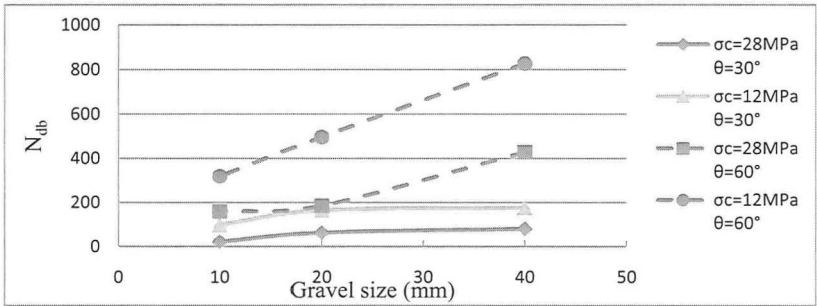


Figure 4. Number of de-bonded particles versus gravel size for various incident angle and rock strength.

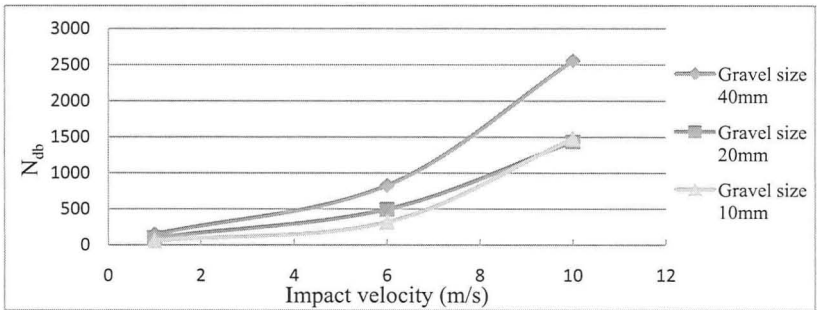


Figure 5. Number of de-bonded particles versus impact velocity for various sizes of saltating gravel (with 60° incident angle).

The mechanical properties of bed-rock influence the eroded rock volume after each impact. Fig. 6(a) presents the influence of the Young's modulus of rock material on N_{db} (under the conditions of $U_i = 6$ m/s and $\theta = 60^\circ$). Under same conditions of the saltating gravel; N_{db} nonlinearly rises with the increase in the Young's modulus. Fig. 6(b) shows the influence of tensile strength of rock material on N_{db} . Under same conditions of a saltating gravel, N_{db} nonlinearly decreases with the increase in the tensile strength. The kinetic energy remains the same under same conditions of the saltating gravel. N_{db} should be inversely proportion to the required energy to erode a unit rock volume ε_v , but not necessarily following the stored elastic strain energy expressed as the form of $\varepsilon_v = k_v \frac{\sigma_T^2}{2E}$.

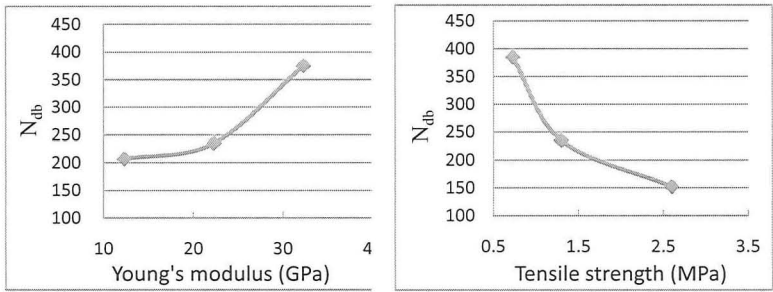


Figure 6. Number of de-bonded particles versus (a) Young's modulus and (b) Tensile strength.

SUMMARY AND CONCLUSION

This work made use of particle flow simulation to model the abrasion process of soft rock in microscopic scale. Its objectives are to model the process of abrasion due to gravel saltation, and to explore the micromechanics of the erosion process. A rock material is modeled as a granular assemblage with inter-particle bonding. This type of simulation can be regarded as a “virtual erosion test”. To model the abrasion due to gravel saltation, the simulation allows a saltating particle to hit the surface of the virtual rock specimen. After the impact, the stress wave results in the inter-particle de-bonding or breakage under the impact point so that causes rock erosion near the surface. The erodible volume after each impact by saltating gravel should be proportional to the number of de-bonded particles.

The abrasive amount due to each saltation impact depends on the transferred impact energy and the rock resistance. To explore the major factors affecting potential abrasion due to saltating gravel, a series of simulation were carried out by changing variables including mechanical properties of rock material, gravel size, incident angle, and impact velocity. It is shown that the number of de-bonded particles will increase with increasing gravel size, incident angle, and impact velocity. The gravel size and impact velocity contribute to the impact kinetic energy that can be transferred to rock bed so that damages the rock material. A higher incident angle results in higher normal component of impact velocity so that causes a higher degree of deformation wear. For the influences of mechanical properties of rock material, a rock material with higher rock strength (both in compressive and tension)

will offer higher resistance to abrasion by impact so that causes a less amount of erodible volume after each impact; while the erodible volume after each impact tends to rise with an increase in the Young's modulus of rock material.

REFERENCES

- Annandale, G.W. (1995). "Erodibility.", *Journal of Hydraulic Research*, 33(4): 471-494.
- Annandale, G.W. (2006). "Quantification of the Erosive Capacity of Water." *Proc. 3rd Int. Conf. on Scour and Erosion*, Amsterdam, Netherlands: 1-6.
- Bitter, J.G.A. (1963a). "A study of erosion phenomenon, Part I." *Wear*, 6(1): 5-21.
- Bitter, J.G.A. (1963b). "A study of erosion phenomenon, Part II." *Wear*, 6(3):169-190.
- Cundall, P., O. Strack (1979). "A discrete numerical model for granular assemblies." *Geotechnique*, 29(1): 47-65.
- Foley, M.G. (1980). "Bedrock incision by streams." *Geological Society of America Bulletin*, Part II, 91: 2189-2213.
- Gilbert, G. K. (1877). *Report on the Geology of the Henry Mountains : Geographical and Geological Survey of the Rocky Mountain Region*, 160p.
- Howard, A.D. and Kerby, G. (1983) "Channel changes ub badlands." *Geol. Soc. of America Bulletin*, 94:739-752.
- Huang, M.W., Cheng, M.H., Liao, J.J., and Pan, Y.W. (2008). "Rapid bedrock erosion in the Taan River." *Proc. 4th Int. Conf. on Scour and Erosion*, Tokyo, Japan.
- ISRM. (1981). "Rock characterization testing and monitoring." *ISRM Suggested Methods*, Pergamon Press, New York.
- ITASCA (2006). *Manuals of PFC^{3D}*.
- Johnston, I.W. (1993). "Soft tock engineering." *Comprehensive Rock Engineering: Principles, Practice & Project (V. 1)*, Pergamon Press: 367-393.
- Oliveira R. (1993) "Weak rock materials." *The Engineering Geology of Weak Rock*: 5-15.
- Sklar, L. S., W. E. Dietrich (2004). "A mechanistic model for river incision into bedrock by saltating bed load." *Water Resources Research*, 40(6): 063011-063021.
- Whipple, K.X. and Tucker, G.E. (1999). "Dynamics of the stream-power river incision model." *Journal of Geophysical Research*, 104: 17661-17674.

Whipple, K.X., G.S. Hancock, R.S. Anderson, (2000). "River incision into bedrock: Mechanics and relative efficacy of plucking, abrasion, and cavitation." *Geol. Soc. of America Bulletin*, 112(3): 490–503.

Modeling Erosion of an Unlined Spillway Chute Cut in Rock

Vlad Perlea¹, M. ASCE, Ph.D., P.E., David Mathews², M. ASCE, P.E., and Francke Walberg³, M. ASCE, P.E.

¹ U.S. Army Corps of Engineers, Sacramento District, 1325 J Street, Sacramento, CA 95814; PH (916) 557-5320; email: vlad.g.perlea@usace.army.mil

² U.S. Army Corps of Engineers, Kansas City District, 601 E 12th Street, Kansas City, MO 64106; PH (816) 389-3696; email: david.l.mathews@usace.army.mil

³ URS Corporation, 8300 College Blvd., Suite 200, Overland Park, KS 66210; PH (913) 344-1120; email: francke_walberg@urscorp.com

ABSTRACT

Discharges up to 1700 m³/s that lasted 21 days caused extensive erosion of the spillway chute excavated in rock at Tuttle Creek Lake, Kansas. Nearly 300 000 m³ of shale and limestone were eroded from the unlined chute resulting in a series of escarpments ranging in height from 1.20 to about 8 m. An empirical mathematical model, similar to a US Department of Agriculture model was developed for geologic conditions at Tuttle Creek Lake. This site specific model was used to evaluate the extent of erosion anticipated for future events and, based on this evaluation, to design the spillway repair. The model provides conservative results since it was conceived in such a manner as to over predict erosion. Initial attempts to generalize its use provided questionable results, but similar site specific procedures may be used in other locations for future events.

INTRODUCTION

A recent report by U.S. Society on Dams, Committee on Hydraulics of Dams (USSD 2006) identifies three major types of progression mechanisms of unlined spillways erosion:

- Headcut erosion, that occurs mainly in soils and sedimentary rocks, as present in Midwest United States; examples are Tuttle Creek spillway, Kansas, Milford spillway, Kansas, and Saylorville spillway, Iowa.
- Pothole scour, observed mainly in volcanic rock formations; an example is Painted Rock spillway, Arizona.
- Plunge pool scour, which may occur in any type of rock; a typical example is Bartlett spillway, Arizona, cut in granite.

This paper deals with the first category only and it is focused on the Tuttle Creek spillway case history, which apparently is the best documented case of headcut erosion.

TUTTLE CREEK SPILLWAY EROSION

Project and erosion event general descriptions

Tuttle Creek reservoir is a U.S. Army Corps of Engineers (USACE) Kansas City District (KCD) flood control project located in Eastern Kansas. It has a 24 937 km² watershed and an estimated maximum design outflow through the controlled

chute spillway of $17\,320\text{ m}^3/\text{s}$. The dam, designed and constructed in the 1950's, is a rolled-earth/rock fill embankment about 43 m high and 2 286 m in length. The spillway is located on the left abutment of the dam and consists of a concrete weir structure and an unlined chute. The weir structure is 256 m wide with 18 tainter gates 6 m high and non-overflow bulkheads. A reinforced concrete apron is as wide as the weir, 183 m in length and terminates with a flip bucket which includes a cutoff wall. Figure 1 shows an aerial photo of the spillway taken a short time after the erosion occurrence.

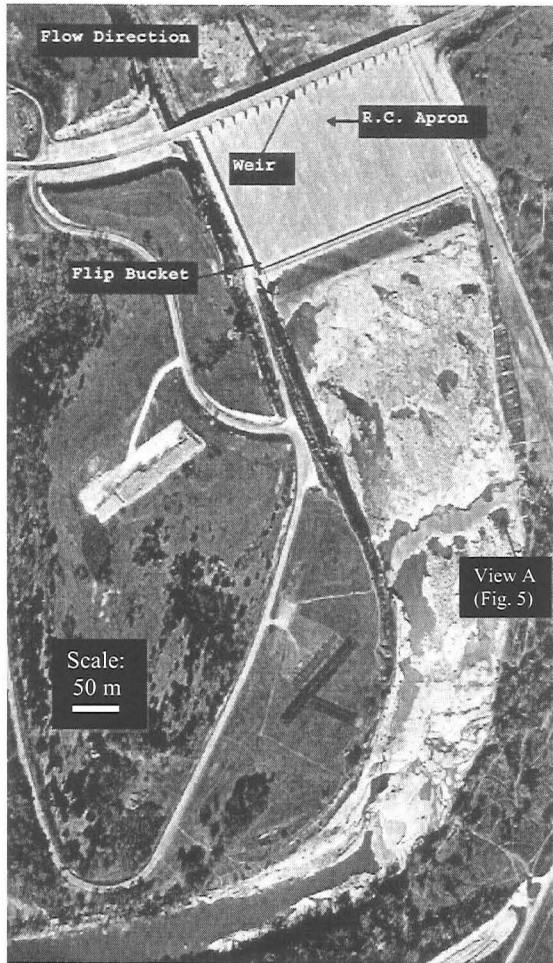


Figure 1. Post-erosion aerial photo of Tuttle Creek spillway.

The unlined chute was excavated 256 m wide at the flip bucket and narrows to only 61 m wide at the lower end. The chute drops over 26 m in elevation in a horizontal distance of 1 036 m. The average channel gradient is approximately 2.5 %. The chute is not straight but curves 90° to the right. The excavation encounters alternating limestone and shale units of variable thicknesses (see Table 1). The layers dip approximately 1 degree in the opposite direction as the channel bottom slope. The major limestone units are relatively durable and do not erode easily, however the shale units are generally soft and erodible. The unlined chute is susceptible to head cutting because erosion of the shales results in undermining of the erosion resistant limestones.

A major flood event, with an estimated 100-year return period, occurred in the summer of 1993. Discharges through the spillway occurred for the first time, after 30 years of operation of the project. Spillway releases lasted 21 days reaching a peak discharge of 1700 m³/s. Nearly 300 000 m³ of material were eroded resulting in a series of escarpments ranging in height from 1.20 m to about 8 m with some concentrated head cuttings. The design hydrograph, based on an estimated peak inflow of 22 640 m³/s, has the peak outflow of 17 320 m³/s (ten times greater than the 1993 flood event) and a duration of about 11 days (compared to 21 days in 1993). While this event was used for establishing the required size of the spillway, it should be understood that it may or may not be critical with respect to the assessment of the extent of erosion. The possibility of long duration events with smaller peak discharges must also be considered. In this respect, a model was developed to project anticipated erosion over the full range of discharges, based on site specific data from the 1993 spillway release and data from literature.

Area geology

The site geology is characterized by alternating layers of limestone and shale. The limestones are medium hard to hard and the shales are generally soft and laminated. Table 1 shows the simplified geologic column of the rock units encountered in the spillway.

The characterization of the rock units for hydraulic erodibility was made in accordance with the methodology developed at U.S. Department of Agriculture (USDA) by John Moore and Darrel Temple (Moore et al. 1994, USDA 1997).

Rock erodibility characterization

According to Moore et al. (1994) the spillway erosion process can be divided in three sequential phases for purposes of mathematical quantification:

- Phase I: Erosion resulting in the local failure of the vegetal cover, if any, and the development of the concentrated flow;
- Phase II: The downward and downstream erosion leading to the formation of a vertical or near vertical headcut, and
- Phase III: The upstream advance of the headcut with associated widening and deepening of the eroded volume.

In the case of Tuttle Creek spillway it is believed that the first two phases had a relatively short duration as compared with the third phase. Measurements of the headcut advance that were used in development and calibration of an erosion model

became available starting with the sixth day of discharge, when the erosion process was evidently in the third phase of development all along the unlined portion of the spillway. Therefore, only phase III parameters were evaluated and used in mathematical quantification of the spillway erosion.

Table 1. Geologic Column

Rock Unit	Rock Type	Layer Thickness (m)	Headcut Height (m)	Characteristic Parameters for Defining the Erodibility Index				
				UCS (MPa)	J_n	RQD	$J_{a,max}$	
Burr Legion	Limestone Shale	1.20 0.60	1.80 (No.1)	These geologic units were completely washed out				
Sallyards	Limestone	0.60	1.90	27.0	2.2	79.3	2	
Roca, Zone A	Shale	1.30	(No.2)	2.5	5.0	20*	4	
Roca, Zone B	Limestone	0.30	1,20	17.1	3.3	89.3	2	
Roca, Zone C	Shale	0.90	(No.3)	5.9	5.0	15*	6	
Roca, Zone D	Limestone	0.50	4.55 (No.4)	10.9	5.0	50*	4	
Roca, Zone E	Shale	1.50		11.4	5.0	40*	4	
Roca, Zone F	Limestone	0.35		7.4	5.0	25*	4	
Roca, Zone G	Shale	0.70		5.7	5.0	40*	4	
Roca, Zone H	Limestone	0.40		6.8	3.3	71.0	2	
Roca, Zone I	Shale	1.10		5.3	5.0	40*	4	
Howe Bennett	Limestone Shale	1.25 1.05		2.30 (No.5)	19.6	3.3	94.0	2
Glenrock Johnson, Zone A	Limestone	0.80		8.00 (Nos. 6 & 7)	45.7	2.7	95.0	2
	Shale	2.40			2.3	5.0	30*	4
Johnson, Zone B	Limestone	0.60	25.0		3.3	60*	4	
Johnson, C&D	Shale	2.10	6.7		5.0	45*	4	
Johnson, Zone E	Shale	0.60	8.4		5.0	50*	4	
Johnson, F&G	Shale	1.50	2.5		5.0	30*	4	
Long Creek, A	Limestone	0.90	4.05		28.3	3.3	91.1	2
Zones B&C	Limestone	2.15	(No.8)		20.4	3.3	90.0	2
Hughes Creek, A	Shale	1.00	12.4		3.3	40*	2	
Zone B Zones C&D	Limestone	0.80	3.00		26.6	3.3	70*	3
	Shale	2.20	6.4	3.3	40*	2		
Zone E	Limestone	0.60	1.70	23.8	3.3	50*	3	
Zone F	Shale	1.10	9.6	3.3	40*	3		

Notes: * Estimated values. Symbol definition (UCS, J_n , RQD, $J_{a,max}$) are given below.

According to Moore et al. (1994) the erodibility index (previously defined as excavatability index by Kirsten, 1982), K_h , represents a measure of the resistance of the material to erosion and has the general form:

$$K_h = M_s \cdot K_b \cdot K_d \cdot J_s \quad (1)$$

where:

M_s = material strength number of the earth/rock material. For rock, $M_s = 0.78 \cdot (\text{UCS})^{1.09}$ for $\text{UCS} \leq 10 \text{ MPa}$ and $M_s = \text{UCS}$ for $\text{UCS} > 10 \text{ MPa}$, where UCS is the unconfined compressive strength (ASTM D 2938). The UCS values resulted from laboratory tests on specimens taken from borings drilled in Tuttle Creek spillway are listed in Table 1.

K_b = block/particle size number. For fractured rock and rock-like materials the primary method of calculation of this parameter is $K_b = \text{RQD}/J_n$ where RQD = Rock Quality Designation and J_n = joint set number. RQD is a standard parameter in drill core logging and represents the sum of the length of the core pieces greater than 0.1 m divided by the total core run length (usually 1.5 m), expressed in percent. J_n is a scale factor representing the effect of different individual discontinuity spacings relative to the average discontinuity spacing; this factor accounts for the shape of the material units or, alternatively, the relative occurrence of different joint sets. For selection of the values listed in Table 1 detailed (unpublished) recommendations by Moore were considered; these recommendations are currently available in USDA, 1997.

K_d = discontinuity/inter-particle bond shear strength number. $K_d = J_r/J_a$ where J_r = joint roughness number, which represents the degree of roughness of opposing faces of a rock discontinuity, and J_a = joint alteration number, which represents the degree of alteration of the materials that form the faces. In accordance with Moore recommendations (USDA, 1997) J_r was assumed 1 for intact rock and 2 or 3 for weathered rock (2 for shale of Bennett and Hughes Creek Zones C&D formations, 3 for all the other rock units); J_a was also 1 for intact rock and 2 to 4 for weathered limestone and 3 to 6 for shale, as shown in the last column of Table 1. Based on the same USDA recommendations, the ratio $J_{r,\text{max}}/J_{a,\text{min}}$ was associated with the intact (unweathered) rock and the ratio $J_{r,\text{min}}/J_{a,\text{max}}$ with the weathered rock. This way, through K_d a range of K_h was defined, with the maximum value for the intact rock and the minimum value for the weathered rock.

J_s = relative ground structure number, which represents the orientation of the effective dip of the least favorable discontinuity with respect to stream flow. The number takes into account the effect of the relative shape of the material units (as determined by joint set spacings) on the ease with which the stream penetrates the ground and dislodges individual material units. For Tuttle Creek spillway $J_s = 0.88$ was determined, based on the following parameters, approximately valid for all rock units: Spillway Flow Direction = 135 azimuth degrees; Bedrock Strike = 330 azimuth degrees; Bedrock Dip Direction = 240 azimuth degrees; Rock Dip = 1 degree.

Flood Event and Erosion Monitoring

Releases were gradually increased during a 4-day period until they reached the peak discharge at of 1 700 m³/s. Without any further change in gate opening, the discharge gradually decreased to zero during the following 17 days. An aerial photo at the end of releases is presented in Fig. 1 and the profile along the most eroded zone, before and after spillway releases, in Fig. 2. Fig. 3 shows the general view of the spillway during releases and soon after they stopped.

By comparing contours determined from aerial photos before and after the flow through the spillway, the total eroded distance along each headcut was

determined. The measured erosion was defined as the horizontal distance along the middle of the hard layer at the top of the escarpment as illustrated in Fig. 4.

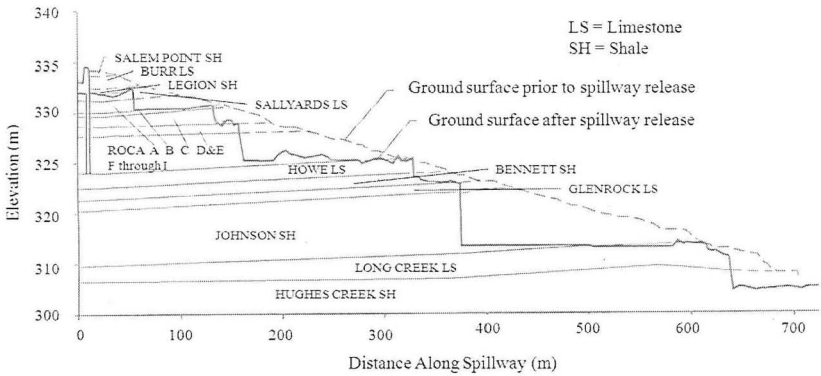


Figure 2. Profile along right side of Tuttle Creek spillway. (Both horizontal and vertical scales are in feet; 1 foot = 0.3048 m)

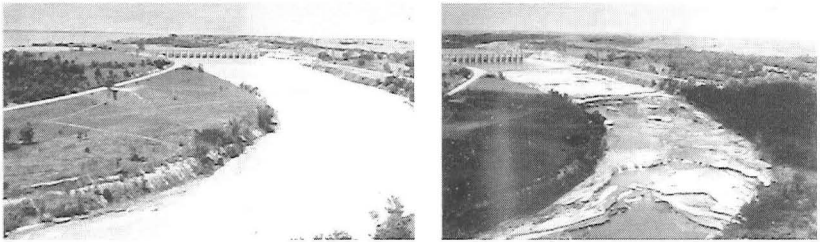


Figure 3. General view of Tuttle Creek spillway: left, during 1993 releases; right, immediately after releases stopped.

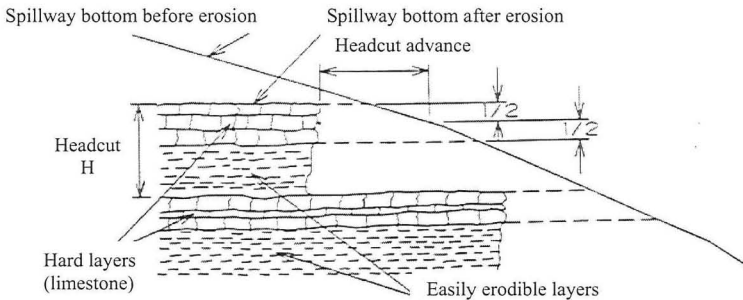


Figure 4. Scheme of spillway erosion.

The headcut erosion was not uniform. The advance was relatively high at weak points and at other locations the erosion was minimal. All headcuts had a relatively hard layer (limestone) on top and easily erodible rock underneath. Fig. 5 presents a characteristic headcut, during and after releases.

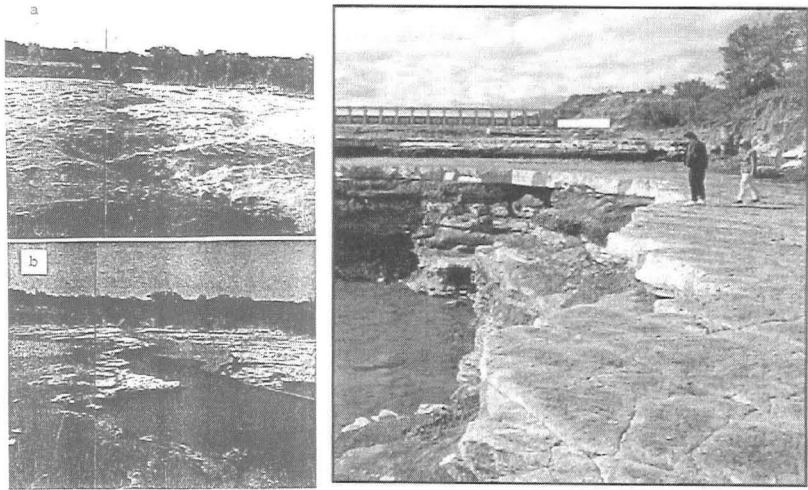


Figure 5. Headcuts 5, 6&7: left: (a) during releases – 8/3/1993; (b) after releases – 8/9/1993; right: one of the highest headcuts (view A on Fig. 1).

During the releases daily photographs were taken at nine different sites along the spillway, to document regression of headcuts. Based on these photos the erosion advance in the upstream direction was estimated at selected knick points on top of the headcuts, where the flow was visibly affected by the ledge. This method of estimating the erosion rate was somewhat inaccurate, but provided reasonable determination of average erosion rate for periods of time varying between 4 and 16 days. The estimation of average rates and associating them to the average unit discharge (as defined later) and to various degrees of rock weathering (shown in bold in Table 2) is illustrated in Fig. 6. See also Table 2 for corresponding data.

Early in the erosion process escarpments took shape, with hard (limestone) layers on top and soft (mostly shale) layers underneath. The aggregate headcut erodibility index was calculated with the formula (Temple and Moore, 1994):

$$K_h = \exp[\sum h_i \ln(K_{hi}) / (\sum h_i)] \quad (2)$$

where

K_{hi} = Erodibility index of each rock unit exposed by the headcut;
 h_i = Thickness of each rock unit exposed by the headcut.

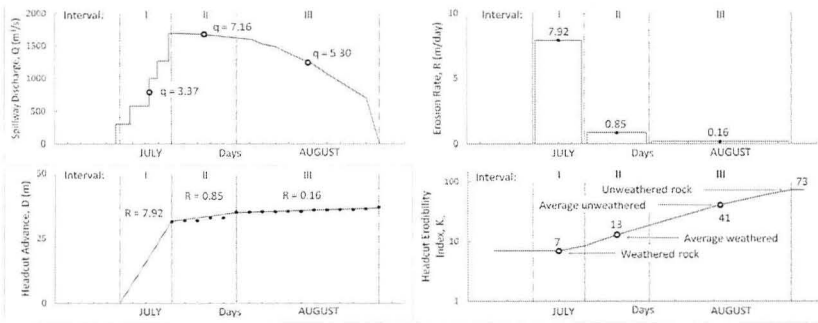


Figure 6. Headcut (No. 3) advance characterization per three time intervals: left – relating the average unit discharge, q to average erosion rate, R ; right – relating the average erosion rate, R to the degree of rock weathering.

Table 2. Monitoring results and associated headcut characterization (in bold)

Headcut No.	Rate of Headcut Advance (m/day)					Headcut Erodibility Index, K_h				
	Initial		Intermediate		Final	Initial		Intermediate		Final
	1	2	3	4	5	6	7	8	9	10
1	Not measured					Layers completely washed out				
2	9.45			0.12		10	17	30	53	95
3	7.92	0.85		0.16		7	13	23	41	73
4	12.2	9.94	1.22	0.37		14	26	48	89	160
5	4.72			0.06		15	26	45	76	130
6	Headcuts that were already combined when monitoring started					15	27	47	-	-
7						8	14	26	-	-
6+7		3.05		1.58		9	17	31	57	100
8+9	Not measured					100	160	240	370	580

Notes: The “initial” values of headcut K_h (column 6) correspond to highly weathered rock and the “final” values (column 10) to the practically unweathered rock. Between them are “moderately weathered”, “somewhat weathered”, and “slightly weathered” (columns 7, 8, and 9) based on a logarithmic equation and that were correlated with corresponding rates of erosion (columns 2, 3, and 4, respectively).

Mathematical modeling of headcut advance

The most comprehensive model of headcut advance at the time of Tuttle Creek spillway erosion event was that developed by Temple and Moore (published 1994). However, because that model was based mostly on spillways excavated in soil, it did not fit the data obtained from erosion monitoring at Tuttle Creek. Therefore, a site specific model was developed using Tuttle Creek data. In the development of the KCD (Kansas City District) model the general form of the USDA equation was assumed:

$$R = C [(qH)^{1/3} - T^{1/3}] \quad (3)$$

where

R = the rate of headcut advance in the upstream direction (m/day);

C = parameter function of K_h ;

K_h = the aggregate headcut erodibility index; when a headcut downstream has a higher erosion rate than the headcut above it the two headcuts combine and K_h changes accordingly;

$q = Q/L$ = unit discharge, the volume of flow over the headcut per units of width and time ($m^3/s/m$); Q is the spillway discharge and L the length of the headcut, which may change significantly due to uneven erosion across the spillway;

H = the drop in the energy grade line as the flow passes over the headcut, approximately equal to the headcut height (m); it changes when two or more headcuts combine due to their different rate of advance;

T = threshold energy required to generate headcut advance.

First the threshold T was determined based on observed discharges that did not induce significant erosion; after that C was estimated based on data in Table 2:

$$R \text{ (m/day)} = \exp[3.77 - 0.57 \ln(K_h)] \cdot [(qH)^{1/3} - 0.361 (K_h)^{1/2.25}] \quad (4)$$

Details of the model derivation are presented elsewhere (Perlea and al., 1997).

Benefits of KCD spillway erosion model

The model was used by the KCD to evaluate the potential breach of the spillway during future flood events. Parametric studies included:

- Various types of discharge hydrographs, including the 1993 discharge hydrograph and the design outflow hydrograph;
- Different longitudinal profiles along the eroded spillway, including a regraded profile to minimize initial concentration of flow;
- Two variants with respect to degree of weathering: (1) unweathered rock, condition believed to occur immediately after 1993 erosion; and (2) weathering to approximately the same extent as existed before the 1993 event, i.e. after decades of exposure to atmospheric weathering factors.

It was concluded that the spillway can likely withstand the spillway design flood (peak discharge of $17\,320 \text{ m}^3/\text{s}$) without loss of the concrete weir structure caused by erosion of the unlined chute. Long duration low flow events may represent more significant risk than the spillway design event. However, the erosion model indicated that a continuous flow of $1\,420 \text{ m}^3/\text{s}$, similar to that of 1993, could threaten the weir structure only after a duration of 50 to 70 days, depending on the extent of rock weathering in the unlined chute. Such an event would be extremely rare.

These findings provided increased confidence in the expected future performance of the spillway and led to the design of a quite economical interim repair, based on protection of the rock for preventing weathering and preventing concentration of flow at the beginning of a future flood event by filling the existing knick points with grouted rock fill. A description of the spillway repair is published elsewhere (Mathews et al., 1998).

ATTEMPTS OF GENERALIZATION OF KCD MODEL

Attempts to apply the KCD erosion model to other documented case histories failed. The few USDA cases for spillways cut in rock had the erosion rate significantly overestimated. However, in the case of the Saylorville spillway, most of the observed erosion rates were significantly larger than predicted, even though the model had been conceived to overpredict erosion rates.

The KCD model was modified by the USACE Engineer Research and Development Center (ERDC), as presented in USSD, 2006. ERDC considered more observation records, in an attempt to generalize the model. Like the KCD model, the ERDC model still overpredicts rates included in USDA bank of data but severely underpredicts Saylorville spillway erosion rates; in addition, the ERDC model underpredicts the Tuttle Creek data.

It is believed that a major aspect that makes a general model difficult to create is that an average discharge and an average erosion index do not adequately represent the erosion process. In addition the rock mass parameters which lead to the erosion index are usually subjective and widely variable. However it is believed that a credible site-specific model, useful for design, can be developed.

CONCLUSIONS

The currently available data does not allow preparation of a suitably reliable general model for sedimentary rock erosion. Existing models, when used, must be used with caution and considerable judgment. Fortunately, with attention to available spillway design criteria (Walberg et al 1995) there is a very low probability for the first release to be catastrophic, thus there is usually an opportunity to develop a site specific model for spillway rehabilitation design, similar to the KCD model presented in this paper.

REFERENCES

- Kirsten, H.A.D. (1982). "A Classification System for Excavation in Natural Materials." *Civil Engineer in South Africa*, Vol.24, No.7 (July): 293-308.
- Mathews, D.L., Perlea, V.G., Walberg, F.C., and Anderson, D.R. (1998). "Erosion and Repair of Unlined Spillway Chute Excavated in Rock." Fourth Int. Conf. on Case Hist. in Geotech. Engrg, St. Louis, MO, USA, Paper No. 6-05.
- Moore, J.S., Temple D.M., and Kirsten, H.A.D. (1994). "Headcut Advance Threshold in Earth Spillways." *Bull. Assoc. Engineering Geologists*, Vol. XXXI, No. 2.
- Perlea, V.G., Mathews, D.L., and Walberg, F.C. (1997). "Rock Erosion of Unlined Spillway Chute." 19th Congress on Large Dams, Florence, Italy: 153-172.
- Temple, D.M. and Moore, J.S. (1994). "Headcut Advance Prediction for Earth Spillways." *Am. Soc. Agr. Engrs.*, Paper No. 942540, presented at the 1994 ASAE International Summer Meeting, Spocane, Washington, USA.
- USDA (1997). "Field Procedures Guide for the Headcut Erodibility Index." Chapter 52, Part 628 Dams, *Nat. Engrg Handbook*, 210-VI-NEH, rev. 1, 2001, 33 p.
- USSD (2006). "Erosion of Unlined Spillways." Prepared by U.S. Society on Dams, Committee on Hydraulics of Dams, Denver, CO, 183 p.
- Walberg, F.C., Mathews, D., Hoyt, J., Huffman, C., and Dridge, R., (1995) USCOLD, 15th Annual Meeting and Lecture: 113-131.

90 Years of Erosion and Deposition on the Trinity River, Dallas, Texas

Mark Tompkins¹, PhD., P.E., Gregory Ajemian², P.E., Anthony Falzone³, Jeremy Thomas⁴, Paul Frank⁵, P.E., and Kyle Winslow⁶, PhD., P.E.

¹NewFields River Basin Services, 1668 Capistrano Avenue, Berkeley, CA 94707; PH (510) 558-0192; email: mtompkins@newfields.com

²City of Dallas, 1500 Marilla, Room 6B\South, Dallas, TX 75201, PH (214) 671-9504; email: gregory.ajemian@dallascityhall.com

³NewFields River Basin Services, 1668 Capistrano Avenue, Berkeley, CA 94707; PH (415) 713-5855; email: afalzone@newfields.com

⁴NewFields River Basin Services, 1668 Capistrano Avenue, Berkeley, CA 94707; PH (510) 919-5402; email: jthomas@newfields.com

⁵CH2M Hill, 155 Grand Avenue, Suite 100, Oakland, CA 94612, PH (510) 622-9100; email: paul.frank@ch2m.com

⁶CH2M Hill, 402 West Broadway, San Diego, CA 92101, PH (619) 687-0110; email: kyle.winslow@ch2m.com

ABSTRACT

The City of Dallas has initiated a design to realign and naturalize an eight mile reach of the Trinity River near downtown that has been relocated, channelized, and straightened over the past 90 years. As part of the channel realignment design process for the Trinity River Corridor project, we conducted historical geomorphic analyses, field measurements of bank erosion and floodplain sediment deposition, and numerical modeling of hydraulic and sediment transport characteristics of the river. Our analyses of bank erosion and lateral channel migration showed limited, localized erosion and relatively low rates of lateral migration. We also determined that the channel has maintained a dynamic equilibrium through a process of localized bank erosion and “repair.” Field measurements of deposition rates and topographic analysis of historical floodplain sedimentation showed that there has been limited systematic deposition on the floodplain. These findings provided a critical foundation for the design of the Trinity River Corridor project.

Keywords: bank erosion, channel migration, flood protection, floodplain deposition, Trinity River

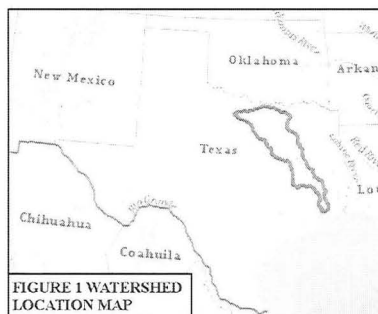
INTRODUCTION

The Trinity River in Dallas, Texas has experienced extensive change over the past century. The most rapid and widespread changes occurred during the construction of the original Dallas Floodway project in the late 1920s and the United States Army Corps of Engineers (USACE) reconstruction of the floodway in the 1950s. The proposed channel realignment element of the Trinity River Corridor Project will result in perhaps the most significant change to the Trinity River since the 1920s-era Dallas Floodway project. The Balanced Vision Plan for the Trinity River Corridor (City of Dallas, 2003) calls for restoration of channel meanders, creation of a mid-channel island, alterations to channel geometry, and general enhancement of aquatic and riparian habitat throughout the corridor, in addition to a wide variety of

recreational, aesthetic, transportation, and other elements. In this paper we describe analyses of historical channel change, bank erosion and repair, bed material composition, and floodplain sedimentation analyses used to guide design of the river channel realignment element of the Trinity River Corridor Project.

HYDROLOGY AND GEOLOGY

The project area begins just downstream of the confluence of the Elm and West Forks of the Trinity River where the contributing watershed area is approximately 6,100 square miles (Figure 1). The climate is characterized as humid subtropical with hot summers and relatively mild winters. Average annual rainfall in the watershed is between 30 and 40 inches, and much of the annual precipitation occurs during thunderstorms, with occasional intense storms in the late spring and early summer. Discharge and stage in the Dallas change rapidly in response to precipitation in the urbanized watershed.



Peak floods influenced many facets of the final channel realignment design, including erosion control measures, riparian vegetation planting schemes, recreational features, and operation and maintenance requirements. The largest annual peak flood in the Trinity River (184,000 ft³/sec) occurred on May 26, 1908, during which the river was over 2 miles wide between West Dallas and downtown Dallas (Furlong et al., 2003). The smallest annual peak flood (4,540 ft³/sec) occurred on May 28, 1978. Table 1 summarizes results from the flood frequency analysis conducted for the Trinity River at USGS gage #0805700 for the entire period of record as well as both pre- and post-1955 periods to illustrate the influence of upstream reservoirs on peak flows.

Table 1. Flood Frequency Analysis Results USGS Gage #08057000 (Trinity River at Dallas) for the period of record 1903 to 2007

Flood Flow Return Period (Years)	Complete Data Set Flood Discharge (ft ³ /sec)	Complete Data Set Water Surface Elevation (ft)	Pre-1960 Flood Discharge (ft ³ /sec)	Pre-1960 Water Surface Elevation (ft)	Post-1960 Flood Discharge (ft ³ /sec)	Post-1960 Water Surface Elevation (ft)
1	3752	390.8	3122	389.7	4891	392.5
1.4	13307	400.2	12882	399.9	14320	400.8
1.5	14805	401.1	14517	401.0	15711	401.7
2	20845	404.4	21292	404.6	20988	404.4
5	41103	411.7	45497	412.9	36060	410.2
10	58937	416.2	68055	418.1	47247	413.4
20	79594	420.3	95188	422.9	58678	416.2
50	111970	425.4	139317	428.9	74370	419.4
100	140836	429.1	179939	433.3	86751	421.6
200	173957	432.7	227725	437.6	99605	423.6
500	225073	437.4	303474	443.2	117347	426.1

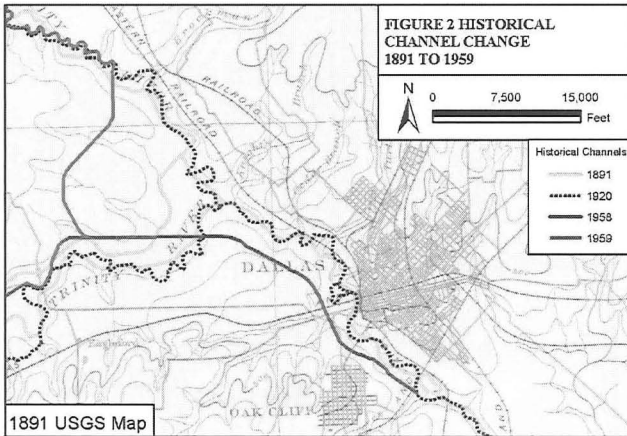
Geology

The project area lies in the Blackland Prairies geologic province which is characterized by low rolling terrain with chalk and marl bedrock formations. Upstream of the project area, the Trinity River drains the Grand Prairie province's low "stair-step" hills and flat plains underlain by calcareous and sandy bedrock. The uppermost reaches of the Trinity River watershed are in the North Central Plains province characterized by low north-south ridges with limestone, sandstone, and shale bedrock. The channel and floodway in the Project area are composed of alluvium consisting of sand, mud, and sparse gravel (Dallas Geological Society 1965 and Bureau of Economic Geology 1992, 1996, and 1999).

HISTORICAL CHANNEL ALIGNMENT CHANGE

To illustrate changes in channel alignment, we obtained, rectified, and analyzed historical topographic maps in a Geographic Information System (GIS). Figure 2 shows the 1891, 1920, and 1959 historical channel centerlines. The major change in the channel alignment between 1891 and 1920 is the channel confinement and secondary channel disconnection that occurred when a levee was constructed between the West and Elm Forks of the Trinity River. Between 1920 and 1959, the channel was straightened and the confluence of the Elm and West Forks was relocated 3.5 miles to the west (Furlong et al., 2003). Remnants of the old channel remain and connect tributaries to the pump stations that pump stormwater discharge from the tributaries into the Dallas Floodway. Within the floodway, the channel

alignment from the 1928 project changed only slightly during reconstruction of the floodway from 1953 to 1960.



Bank Erosion

Initial observations from field reconnaissance in the floodway and review of aerial photographs identified bank erosion as an important channel process influencing long-term channel form. To determine the extent of bank erosion along the channel banks in the project area, we analyzed the 2005 aerial photographs in GIS and digitized areas of bank erosion as either “fresh” (an erosional surface that had not been revegetated), or “vegetated” (an erosional surface that had been revegetated). The 2005 aerial photographs were taken during a year of high peak flows (25,600 ft^3/sec on June 12, 2004, and 23,000 ft^3/sec on July, 30, 2004), and many of the erosion sites observed in the aerial photographs were likely impacted by these high flows. Peak daily flows of 35,700 ft^3/sec (March 20, 2006), 35,700 ft^3/sec (June 28, 2007), and 25,400 (March 19, 2008) occurred between the date of the aerial photos and the field verification. Because these high-flow events could have created additional erosion sites or scoured vegetation from channel banks, we field verified mapped erosion areas on aerial photographs and field maps and later digitized these observations in GIS.

We measured significant areas of bank erosion downstream of any deviation in channel alignment, and at the downstream banks of stormwater outfall channels. Eroded banks had an average erosion depth of approximately 10 ft and a linear extent between 10 and 20 ft. The average volume of active bank erosion per site was 5,967 ft^3 and a total of 35,2674 ft^3 of bank material had been removed from the active erosion sites upstream of Sylvan Avenue (Figure 3).



We observed a pattern of bank erosion and repair by vegetation recruitment and deposition throughout the project area. At channel bends, pump station outfall channels, and flow obstructions such as bridge piers or large woody debris, strong eddies scour the bank and cause bank erosion along the existing channel. Pore pressure from rapidly receding peak flows may also cause bank failures and contribute to bank erosion along the existing channel. However, we observed widespread sediment deposition along eroded banks and subsequent vegetation recruitment and growth (which further decreases the velocity of flow over the eroded surface and increases sediment deposition rates). This phenomena appears to contribute significantly to the low lateral migration rates we measured by comparing historical channel margins. Figure 4 is a conceptual model that depicts the cycle of bank erosion and repair in the project area, and Table 2 is a summary of lateral channel migration rates in the project area. While a detailed investigation of channel erosion was not conducted in the Great Trinity Forest downstream of the project area, similar bank erosion and repair was observed along the channel in that reach.

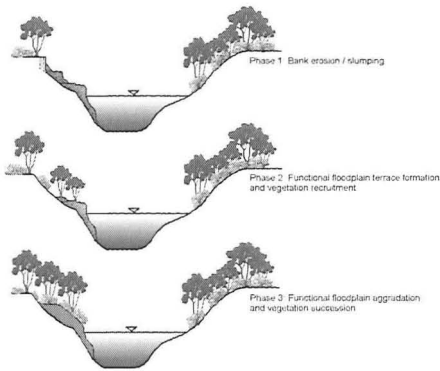


Figure 4: Conceptual model of bank erosion and natural “repair” through sediment deposition and revegetation

Table 2. Reach Average Migration Rate and Maximum and Minimum Bank Migration

Reach	Period of Analysis	Average Migration (ft)		Average Migration Rate (ft/yr)		Maximum Migration Rate (ft/yr)		Minimum Migration Rate (ft/yr)	
		Left Bank	Right Bank	Left Bank	Right Bank	Left Bank	Right Bank	Left Bank	Right Bank
Confluence to 1,500 ft Upstream of Hampton	1930-2005	19	65	0.25	0.87	0.56	2.13	0.01	0.17
1,500 ft Upstream of Hampton to Sylvan Street Bridge	1965-2005	26	21	0.64	0.52	1.88	2.58	0.10	0.05
Sylvan Street Bridge to Houston Street Viaduct	1965-2005	55	35	1.37	0.87	3.20	2.93	0.03	0.00
Houston Street Viaduct to DART Bridge (Multistage Channel)	1965-1984	22	26	1.14	1.35	3.95	3.58	0.05	0.16
DART Bridge to Highway 45 (Great Trinity Forest)	1965-2005	32	37	0.80	0.93	2.28	2.60	0.03	0.03

FLOODPLAIN SEDIMENTATION

Sediment transport

The Trinity River has a high suspended sediment concentration of approximately 920 milligrams per liter (mg/L) at the bankfull flow of 13,000 ft³/sec, and a sediment transport rate of over 28,000 tons/day at that same flow. Overbank flows deposit significant quantities of silt in floodplain depressions, potentially requiring regular sediment management on trails, road surfaces, and other Project design features. There have been no significant channel migration problems documented in the last 50 years within the Project reach that would indicate that there has been a net loss of sediment from the Project reach transported either by normal daily flows or by flood events. The apparent stability of the channel in the Project reach and minor changes in the overbank topography in undisturbed areas also indicate that any sediment being supplied from the Dallas Floodway area is being transported through the project reach without significant deposition.

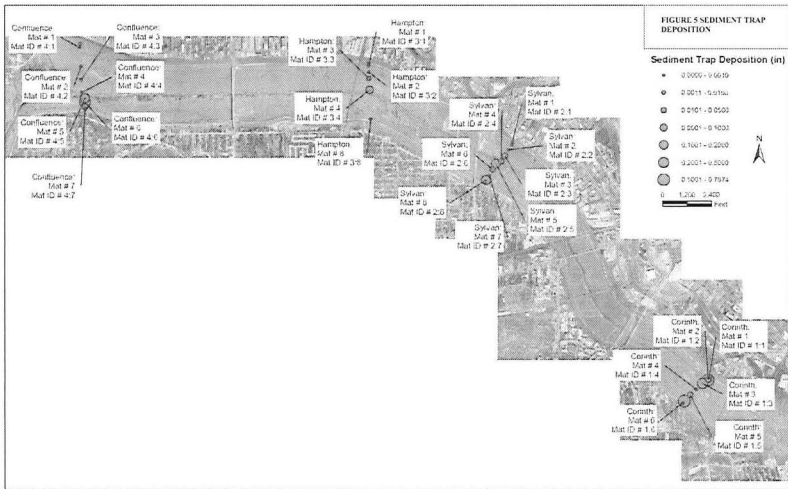
Sediment Traps

Because the suspended sediment load in the Trinity River is relatively high, an understanding of the rate of sediment deposition on the floodplain is critical to the design of and planning for Project features and maintenance on the floodplain. We placed sediment traps, consisting of 1.5 ft square artificial turf patches, along transects on the active floodplain to quantify sediment deposition. This method has been shown to be the most cost-effective means of riparian sedimentation analysis in a recent study of methods for quantifying contemporary sediment deposition within water bodies and their margins (Steiger et al., 2003). We established four cross sections along the Project reach with two to five sediment traps placed on the floodplain on each side of the channel (Figure 5). We deployed the sediment traps in the following configuration: one sediment trap at the top of bank floodplain terrace, one sediment trap proximate to the levee toe, and up to three sediment traps on the floodplain.

We revisited sediment traps after flows overtopped the channel banks (typically flows greater than approximately 13,000 ft³/sec) and measured average sediment deposition in quadrants on each trap. Two overbank flows recorded at the USGS Trinity River at Dallas, Texas gage (08057000) occurred on April 25, 2008 (14,300 ft³/sec) and June 12, 2009 (30,700 ft³/sec). The April 25, 2008 peak discharge overtopped the channel banks but did not inundate the entire floodplain. The larger June 12, 2009 peak discharge resulted in higher flows on the floodplain. We checked the sediment traps in the field on May 2, 2008, after the 14,300 ft³/sec discharge event. Because the peak discharge did not completely inundate the floodplain, the sediment traps at the upstream most transect near the confluence and the sediment traps on the west/right bank near Sylvan Bridge were not checked. Six sediment traps were not located. Of the thirteen sediment traps that were relocated, only one had measurable sediment after the April 25, 2008 event. Sediment trap 1:2 is located on a terrace between the low flow channel and the floodplain on the Corinth Transect and 127.6 in³ of sediment covered 2/3 of the sediment trap. The remaining twelve sediment traps had an immeasurable dusting of silt.

We checked the sediment traps a second time after the June 12, 2009, 30,700 ft^3/sec event. This event inundated the floodplain from the downstream most transect near the Corinth Street Bridge to the upstream most transect near the confluence. Of the 29 sediment traps deployed, 24 were relocated. Sediment trap 1:2 was deployed on a low bench and may have been washed away or buried with sediment. Sediment traps 3:5, 3:6, and 3:7, were not located. Of the 24 relocated sediment traps, 14 were covered with a measurable amount of sediment. The remaining ten sediment traps only contained an immeasurable dusting of sediment that was too small to measure. The volume of sediment deposited on the sediment traps ranged from 0.03 in^3 to 5.58 in^3 .

To illustrate sediment deposition patterns on the floodplain, we plotted the locations of the sediment traps on a base map with graduated symbols and scaled the symbol sizes proportional the volume of deposited sediment. Figure 5 shows the volume (in cubic inches) of deposited sediment divided into seven categories (0-0.01, 0.02-0.10, 0.11-0.50, 0.51-1.00, 1.01-2.50, 2.51-6.00, 6.01-127.56). Sediment deposition was concentrated at the top of bank of at least one bank of the active channel at each transect. Sediment deposition also occurred close to the toe of the levee on the right/west bank at the Confluence, Sylvan, and Corinth transects. The largest amount of deposited sediment was observed on the low flow bench at the Corinth transect.



We compared observed sediment deposition downstream of Westmoreland to the existing conditions sediment transport model results for a 24 hour flow at 25,000 ft^3/sec to validate model performance. Figure 6 shows the location of the sediment traps for the downstream three transects and the sediment transport modeling results downstream of Westmoreland. In general, the model shows deposition at the channel margins, near the toe of the levees, downstream of outfall channels, and across the floodplain immediately downstream of Westmoreland. The existing conditions

REFERENCES

- Bureau of Economic Geology, 1997. Existing reservoirs from the 2001 State Water Plan. Digital data provided by, Texas Water Development Board. <http://www.twdb.state.tx.us/mapping/gisdata.asp> Assessed July 25, 2007.
- Bureau of Economic Geology 1992, 1996, and 1999 Texas maps
- City of Dallas. A Balanced Vision Plan for the Trinity River Corridor. (2000). Retrieved on January 14, 2010 at http://www.trinityrivercorridor.org/html/vision_plan.html.
- Dallas Geological Society 1965 Dallas County geologic map
- Environmental Systems Research Institute. 2007. ArcInfo 9.2 [software]. Redlands, California: Environmental Systems Research Institute.
- Furlong, J.N., G.A. Ajemian, and T. McPherson. 2003. History of the Dallas Floodway. American Society of Civil Engineers, Texas section meeting, Dallas, Texas. September.
- Smelser, M.E. and J.C. Schmidt. 1998. An assessment methodology for determining historical changes in mountain streams. U.S. Forest Service General Technical Report RMRS-GTR-6, 29 p.
- Steiger, J., A.M. Gurnell, and J.M. Goodson 2003. Quantifying and characterizing contemporary riparian sedimentation. *River Research and Applications*, 19: 335-352.

2-D Pore-Particle Scale Model of the Erosion at the Boundary of Two Soils Under Horizontal Groundwater Flow

M. Chekired¹ and V. Roubtsova¹

¹ Institut de recherche d'Hydro-Quebec, Expertise Robotique et Civil, 1740 boul. Lionel-Boulet, Varennes (Quebec) J3X 1S1

ABSTRACT

Modeling particle-fluid systems in porous media encountered in many scientific and engineering applications presents a significant challenge. This paper outlines a hydrodynamic flow at a low Reynolds number through saturated porous media which is generated virtually using only the grain-size distribution curves of soils. In order to represent the pore and granular structures of soils, a novel model was developed using a fractal approach. For a given porosity, particle and pore size distributions were successfully modeled for a wide range of soils. We tested the model's conductivity behaviour by carrying out a steady-state flow through a fractal structure. Soil particle movement was modeled using the discrete element method (DEM), and the hydrodynamic flow was simulated by the well-known marker-and-cells (MAC) method, with special conditions imposed at the particle boundaries. The fluid-particle interaction was taken into account in our calculations using the method of direct force integration at the surface of particles. Several comparisons of our numerical results to those of published experiments for particle-particle and particle-wall interaction in a viscous fluid show very good agreement. Finally, an example of a possible erosion scenario at the interface of two different soils under a horizontal flow is presented. The results and a discussion of this model's applicability are also presented. This study is a part of an extensive program which includes 3-D simulations aimed at gaining a better understanding erosion phenomena in soils made up of irregularly shaped particles under hydrodynamic flow.

1. Introduction

Microscopic numerical analysis can be an effective tool to study the phenomenon of internal erosion. Pore-scale models of viscous fluid flow based on the Navier-Stokes equations take in account such details as the real water velocity and the water pressure in the pore channels. With this flow pattern, it is possible to calculate the real drag force, which is a primary factor determining the erosion threshold. The interaction between soil particles is integrated into the model.

2. Fractal scaling of soil particle-size distributions

A detailed study of the pore solid fractal (PSF) model was conducted by Perriers et al. (1999). The generation of a PSF model starts with the initiator which consists of a square of length L in 2-D. This square is divided into R^2 sub squares with length L/R , R being the scaling factor. The sub squares present the pores (P), particles (S), and unspecified elements ($F = R^2 - P - S$) that will be devised in the next iteration step. All unspecified elements will be assigned to pores for the last iteration.

This model was extended by combining three fractal processes in series (3G-PSF) by Lehmann et al. (2003). Each generator was applied for a certain number of iterations. A more realistic model is obtained by changing the solid squares to solid round particles (see Figure 1).

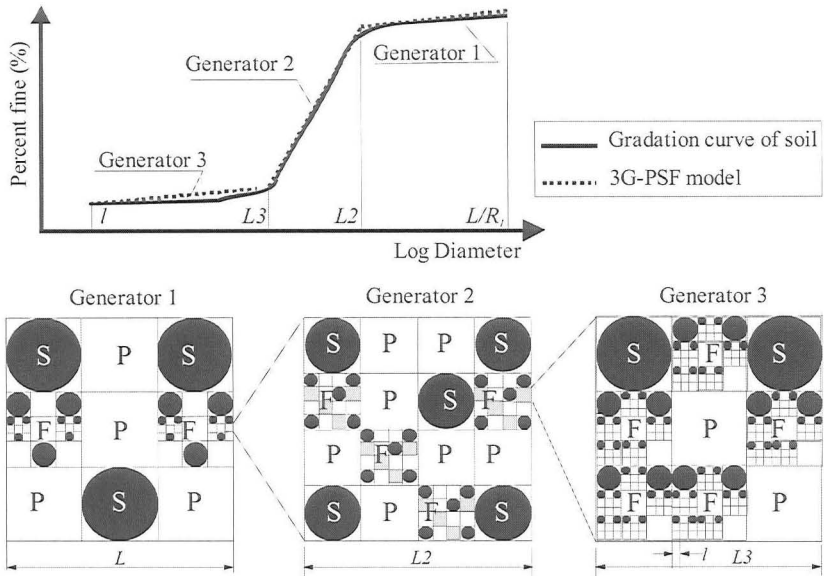


Figure 1. Construction of a 3G-PSF with round particles.

For the first generator: $R = 3$, $S = 3$, $P = 4$, and $n = 3$; for the second generator: $R = 4$, $S = 5$, $P = 7$, and $n = 2$; and for the third generator: $R = 3$, $S = 2$, $P = 2$, and $n = 3$.

After a number of iterations, the porosity is found as follows:

$$\phi_{n_1+n_2+n_3} = \frac{P_1 + (1 - 0.25 \times \pi)S_1}{P_1 + S_1} \left(1 - \left(\frac{F_1}{R_1^2} \right)^{n_1} \right) + \left(\frac{F_1}{R_1^2} \right)^{n_1} \frac{P_2 + (1 - 0.25 \times \pi)S_2}{P_2 + S_2} \left(1 - \left(\frac{F_2}{R_2^2} \right)^{n_2} \right) + \left(\frac{F_1}{R_1^2} \right)^{n_1} \left(\frac{F_2}{R_2^2} \right)^{n_2} \frac{P_3 + (1 - 0.25 \times \pi)S_3}{P_3 + S_3} \left(1 - \left(\frac{F_3}{R_3^2} \right)^{n_3-1} \right) + \left(\frac{F_3}{R_3^2} \right)^{n_3-1} \left(\frac{P_3 + F_3 + (1 - 0.25 \times \pi)S_3}{R_3^2} \right) \quad (1)$$

where the indices 1, 2, and 3 correspond to the first, second, and third generators respectively. n is the number of iterations.

The best approximation of gradation curves associated with a given porosity determines the parameters of the generators. A specific algorithm dedicated to ensuring a flow path was used.

Different particle locations can be generated randomly with the same parameters of 3G-PSF model. A comparison of the particle size distribution of various soil samples with those obtained by fractal modeling is shown in Figure 2.

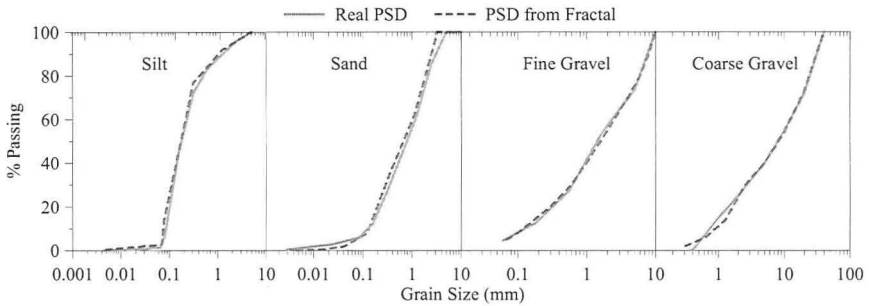


Figure 2. Comparison of PSD for various soil samples with those obtained from the fractal model.

3. Flow through generated soils

The water flow through a pore channel is described by the Navier-Stokes equations for viscous-incompressible liquids, and is expressed by:

$$\rho \left[\frac{\partial \bar{v}}{\partial t} + (\bar{v} \nabla) \bar{v} \right] = -\nabla p + \eta \nabla^2 \bar{v} + \bar{f} \quad (2)$$

$$\nabla \bar{v} = 0$$

where ρ is the density of the liquid (kg/m^3), t is the time (s), \bar{v} is the flow velocity (m/s), p is the water pressure (Pa), η is the dynamic viscosity (Pa·s), and \bar{f} is the force of gravity (N).

We chose the well-known marker-and-cell (MAC) method to solve this system of equations (Harlow and Welch (1965)).

The coefficient of permeability (m/s) for this soil sample is (Scheidegger (1963))

$$K = - \frac{\langle v \rangle s \rho g}{\Delta p}$$

where $\langle v \rangle$ is the average velocity in the soil (m/s), s is the length of the sample in the direction of flow (m), and Δp is the pressure difference at the boundary (Pa).

The hydrodynamic flow through four different soil samples generated by the fractal model is presented in Figure 3. Comparison of porosity and the coefficient of permeability calculated from the fractal model and from the empirical formula for different soils is presented in Tables 1 and 2 respectively.

The empirical porosity of the soil was calculated by $\phi = 0.255(1 + 0.83^U)$ (Vukovic and al. (1992)), where $U = d_{60}/d_{10}$ is the coefficient of grain uniformity, d_{60} and d_{10} represent the grain diameter in mm at which 60% and 10% grains are finer respectively. The porosity of the fractal model was calculated using equation 1.

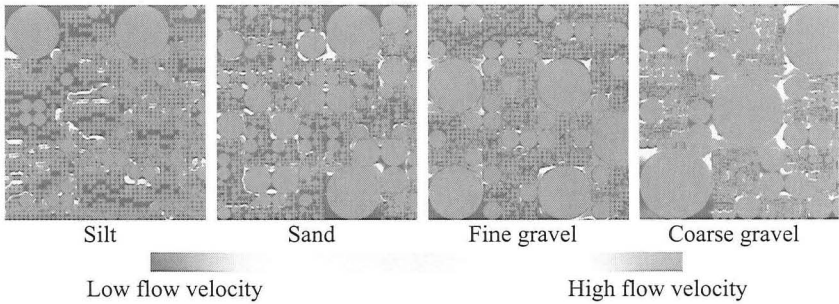


Figure 3. Hydrodynamic flow through generated soils

Table 1. Comparison of porosity

	Silt	Sand	Fine Gravel	Coarse Gravel
Empirical	0.406	0.303	0.261	0.268
Fractal	0.405	0.314	0.265	0.279

Table 2. Comparison of coefficient of permeability (m/s)

		Silt	Sand	Fine Gravel	Coarse Gravel
Empirical		$1.07 \cdot 10^{-04}$	$2.03 \cdot 10^{-04}$	$2.17 \cdot 10^{-04}$	$5.09 \cdot 10^{-03}$
Fractal	Min	$1.61 \cdot 10^{-04}$	$2.18 \cdot 10^{-04}$	$8.61 \cdot 10^{-05}$	$9.68 \cdot 10^{-04}$
	Max	$1.94 \cdot 10^{-04}$	$2.65 \cdot 10^{-04}$	$3.97 \cdot 10^{-04}$	$3.44 \cdot 10^{-03}$

The empirical coefficient of permeability was calculated using the Pavchich formula (Goldin and Rasskazov (1992)), expressed as follows:

$$K = \frac{g}{\nu} 4 \cdot 10^{-3} B^3 \sqrt{U} \frac{\phi^3}{(1-\phi)^2} d_{17}^2$$

where g is the acceleration due to gravity, ν is the kinematic viscosity of water (m^2/s), B is equal to 1 for sand and gravel and 0.35-0.4 for pebbles, and d_{17} represents the grain diameter in mm for which 17% of the sample are fine then. This formula has been found to be satisfactory for a wide range of soils. We present the extreme (Min. and Max.) values for the coefficient of permeability calculated during simulations for various particle locations. Knowing that the permeability is a 3D property, the permeability calculated using a 2D concept is not fully conclusive for all soils selected in this study.

4. Motion and interaction of particles in fluids (DEM)

The movement of granular particles is modeled using the discrete element method (DEM) proposed by Cundall and Strack (1979). The motions of particle i caused by its interactions with neighboring particles is described by the equations:

$$m_i \frac{d\vec{V}_i}{dt} = m_i \vec{g} + \sum_{j=1}^k (\vec{F}_{cn,ij} + \vec{F}_{dn,ij} + \vec{F}_{ct,ij} + \vec{F}_{dt,ij}) + \vec{F}_f \quad (3)$$

$$I_i \frac{d\bar{\omega}_i}{dt} = \sum_{j=1}^k (\bar{T}_{ij} + \bar{M}_{ij}) + \bar{M}_{\beta}$$

where:

m_i, I_i , are the mass (kg) and moment of inertia (kg m^2) of particle i respectively
 \bar{V}_i and $\bar{\omega}_i$ are the translational (m/s) and rotational (s^{-1}) velocities of particle i
 k is the number of neighboring particles.

$\bar{F}_{cn,ij} = -K_n \delta_n^2 \hat{n}$ is the normal force of contact (N)

$\bar{F}_{dn,ij} = -C_n \bar{V}_{n,ij}$ is the normal damping force (N)

$\frac{d\bar{F}_{ct,ij}}{d\delta_t} = -K_t$ is the tangential force of contact (N). The value of this force is

limited by $|F_{ct,ij}| \leq \mu_s F_{cn,ij}$

$\bar{F}_{dt,ij} = -C_t \bar{V}_{t,ij}$ is the tangential damping force (N)

\bar{F}_{β} is the drag force (N)

$\bar{T}_{ij} = R_i (\bar{F}_{ct,ij} + \bar{F}_{dt,ij})$ is the torque moment (N·m)

$\bar{M}_{ij} = -\mu_r |\bar{F}_{cn,ij}| \frac{\bar{\omega}_i}{|\bar{\omega}_i|}$ is the friction torque (N·m)

\bar{M}_{β} is the drag moment (N·m)

$$K_n = \frac{4}{3} E^* \sqrt{R^*}, \quad C_n = 2\sqrt{m^* K_n}, \quad K_t = 2\sqrt{R} \delta_n \left(\frac{G_i}{2-\nu_i} + \frac{G_j}{2-\nu_j} \right), \quad C_t = K_n \sqrt{\frac{K_t}{K_n}}$$

δ_n, δ_t are the normal and tangential contact displacement respectively:

$$\frac{1}{E^*} = \frac{1-\nu_i^2}{E_i} + \frac{1-\nu_j^2}{E_j} \quad \text{and} \quad \frac{1}{R^*} = \frac{1}{|R_i|} + \frac{1}{|R_j|}$$

where E is Young's modulus (Pa), ν is the Poisson ratio, R_i is the particle radius (m), and μ_s, μ_r are the sliding and rolling (m) friction coefficients respectively. The determination of interaction forces has been detailed by Zhou et al. (2002) and Nakashima (2004).

To obtain the proper particle-liquid interaction, we need to integrate the stress tensor over the particle surface. Currently, we use a 2-D model for the water flow and the spherical particles that move and rotate in a 2-D plane. First, we integrate the stress tensor over the particle surface (circle) at the plane of flow.

$$\bar{F}_{\beta} = \oint_A \left(-p + \eta \left[\nabla \bar{v} + (\nabla \bar{v})' \right] \right) \hat{n} dA \quad (4)$$

where A is the particle outline projection (m) and \hat{n} is the normal to the circular particle.

This force acts per unit length around infinite cylinder into flow. The standard curves for a drag coefficient of a cylinder and a sphere (Clift et al. (1978)) are shown

in Figure 4. For comparison, we have also plotted the Stokes curve. For a low Reynolds number, we can see that

$$C_{Ds} \approx 1.5 \cdot C_{Dc}$$

where C_{Ds} and C_{Dc} are the drag coefficients for a sphere and a cylinder respectively.

Therefore, the relationship of the drag force for the cylinder and the sphere under the same flow conditions can be rewritten as:

$$\frac{F_s}{F_c} = \frac{3\pi d}{8}$$

where F_s is the drag force for the sphere (N), F_c is the drag force for the cylinder (N/m), and d is the diameter of the circular particle (m). The numerical results obtained for particles 0.5 and 1 mm in diameter are shown in Figure 4.

The buoyancy force is included in formula 4, and is adjusted for a spherical particle. The no-slip liquid boundary condition on each particle surface was also implemented. We used the condition proposed by Kalthoff et al. (1997). All the liquid grid velocities located "inside" a particle are constrained to equal the particle velocity before the evaluation of the temporal velocity at each time step.

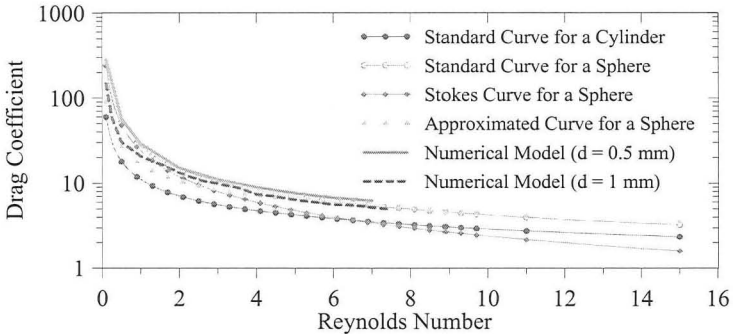


Figure 4. Drag coefficient as a function of the Reynolds number.

5. Results validation

To validate the numerical results obtained, experimental data obtained by Zhang et al. (1999) were selected. These data concern the settling of spherical particles and the dynamic behavior of their collision in a viscous fluid. Several experiments were carried out with different particle densities and dynamic viscosities. Lubrication theory predicts that contact is impossible at low Reynolds numbers. However, due to the existence of microscopic surface roughness on real particles, direct particle-particle contact is possible. Several studies on the rebounding of colliding particles have been published in recent years. We use an algorithm in which the collision process starts when the separation between particles is less than one MAC cell. The change in velocity with distance for spherical particles before and after colliding with a fixed particle in aqueous glycerine is shown in Figure 5(a) and

5(b) respectively. Figure 5(b) concerns only the example with a particle density of 2180 kg/m^3 and fluid with a dynamic viscosity of $0.053 \text{ Pa}\cdot\text{s}$. Our results are depicted in Figure 6. The visualization allows users to explore relationships in the data, and to better present the results to scientists and engineers. In this way, particle-tracking models can be better integrated into decision support systems.

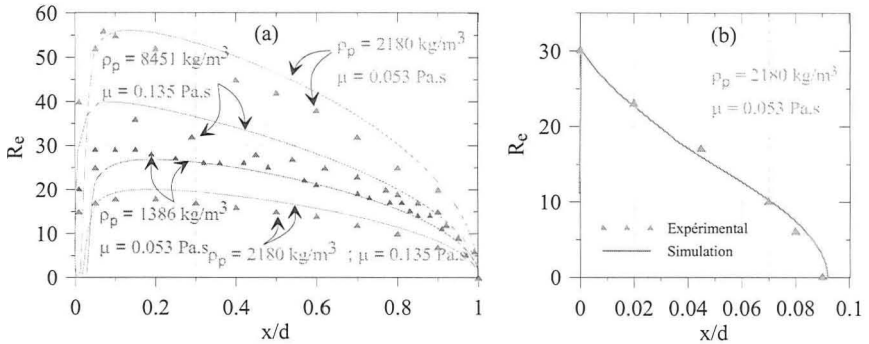


Figure 5. Comparison of simulated and experimental data for colliding particles in viscous fluid

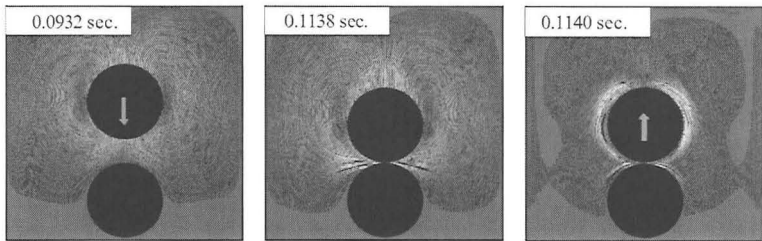


Figure 6. Visualization of the velocity field induced by the normal collision of a settling particle with fixed particle

Figure 7(a) compares the numerical data and experimental data for the settling of glass beads and also after they collide with a wall in water. A schematic representation of the test setup is shown in Figure 7(b). Computational visualization of the flow streamlines during settling of the glass beads and as they approach the wall is shown in Figure 8.

Another validation example concerns the trajectories of a particle for the oblique collision of two glass beads. Comparison of the experimental and simulation results is presented in Figure 9(a). Visualization of the flow streamlines before and after collision is presented in Figure 9(b). We have also compared the results obtained by our model with other experimental results (Zhao and Davis (2002), Bouard and Coutanceau (1986)), and found that they agree very well.

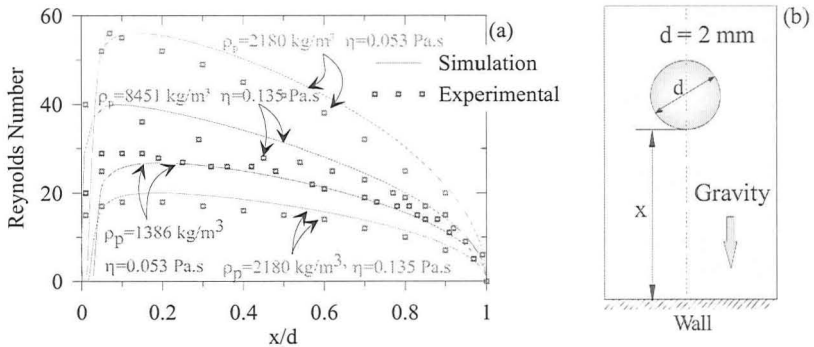


Figure 7. (a) Comparison of the simulation and experimental data for the collision of a glass bead with a wall in water, and (b) Experimental setup

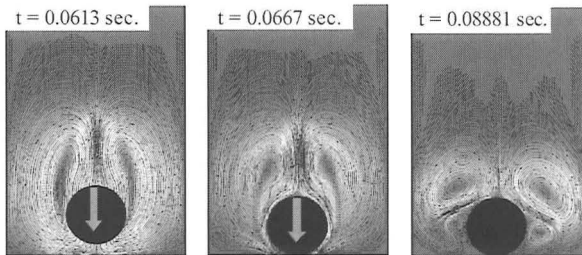


Figure 8. Visualization of the flow streamlines induced by collision of the particle with the wall

6. Simulation of erosion at the interface of two soils

In simulating a possible erosion scenario in 2-D between two layers of different soils generated virtually, special conditions were imposed: the top layer of soil particles (coarse gravel) was kept fixed at all times, while the bottom layer of soil particles (silt) was fixed until a steady-state flow was achieved. This allowed the silt particles to migrate under the effect of hydrodynamic forces. This approach was adopted to allow water to pass between the particles. These conditions would not be needed for a 3-D model.

Our objective with this example is to illustrate the potential of our model to examine the stability of a given base soil-filter system with a flow parallel to the contact interface. We simulate only a very small arrangement of soil particles containing 614 moving particles for silt and 14 fixed particles for coarse gravel. The density of the silt particles is 2700 kg/m^3 . The size of the silt particles is $9.77 \cdot 10^{-3} - 0.15 \text{ mm}$ and that of the gravel particles is $1.11 - 0.278 \text{ mm}$. The gradient is constant, and is equal to 0.063. The stages of particle movement at different times are presented in Figure 10. The velocity of the water in gravel is greater than it is in silt, because the pore channels are larger in the gravel. As the fine particles begin to leave

the soil, the pores become larger and the channels straighter. Increasing flow velocity subsequently causes major silt particle migration.

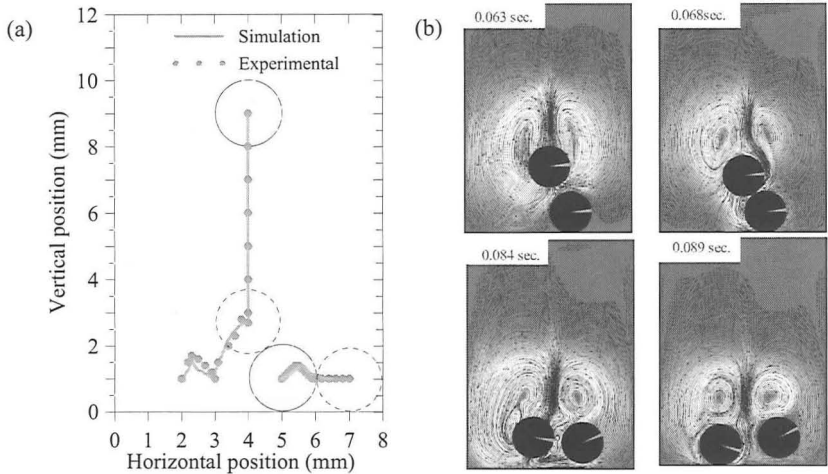


Figure 9. (a) Experimental and simulation results of the trajectories of two particles colliding, and (b) Visualization of results

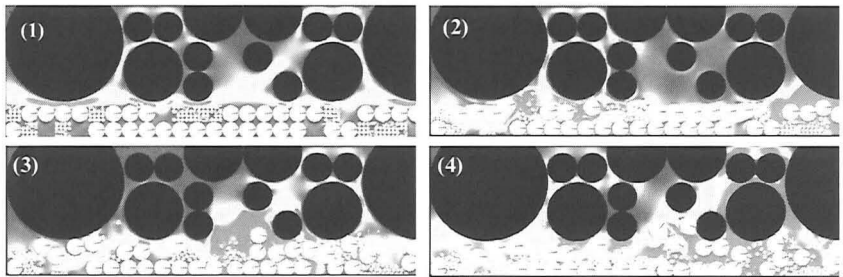


Figure 10. Visualization of the erosion process: (1) steady-state flow with fixed particles ($t = 0.00$ sec.), (2) Motion of the finest particles ($t = 0.013$ sec.), (3) Motion of the largest particles ($t = 0.022$ sec.), and (4) Erosion ($t = 0.030$ sec.)

7. Conclusion

Our preliminary results in this paper indicate that the proposed 2-D model can virtually generate different kinds of soils successfully using only grain size distribution curves, and can estimate soil characteristics, such as the coefficient of permeability. The simulation results of the dynamic behavior of particles in motion in a fluid imply that the model can precisely describe the hydrodynamic behavior of particles in motion, predicting the motion of the particles before collision, the collision between particles, the rebounding of particles following contact, and the motion of particles after contact. Several other simulations show that the model

results agree very well with those obtained from experiments. An example of the visualization of erosion at the contact interface between two different soils under horizontal flow shows the capability of the model. It can determine the transport and deposition rates of particles, where the porous media were subjected to hydrodynamic flow, and it can simulate the microscopic features of the process of internal erosion. Currently, the model has some limitations, such as the round shape of the particles and the 2-D water flow. Based on the verification work presented in this paper, the focus will now move to the development of 3-D model, which can accommodate the real shape of natural particles and include the compaction effects and cohesive forces.

REFERENCES

- Bouard, R. and Coutanceau, M. (1986). "Étude théorique et expérimentale de l'écoulement engendré par un cylindre en translation uniforme dans un fluide visqueux en régime de Stokes." *Journal of Applied Mathematics and Physics (ZAMP)*, Vol. 37 (5): 673-684.
- Clift, R., Grace, J. R., and Weber, M. E. (1978). *Bubbles, Drops and Particles*, Academic Press, New York, 380 p.
- Cundall, P. and Strack, O. (1979). "A Discrete numerical model for granular assemblies." *Geotechnique*, Vol. 29(1): 47-65.
- Goldin, A. L. and Rasskazov, L. N. (1992). Earth Dam Design, *Geotechnika 2*. Balkema, Rotterdam, 328 p.
- Harlow, F. H. and Welch J. E. (1965). "Numerical calculation of time-dependent viscous incompressible flow of fluid with a free surface," *The Physics of Fluids*, Vol. 8: 2182-2189.
- Kalthoff, W., Schawarzer, S., and Herrmann, H. J. (1997). "Algorithm for the simulation of particle suspensions with inertia effects," *Physical Review*, Vol. 56(2): 2234-2242.
- Lehmann, P., Stähli, M., Papritz, A., Gygi, A., and Flühler, H. (2003). "A Fractal Approach to Model Soil Structure and to calculate thermal conductivity of soils," *Transport in porous media*, Vol. 52: 313-332.
- Nakashima, H. (2004). "Discrete Element Method (DEM) and its possible application." *SICE Annual Conference in Sapporo*, Vol. 2: 1104-1107.
- Perrier, E., Bird, N., and Rieu, M. (1999). "Generalizing the fractal model of soil structure: the pore-solid fractal approach." *Geoderma*, Vol. 88: 137-164.
- Scheidegger, A. E. (1963). "The Physics of Flow Through Porous Media." University of Toronto Press, Toronto.
- Vukovic, M. and Soro, A. (1992). "Determination of Hydraulic Conductivity of Porous Media from Grain-Size Composition." *Water Resources Publications*, Littleton, Colorado, CO, 83 p.
- Zhang, J., Fan, L.-S., Zhu, C., Pfeffer, R., and Qi, D. (1999). "Dynamic behavior of collision of elastic spheres in viscous fluids." *Powder Technology*, Vol. 106: 98-109.
- Zhao, Y. and Davis R. H. (2002) "Interaction of two touching spheres in a viscous fluid." *Chemical Engineering Science*, Vol. 57: 1997-2006.
- Zhou, Y. C., Xu, B. H., Yu, A. B., and Zulli, P. (2002). "An experimental and numerical study of the angle of repose of coarse spheres." *Powder Technology*, Vol. 125: 45-54.

Reexamination of Creep Theory in the Foundation of Weirs by Model Experiments and Elasto-Plastic FEM

K. Okajima¹, N. Magara¹ and T. Iida¹

¹Laboratory of Water Environmental Engineering, Department of Biological and Environmental Engineering, Graduate School of Agricultural and Life Sciences, The University of Tokyo, Zip code 113-8657, Tokyo, Bunkyo-ku Yayoi 1-1-1; PH(+81)3-5841-5349; email: aokajim@mail.ecc.u-tokyo.ac.jp

ABSTRACT

Creep flow theories that are Bligh's and Lane's equation have been used as the safety criteria against piping under foundation of weirs. These methods were reexamined by model experiments and finite element analyses in this study. These model experiments were carried out in six patterns and had same creep length by changing the installation position and length of cut-off wall. These critical water heads of model experiments were different from each pattern. It was clear that creep flow theories were not able to predict these differences. Our FEM predicted these critical water heads of model experiments. Maximum shear strain contour line by our finite element analysis indicated that shear strain concentrated in similar soil mass as Terzaghi assumed in the seepage failure equation. It was suggested that Terzaghi's method was more effective than the creep theory to calculate the critical water head if the soil mass was defined properly.

INTRODUCTION

Creep flow theories are applied to the design criteria against piping of foundation of a weir. Bligh's creep flow theory was developed as the empirical equation for the design of floating type weirs in permeable layer through many experiences in 1910 (Bligh). After suggestion of this theory it was indicated that vertical sections of the creep length contribute more to reduce the danger of piping than horizontal sections of the length. In the response to this, Lane (1935) suggested the weighted creep flow theory. These creep flow theories were based on the assumption that the cause of piping was erosion along the contact surface between soils and weir.

The purpose of this study is the reexamination of these practical safety criteria

against seepage failure. We conducted a series of model experiments, and then evaluated these practical safety criteria and the validity of the elasto-plastic FEM by applying to the experiments.

CREEP FLOW THEORIES

To prevent piping at the down-stream side of a weir, practical manuals indicate that a safe creep length have to be ensured under the surface of the weir and along the side of the weir. The creep length to be ensured must be larger than the values calculated by two methods.

The first method is Bligh's method.

$$L_B \geq C_B \Delta H \quad (1)$$

Where L_B is the creep length that is measured along the bottom face of the weir, C_B is Bligh's creep ratio which varies depending on the type of the foundation soil, and ΔH is the water head. For example the fine sand C_B is 15. The critical head is ΔH_{CB} when $L_B = C_B \Delta H_{CB}$.

The second method is Lane's method.

$$L_L \geq C_L \Delta H \quad (2)$$

Where L_L is the weighted creep length.

$$L_L = \sum l_v + k_v / k_h \sum l_h \quad (3)$$

Where, l_v is the creep length of vertical direction (inclination angle of more than 45 degrees), l_h is the creep length of horizontal direction (inclination angle of lower than 45 degrees). k_v is the vertical coefficient of permeability and k_h is the horizontal coefficient of permeability. However, k_v / k_h has been used 1/3 customarily. C_L is Lane's creep ratio which varies depending on the type of the foundation soils. For example the fine sand C_L is 7.0. ΔH is the water head. The critical head is ΔH_{CL} , when $L_L = C_L \Delta H_{CL}$.

MODEL EXPERIMENTS AND REEXAMINATION OF CREEP FLOW THEORIES

Layout of Model Experiments

The experimental apparatus was consisted of a glass-walled sand box. The size was 1000mm long, 500mm high and 200mm wide. The permeable layers in these model experiments were made by using clean sand. The sand was the Toyoura sand with a specific gravity of 2.64, a mean diameter (D_{50}) of 0.16 mm and a uniformity coefficient of 1.46. The weir was made of rigid acrylic plates. The weir was fixed to sand box and was sealed by silicon rubber and silicon adhesion bond to prevent water and sand from spilling out. The sandpaper was pasted on the bottom and side of the weir to prevent roofing. The cut-off wall was made of aluminum plate. The sand layers were prepared by pouring dry sand using hopper into stored water and deleting air during the soil particle falling. The high density of the sand layers was obtained: the relative density was about 85%.

After setting up the water levels of both upstream and downstream side equal, the downstream water level was lowered incrementally (5mm after an hour). The deformation of the sand layer was measured. When piping or boiling occurred, the water head was defined to attain the critical water head.

The data of a series of model experiments are indicated in Figure2. All patterns had same creep length in which Bligh's creep length is 180mm and Lane's creep length is 123mm. These data were obtained by conducting 2 or 3 times in each experiment. These experiments are divided into 3 groups (Figure1). The first group was named "Depth group" to change penetration depth of the weir: Weir1, Weir2 and Weir3. From these experiments we can evaluate the influence of the depth of the weir for piping. The second group was named "Position group" to change the position of a cut-off wall: Weir4, Wei3 and Weir5. From these experiments we can evaluate the influence of the position of the cut-off wall for piping. The third group was named "Two cut-off group" to change the position and length of two cut-off walls: Weir6 and Weir7. From these experiments we can evaluate the influence of the position of the cut-off wall for piping.

Results of Model Experiments

Table1 shows results of model experiments that are relative density (%), critical water head, the kind of seepage failure (Piping or Boiling) and average of critical water head. Piping was observed in some patterns of model experiments. The

heaving was observed because sand ground in down-stream side deformed. Relative densities were about 85% from 81.2% to 88.9%. Critical water heads in each pattern were similar water heads. In these model experiments the reproducibility was observed.

These model experiments had same creep length. Bligh's and Lane's creep flow theories predict a critical water head with patterns. However, each critical water head was different from the other pattern. The result indicated that creep flow theories were not able to predict the critical water head. Discussions of each groups described later.

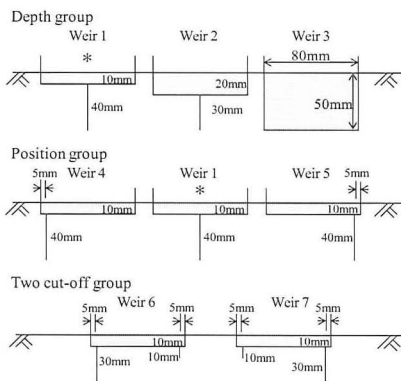


Figure 1 Patterns of model experiments

Table 1 Results of model experiments

Pattern	Relative Density %	Critical water head mm	Piping / Boiling	Average of critical water head mm
Weir1	82	80	Piping	87
	86.3	90	Piping	
	83.6	90	Piping	
Weir2	84.7	140	Piping	137
	86.1	145	Boiling	
	84.5	125	Piping	
Weir3	88.9	250	Boiling	258
	85.1	251	Boiling	
	81.4	271	Boiling	
Weir4	87.4	70	Piping	73
	81.2	75	Piping	
	81.5	75	Piping	
Weir5	82.6	155	Boiling	170
	83.1	175	Boiling	
	87.4	180	Boiling	
Weir6	86.6	130	Boiling	133
	84.5	135	Boiling	
	82.6	135	Boiling	
Weir7	83.6	145	Boiling	155
	82.3	165	Boiling	

SEEPAGE FAILURE ANALYSES BY ELASTO-PLASTIC FEM

In this study the finite element analysis consisted of two steps. The first step is the seepage flow analysis by FEM. The second is the seepage failure analysis by the elasto-plastic FEM to input effective stress regarding the seepage force as the external force.

Constitutive model of the elasto-plastic model

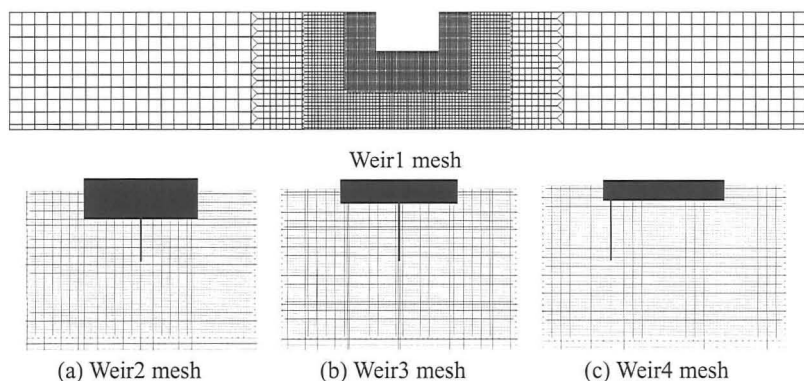
The finite element analysis employs the elasto-plastic constitutive equations with a non-associated flow rule and strain hardening-softening. The constitutive equations based on the yield function of Mohr-Coulomb and the plastic potential function of Drucker-Prager. The finite element is 4-noded iso-parametric element

with one point integration. The explicit dynamic relaxation method combined with the generalized return-mapping algorithm is applied. The elasto-plastic constitutive relations including the effect of the shear band are employed.

A simplified and generalized version of mesh size-dependent softening modulus method (Tanaka and Kawamoto, 1989) is used in this study. A material model for a real granular material (i.e., Toyoura sand) with a high angle of internal friction is used with the features of nonlinear pre-peak, pressure-sensitivity of the deformation and strength characteristics of sand, non-associated flow characteristics, post-peak strain softening, and strain-localization into a shear band with a specific width (Tatsuoka et al., 1991; Siddiquee, 1999). The material model will be briefly described in this section.

Input Parameter and FEM mesh

In the elasto-plastic finite element analysis, the material constants of Toyoura sand are as follow: relative density = 88%, residual friction angle (ϕ_r)= 33 degree. The calibration of the other elasto-plastic parameter of air-dried Toyoura sand in the elasto-plastic constitutive model was performed using the plane strain compression tests by Tatsuoka et al (1986). The analysis was performed using a series of finite element mesh of each model experiment, as shown in Figure2. Elements bordering on the weir were boundary elements and the friction was set to be equal to the friction between sand and weir in these elements.



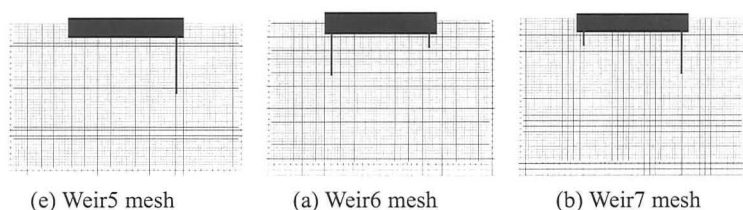


Figure 2 FEM mesh

RESULT AND DISCUSSION

Critical water head

Result of model experiments and FEM in each group are discussed about the effectiveness of FEM and the tendency of seepage failure of foundation of the weir. Figure3 indicates the critical water head of Position group. The critical water head gradually increases with the moving to the downstream end of the weir in Position group which has same creep length. Results of FEM predicted each critical water head well. Figure4 indicates the critical water head of Depth group. The critical water head gradually increases with the increasing the penetration depth of the weir in Depth group which has same creep length. Results of FEM predicted each critical water head well. Figure5 indicates the critical water head of Two cut-off group. The critical water head varies with the number and length of cut-off walls though these critical water head was near without the point of longer cut-off wall. Results of FEM predicted each critical water head well. Results of FEM which penetration depth of weir was 10mm and the cut-off wall was set at upstream side or middle of the length of weir were computed higher than results of model experiments (Weir1 and Weir4). The reason is considered that the continuum model might not hold true when number of particle of sand (the average particle side is 0.16mm) was about 60 at the downstream edge of the weir. Result of FEM which penetration depth of weir was 50mm was computed lower than results of model experiment (Weir3). The reason was considered that the friction of the side glass wall influenced the water head of boiling because it was observed that larger sand mass moved during the boiling in the model experiments of Weir3. These discussions indicated that our FEM was effective analysis to compute the critical water head.

Maximum shear strain

Our elasto- plastic FEM has the frictional hardening-softening functions.

When the maximum shear strain reaches 0.1, the frictional function changes from hardening regime to softening regime. At that time the shear band develops in these elements. Figure6 indicates that the observed shear band in model experiment at water head 180mm and computed maximum shear strain distribution by FEM at water head 170mm. The observed shear band is showed by broken line in the picture. When the shear band was compared with concentration area of the maximum shear strain, it is clear that our FEM is able to predict the position and the tilt of the shear band well. This result indicated that our FEM was able to predict the deformation by seepage failure. So we discussed the mechanism of seepage failure with these maximum shear strain distribution by our FEM.

Figure7 indicates maximum shear strain distributions at the critical water head of Weir1, Weir2, Weir3 and Weir4. It is indicated that the mechanism to change the critical water head of Depth group is expanding of concentration area of maximum shear strain from Figure7 (a), (b) and (d). It is indicated that the mechanism to change the critical water head of Position group is expanding of concentration area of maximum shear strain from Figure6 and Figure7 (d) when the cut-off wall approaches the downstream edge of weir. However the concentration areas of Figure7(c) and (d) is very similar without the position of the cut-off wall. The difference of the critical water head between Weir4 and Weir1 causes the seepage force by seepage flow.

These mechanisms of seepage failure indicated that Terzaghi's method in the cut-off pile was possible to predict the critical water head in the weir.

Application of Terzaghi's method

Terzaghi's method is the most famous method of a critical hydraulic gradient. Originally, Terzaghi's method was developed to be applied to a safety criterion for sheet pile piping. This method was formulated based on experimental model tests and its effectiveness was confirmed by many sheet pile model tests. In Terzaghi's method, a piping occurs when the submerged weight of the soil prism on the down-stream side of the sheet pile equals the heaving force by excess hydrostatic pressure. In the formulation Terzaghi defined that the size of the prism was $D \times D/2$ in the two dimensional condition when the penetration depth is D .

In this study we decided that the penetration depth D is the depth of downstream edge of the weir. Figure8 indicates the result of application of Terzaghi's method to the weir. Terzaghi's method was very good prediction of the critical water head. It was suggested that Terzaghi's method was more effective than the creep

theory to calculate the critical water head in the seepage failure of the weir.

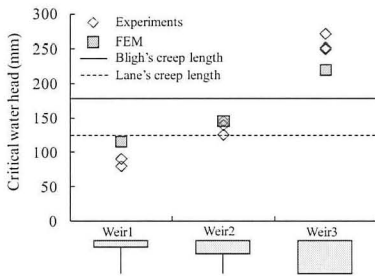


Figure 3 Critical water head of Position group

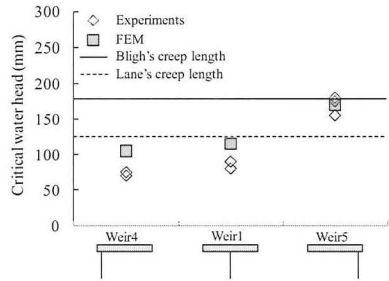


Figure 4 Critical water head of Depth group

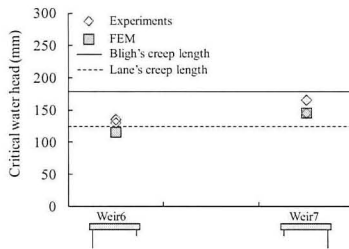


Figure 5 Critical water head of Two cut-off group

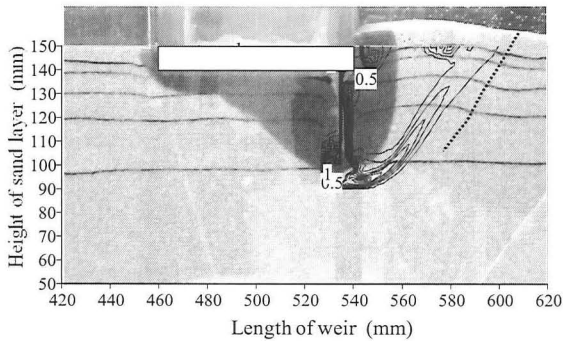
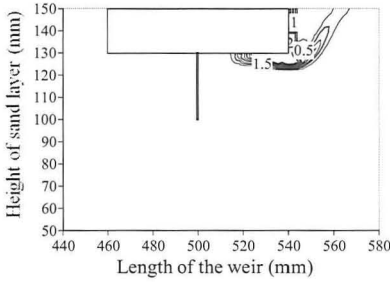
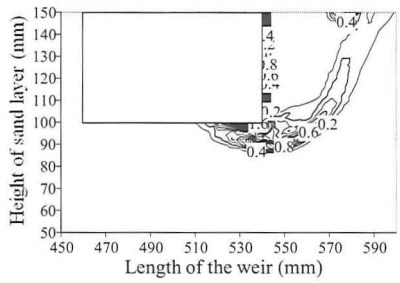


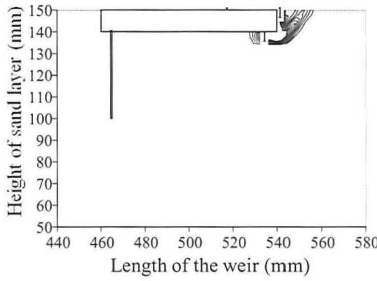
Figure 6 Shear band in model experiment at water head 180mm and maximum shear strain distribution at water head 170mm



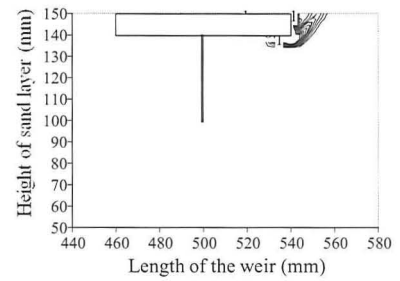
(a) Maximum shear strain distribution at water head 140mm (Weir2)



(b) Maximum shear strain distribution at water head 230mm (Weir3)

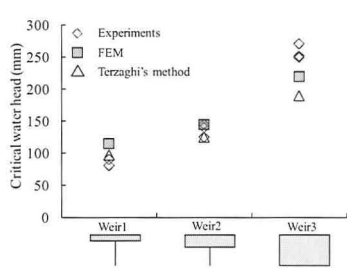
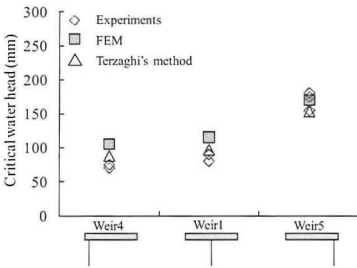


(c) Maximum shear strain distribution at water head 105mm (Weir4)



(d) Maximum shear strain distribution at water head 115mm (Weir1)

Figure 7 Maximum shear strain distribution of elasto-plastic FEM



(a) Critical water head of Position group

(b) Critical water head of Depth group

Figure 8 Critical water head in applying Terzaghi's method

CONCLUSION

Creep flow theories were reexamined by model six patterns experiments and finite element analyses that had same creep length by changing the installation position and length of cut-off wall in this study. These critical water heads of model experiments were different from each pattern. It was clear that creep flow theories were not able to predict the critical water head. Our FEM predicted these critical water heads of model experiments. Maximum shear strain contour line by our finite element analysis indicated that shear strain concentrated in similar soil mass as Terzaghi assumed in the seepage failure equation. It was suggested that Terzaghi's method was more effective than the creep theory to calculate the critical water head if the soil mass was defined properly.

REFERENCES

- Bligh, W. G. (1910) "The practical design of irrigation works", London Constable, 162-205
- Lane, E.W. (1935) "Security from Under seepage Masonry Dams on Earth Foundations", *Trans. ASCE*, 100, 1234-1351,
- Tanaka, T and Verruijt, A (1999) "Seepage failure of sand behind sheet piles - The mechanism and practical approach to analyze-", *Soils and Foundations*, 39(3), 27-35
- Tanaka, T. and Kawamoto, O. (1988) "Three dimensional finite element collapse analysis for foundations and slopes using dynamic relaxation", *Proc. of Numer. Meth. in Geomech.*, 1213-1218,
- Tatsuoka, F., Siddiquee, M. S. A, Park, C. S., Sakamoto, M. and Abe, F. (1993) "Modeling Stress-Strain Relations of Sand", *Soils and Foundations*, 33(2), 60-81
- Terzaghi, K. and Peck, R. B. (1948) "Soil Mechanics IN Engineering Practice", John Wiley and Sons, 218-233

Application of the Multi-Dimensional Surface Water Modeling System at Bridge 339, Copper River Highway, Alaska

T. P. Brabets¹, M. ASCE and J. S. Conaway¹

¹U.S. Geological Survey, Alaska Science Center, 4210 University Drive, Anchorage, Alaska, 99508; PH (907) 786-7105; email: tbrabets@usgs.gov; jconaway@usgs.gov

ABSTRACT

Due to a major channel change in 2001, Bridge 339 at Kilometer 58 of the Copper River Highway has undergone excessive scour, resulting in damage to its abutments and approaches. Maintenance at Bridge 339 has been costly and will continue to be so if no action is taken. The USGS Multi-Dimensional Surface Water Modeling System (MD_SWMS), in its 2-dimensional mode, was used to assess three possible solutions: (1) constructing a guide bank to redirect flow, (2) dredging approximately 305 meters of channel upstream of the bridge to align flow perpendicular to the bridge, and (3) extending the bridge. Under existing conditions and at the highest measured discharge and stage of 920 m³/s and 15.58 m, respectively, the velocities and shear stresses simulated by MD_SWMS indicate scour and erosion will continue. Construction of a 76-meter-long guide bank would not improve conditions because it is not long enough. Dredging a channel upstream of Bridge 339 would help align the flow perpendicular to Bridge 339, but because of the mobility of the channel bed, the dredged channel would likely fill in during high flows. Extending Bridge 339 would accommodate higher discharges and re-align flow to the bridge.

INTRODUCTION

The lower Copper River/Copper River Delta is a complex and dynamic system. Near its mouth, the Copper River drains approximately 62,000 km², making it the third largest basin in the State of Alaska. During the winter months (November through April), the river is ice covered and flow averages 330 m³/s. During the open water months, May through October, snowmelt and glacier melt contribute significant flow to the Copper River and average flow increases by an order of magnitude—to 3,200 m³/s.

The Copper River Highway begins at Cordova and heads about 77 km northeast to the Million Dollar Bridge. Eleven bridges are located along the highway as it extends across the delta (fig. 1). Channels in the large delta are constantly scoured and filled, and flow shifts from one channel to another. As a result, several bridges have been damaged by excessive scour. For example, Bridge 342 has undergone major reconstruction (adding 146 m to the original bridge and constructing spur dikes) due to a combination of channel migration, changes in flow regime, and severe scour.

The purpose of this report is to (1) provide a brief history and overview of the recent channel changes at Bridge 339 that have resulted in higher flows at the bridge, and (2) analyze the hydraulic conditions at the bridge at a discharge of $920 \text{ m}^3/\text{s}$ and how those conditions would be affected if different improvements were put in place. These improvements included a guide bank, re-channelization, and lengthening the bridge.

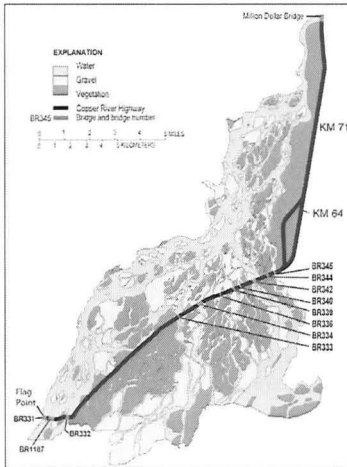


Figure 1. Locations of bridges along the Copper River Highway, Alaska.

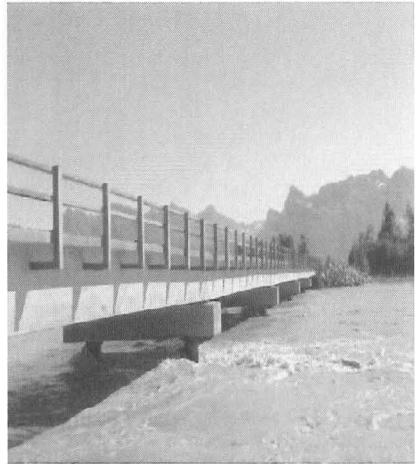


Figure 2. Bridge 339, Copper River Highway, August 6, 2004 (Discharge- $770 \text{ m}^3/\text{s}$)

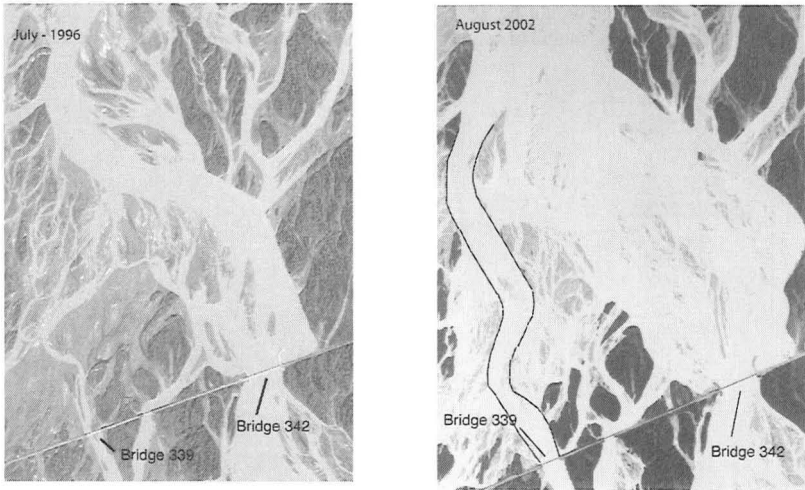
BRIDGE 339 – PAST AND PRESENT CONDITIONS

The bridges from Flag Point to the Million Dollar Bridge (fig. 1) were damaged in the 1964 earthquake. Beginning in 1970, as part of a major reconstruction effort, all the bridges were rebuilt. Bridge 339 was designed for a flow of $500 \text{ m}^3/\text{s}$ and rebuilt during 1976–78. When completed, the bridge was 122 m long and supported by four sets of concrete-filled steel piers spaced 24 m apart (fig. 2).

Flow and channel characteristics of the lower Copper River from 1950 to 1995 were documented in an earlier USGS study (Brabets, 1997). The study found that of the total flow of the Copper River that passed through the Million Dollar Bridge, approximately 50 percent passed through the bridges at Flag Point (Bridges 331, 1187, and 332) and approximately 40 percent passed through Bridge 342 (fig. 1). The remaining flow passed through the other bridges and the percentage of flow that passed through Bridge 339 ranged from less than 1 percent to 5 percent of the total flow – $28 \text{ m}^3/\text{s}$ to $415 \text{ m}^3/\text{s}$ – well below the design discharge for the bridge.

Based on aerial photography taken in 1996 and records of the Alaska Department of Transportation and Public Facilities (AKDOT&PF) Cordova maintenance office, the flow conditions at Bridge 339 remained the same until 2001. In 2001, most likely due either to high flow in the Copper River or to the effects of ice jams, a major channel

change occurred at the bridge. A comparison of aerial photography flown in 2002 with aerial photography flown in 1996 clearly showed the channel change (figs. 3-4). A fairly large sinusoidal (S-shape) channel formed upstream of Bridge 339.



Figures 3-4. Aerial photographs of the lower Copper River near Bridge 339 taken in July 1996 and August 2002.

From 2002 to 2009, the main channel to Bridge 339 has constantly changed. LIDAR (Light Detection and Ranging) imagery obtained in 2005 and aerial photography flown in 2006 and 2007 (figs. 5-6) showed the channel migrating toward the west and impacting the approach to the bridge. The channel then reversed direction and headed eastward, parallel to the approach, and then flowed under the bridge. Because of the changing direction of the channel, the angle of attack, and the foundation material beneath the approach to Bridge 339, large quantities of riprap were needed to stabilize the approach; in most instances, this provided only temporary bank stabilization during the summer runoff months. Since 2004, approximately 7,650 m³ of large riprap have been placed along the approach by AKDOT&PF personnel.

As a result of this channel change (and additional damage that was done to the Copper River Highway from Kilometer 66 to 71 in 2001), the USGS, in cooperation with AKDOT&PF, began another study of the lower Copper River. In 2004, the first discharge measurements since 1995 were made at Bridge 339. These measurements confirmed the major channel change because the discharges measured (740 m³/s, 570 m³/s, and 350 m³/s) represented about 20 percent of the total flow of the Copper River. In 2005, sonars (depth sensors) were installed on piers to measure scour. Scour depths as great as 9 m have been recorded. From 2004 to 2008, discharge measurements at Bridge 339 have documented flows as high as 920 m³/s, far exceeding the bridge's design discharge of 500 m³/s. Depending on the alignment of the approach channel relative to the bridge opening, scour has varied among the piers.



Figures 5-6 Aerial photographs of the lower Copper River near bridge 339 taken in October 2006 and August 2007.

In October 2006, the Copper River Basin experienced flooding as a result of a 'pineapple express,' a low-pressure system that moved inward from the Gulf of Alaska. The resulting flood peak of $12,400 \text{ m}^3/\text{s}$ at the Million Dollar Bridge was estimated to have only a 1 to 1.5 percent chance of occurrence. The peak stage at Bridge 339 was 16.29 m, and the estimated peak discharge was $1,560 \text{ m}^3/\text{s}$. Although there was no structural damage to Bridge 339, the flood damaged the western approach to the bridge, almost breaching the roadway, and the heavy riprap that had been placed along the approach was washed away. Based on the inspection of the aerial photography and discharge measurements taken after the October 2006 flood, it does not appear that any long-lasting channel changes resulted from the flood.

River discharges well in excess of the design discharge at Bridge 339 have and will continue to require maintenance by AKDOT&PF at the west approach to the bridge. Additionally, the piers at Bridge 339 are subject to excessive scour and the structure itself could be at risk. The channel will continue to undercut the west approach, which consists of fine-grained material, and as a result of the undercutting, riprap will continue to be washed away and will need to be replaced. As the channel erodes in the vicinity of Bridge 339, there will be a tendency to flow into another channel towards Bridge 336 (fig. 1). Increased discharge in this channel would impact the highway in several points that have no riprap protection before passing through Bridge 336, which has a design discharge of only $240 \text{ m}^3/\text{s}$. The material of the roadbed between Bridges 339 and 336 is easily erodible, and the road grade is lower than at Bridge 339. Thus, in addition to continued problems at Bridge 339, problems could also arise at Bridge 336 or along the highway between the two bridges if the approach channel to bridge 339 migrates to the west.

Also of concern to AKDOT&PF is the migration of the approach channel to Bridge 339 during August – September 2008 (figs. 7-8). The main channel now directly impacts the right downstream abutment, requiring placement of additional heavy riprap for reinforcement. If movement of the channel continues, flow will be directed towards the east approach (left bank) to the bridge, most likely creating the same conditions that occurred on the west approach.



Figures 7-8. Aerial photograph of the Bridge 339 area taken in October 2006 and photograph of Bridge 339 taken on September 29, 2008. Red line indicates the position of the left bank in August-September 2008.

POTENTIAL SOLUTIONS TO SCOUR AND EROSION AT THE BRIDGE 339 AREA

Some solutions or betterments that have been considered for Bridge 339 are (1) constructing a 76-m guide bank on the west upstream side of Bridge 339 to direct the water perpendicular to the bridge, (2) re-channelization or dredging of approximately 305 m of channel directly upstream of Bridge 339, and (3) extending the bridge. Each of these betterments would have a different effect on the hydraulic conditions in the Bridge 339 area. The USGS Multi-Dimensional Surface Water Modeling System (MD_SWMS) (McDonald and others, 2005) was used to analyze the hydraulic conditions resulting from the proposed betterments.

MD_SWMS is a generic Graphical User Interface (GUI) developed by the USGS (McDonald and others, 2006) for hydrodynamic models. FaSTMECH, one of the computational models within MD_SWMS (Nelson and McDonald, 1997), includes a 2-dimensional, vertically-averaged model and a sub-model that calculates vertical distribution of the primary velocity and the secondary flow about the vertically averaged flow. This so-called '2.5-dimensional' approach has been shown to adequately simulate

the velocity field and bed shear stress without the complexity of a fully 3-dimensional model (Barton and others, 2005).

Minimum data requirements for the model include channel geometry, streamflow at the upstream boundary, and water-surface elevation at the downstream boundary. The physical assumptions of the model are that flow is steady, incompressible, and hydrostatic (vertical accelerations are neglected), and that turbulence is adequately treated by relating Reynolds stresses to shear using an isotropic eddy viscosity (Nelson and others, 2003).

MD_SWMS was used to simulate the following scenarios at Bridge 339: (1) channel conditions in 2006 with no betterments for model calibration, (2) construction of a 76-m long guide bank at the upstream west abutment of the bridge, (3) re-channelization or dredging of the existing channel upstream of the bridge, and (4) a 73 m extension of Bridge 339. For each scenario, a discharge of 920 m³/s was assumed/simulated, the highest flow that has been measured at the bridge. Water-surface elevation at the bridge (15.61 m) was known at this discharge. The upstream and downstream water-surface elevations were determined on the basis of the water-surface slope determined from the LIDAR data, which was obtained at a discharge of 572 m³/s and a water-surface elevation of 15.50 m. A bed material size (D_{50}) of 8 mm (based on data collected by Brabets, 1997) was used as input to MD_SWMS to compute the critical shear stress of the river bed.

To check the accuracy of the calibration, model convergence was evaluated by MD_SWMS by comparing the predicted model discharge to the observed specified discharge for a selected cross section. If the percent deviation from the normalized discharge was within ± 3 percent, the convergence was considered acceptable. Convergence for each of the four scenarios simulated by MD_SWMS was within acceptable limits.

CALIBRATION CONDITIONS

Two potential scenarios were not addressed with MD_SWMS. First, if the main channel that leads to Bridge 342 (upstream of Bridge 339) were to shift and direct more flow to the channel leading to Bridge 339, the flow capacity of Bridge 339 would be exceeded more frequently than at present and excessive scour at the piers or abutments at Bridge 339 could occur. Secondly, the effects of the movement of the approach channel to Bridge 339 that occurred in August – September 2008 were not considered. The main channel now directs flow at the right downstream abutment, requiring the placement of additional heavy riprap to reinforce the abutment. If movement of the channel continues, flow will be directed toward the east approach (left bank) to the bridge, most likely creating the same conditions that occurred on the west approach to the bridge.

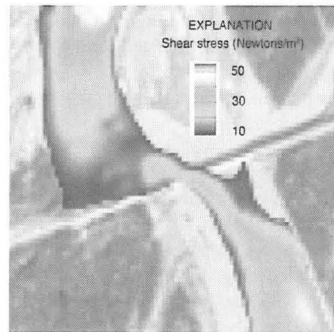
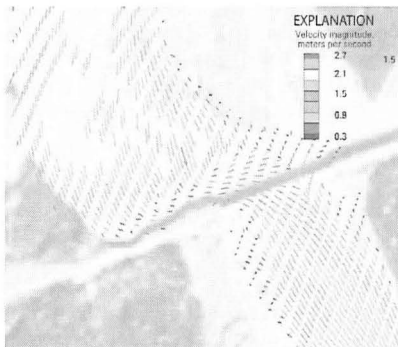
Input conditions for the simulated calibration discharge are presented in table 1. The output from MD_SWMS indicated an averaged predicted water-surface elevation of 15.83 m versus the observed water surface of 15.57 m at the bridge. Predicted velocities ranged from 1.04 to 2.62 m/s along the right bank and the approach to Bridge 339 (fig. 9). Average velocities measured downstream for the calibration discharge ranged from 2.0 m/s to 2.1 m/s. Modeled shear stress values ranged from 5.7 to 50 Newtons/m² (fig. 10). On the basis of previous work by Julien (1998), the critical shear stress for mobility of bed material with a diameter of 8 mm would be 5.7 Newtons/m². Thus, the modeled reach would be considered a mobile bed. Based on field observations, the channel is

constantly changing, thus verifying to a certain extent, the output from MD_SWMS. Although the channel is changing, it was felt the model could be used to simulate the various betterments for qualitative/non-design purposes.

Table 1. Boundary conditions and model parameters used for the simulation of the calibration discharge of 920 m³/s at Bridge 339, Copper River Highway, Alaska.

[m³/s, cubic meter per second; m, meter; m²/s, meter squared per second]

Boundary conditions	
Discharge	920 m ³ /s
Downstream starting water-surface elevation	15.20 m
Channel slope	0.001
Model parameters	
Number of grid cells	31,411
Grid cell spacing in stream-wise and stream-normal directions	5.0 m
Lateral eddy viscosity	0.005 m ² /s
Drag coefficient	0.007

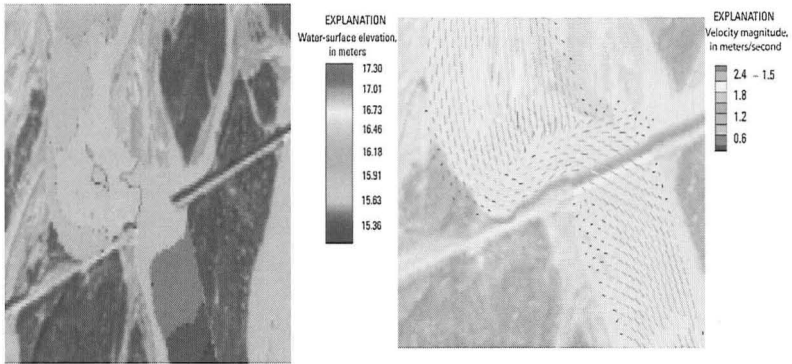


Figures 9-10. Output from MD_SWMS showing velocity vectors and shear stress at the Bridge 339 reach based on a flow of 920 m³/s.

GUIDE BANK

As proposed, the guide bank would be 76 m long and constructed on the west end of the bridge. The guide bank would be perpendicular to the roadway and then angle slightly to the west. The desired effect of the guide bank would be to align the direction of flow perpendicular to Bridge 339. However, the output from MD_SWMS did not indicate this change in flow direction would take place. Velocities, velocity vectors, and bed shear stresses were nearly identical to current conditions, which would indicate that most of the flow still would be directed towards the approach and not towards the bridge (fig. 9). The simulation results indicated that the proposed guide bank would not be long

enough to keep the approach channel from impacting the right bank bridge approach. A possible negative impact of the guide bank, based on the output from MD_SWMS, would be to increase the water-surface elevation along the right bank (fig. 11). Such an increase in water-surface elevation could possibly increase flow towards Bridge 336. However, no attempt was made to determine the amount of flow towards this bridge. A guide bank greater than 76 m would limit flow towards Bridge 336.



Figures 11-12. Output from MD_SWMS showing water-surface elevations at Bridge 339 based on a discharge of $920 \text{ m}^3/\text{s}$ and construction of a 76 m guide bank and velocity vectors based on re-channelization upstream from bridge.

RE-CHANNELIZATION

Another proposed mitigation approach is re-channelization or dredging upstream of the bridge. The proposed dredging would begin at or near the upstream center of Bridge 339, would be 305 m length, 46 m wide, 1.5 to 2.4 m below the 2006 upstream bed elevation of 11 m, and would be aligned perpendicular to the bridge opening. The desired effect of this option is to encourage the approach channel to align itself with the bridge opening. Using these geometric parameters, the channel bathymetry was modified and input to MD_SWMS. This simulation showed the highest velocities through the dredged channel, indicating that most of the flow was through this channel and perpendicular to the bridge (fig. 12). It is important to note, however, that on the basis of calculated shear stresses, the entire bed is mobile. Thus, the dredged channel could fill in when the bed is mobilized during high flow and the original channel would be re-occupied. Also, the dredged channel would be the only one occupied at low flow, when deposition occurs.

BRIDGE EXTENSION

The third betterment analyzed was an extension of Bridge 339. Currently, it would appear that any extension of Bridge 339 should be to the west, but a thorough analysis of channel migration should be done before a final decision is made. Because the main channel is currently on the right bank and a bridge extension would consist of 24-m

sections, for this scenario, a 73 m extension of Bridge 339 to the west was used for modeling purposes.

If Bridge 339 were extended 73 m to the west, simulation results showed that water velocity and the corresponding velocity vectors were lower than the calibration conditions and were more uniform across the channel (fig. 13). Thus, flow would be more nearly centered through the bridge. On the basis of calculated shear-stress values, the channel would still be mobile, but the potential for scour would be reduced due to the lower shear-stress values. Based upon surveyed cross sections from 2005–08, the flow tends to occupy discrete portions of the channel rather than its entire width. If this trend continues, an increase in the bridge opening would do little to mitigate scour.

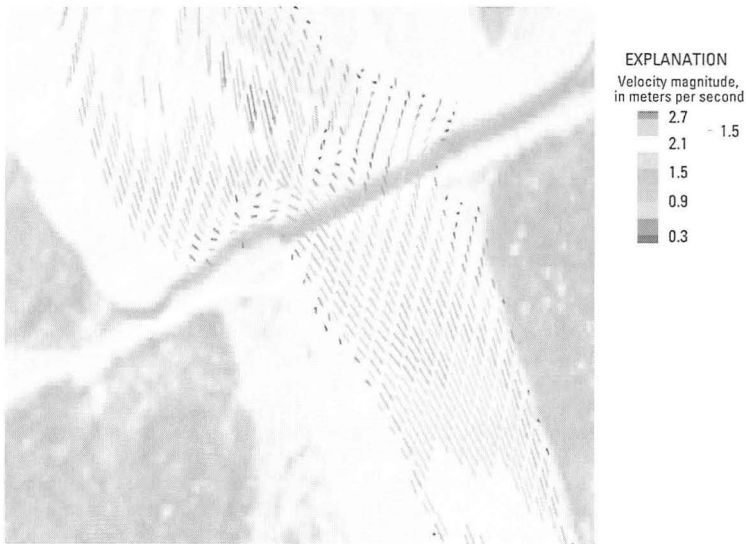


Figure 13. Output from MD_SWMS showing velocity vectors at Bridge 339 based on a flow of $920 \text{ m}^3/\text{s}$ and extending the bridge 73 m to the west.

SUMMARY

Bridge 339, located at Kilometer 58 of the Copper River Highway, Alaska, has undergone significant scour at its piers, abutments, and approach due to a major channel shift of the Copper River in 2001 that resulted in flows higher than the design discharge for the bridge. Under current hydraulic conditions, considerable maintenance will be required to protect the bridge and approach. To insure the integrity of the bridge and reduce maintenance costs, three betterments have been proposed for Bridge 339. The hydraulic conditions associated with these betterments were analyzed using the USGS Multi-Dimensional Surface Water Modeling System (MD_SWMS).

A proposed 76-m long guide bank (betterment 1) would not be long enough to affect hydraulic conditions at the bridge. A possible negative impact of the guide bank

would be to increase the water-surface elevation along the right bank, resulting in higher flow towards another bridge. If the channel upstream of Bridge 339 were dredged (betterment 2), simulation results indicate that most of the flow would pass through the new channel and perpendicular to the bridge. Because the entire bed is mobile, however, the dredged channel could fill back during periods of high flow and the original channel would be re-occupied. If Bridge 339 were extended 73 m to the west (betterment 3), the simulated velocity, and the corresponding velocity vectors would be lower than the current conditions and more uniform across the channel. The channel still would be considered mobile, but the potential for scour would be reduced due to the lower shear-stress values. Without guide banks of sufficient length on both banks, it is still possible for the approach channel to be misaligned relative the bridge opening and scour of the approach to continue despite the increased length of the bridge opening.

References Cited

- Barton, G.J., McDonald, R.R., Nelson, J.M., and Dinehart, R.L., 2005, Simulation of flow and sediment mobility using a multidimensional flow model for the white sturgeon critical-habitat reach, Kootenai River near Bonners Ferry, Idaho: U.S. Geological Survey Scientific Investigations Report 2005-5230 64 p.
- Brabets, T.P., 1997, Geomorphology of the Lower Copper River, Alaska: U.S. Geological Survey Professional Paper 1581, 89 p.
- Julien, P.Y., 1998, Erosion and sedimentation: Cambridge University Press, 280 p.
- McDonald, R.R., Bennett, J.P., and Nelson, J.M., 2006, Multi-dimensional surface water modeling system user's guide: U.S. Geological Survey Techniques and Methods Report, book 6, section B, chapter 6, 156 p., accessed at http://wwwwbrr.cr.usgs.gov/gst1/WebHelp_Pro/MD_SWMS.htm
- Nelson, J.M., and McDonald, R.R., 1997, Mechanics and modeling of flow and bed evolution in lateral separation eddies, Glen Canyon Environmental Studies Report, 69 p.

Assessment of Scour Development at a Deep-Water Marine Jetty Using 3d Computational Fluid Dynamics

Richard J.S. Whitehouse¹ and Sébastien E. Bourban¹

¹ HR Wallingford, Howbery Park, Wallingford, Oxfordshire, OX10 8BA, UK.
Email: r.whitehouse@hrwallingford.co.uk, s.bourban@hrwallingford.co.uk
Tel: +1491 835381

ABSTRACT

To assess the interaction of the tidal flow with a deep-water marine jetty, Computational Fluid Dynamics (CFD) was used to predict flow patterns for fast flood and ebb tide conditions both without and with the jetty in place. The modelled area covered three square kilometres of coastal bathymetry around the jetty head, with pile diameters of the order of one metre and water depths ranging from 3 m to 45 m. The predicted changes in velocity and bed shear stress distribution were used to explain the observed local bed level changes at this site over a period of three years.

INTRODUCTION

To understand the interaction of strong tidal flow with a deep-water jetty structure, an analysis of the current patterns was completed with a three dimensional Computational Fluid Dynamics (CFD) model. This paper describes an assessment of the modelling and comparison with the seabed changes. To take account of the local influences and to cover the far field, the modelled area covered three square kilometres. Detailed bed level surveys were carried out before construction of the jetty was started and once it was completed, and has shown changes. This paper describes the modelling approach, the observed bed level changes, and the analysis of the flow and bed shear stress distributions. The model results provide a systematic basis for understanding the observed bed level changes at the jetty site.

THE JETTY AND THE MARINE ENVIRONMENTAL CONDITIONS

The 2.5 kilometre long jetty is supported by circular steel piles of varying diameter with vertical and raker piles (varying between 1.2 m and 1.4 m diameter) at various angles and orientations (Figure 1). The T-head is 2.5 km from the shore and the seawards 0.25 km is situated in deep water with a water depth to mean tide level of 21.6 m. The bathymetry before jetty construction is shown in Figure 2.

Tidal current data offshore of the jetty head during construction showed that the flood tide currents at the surface can reach speeds of 2.8 ms^{-1} , or higher, and that the ebb tide currents can be as large as 1.75 ms^{-1} . Figure 3 shows the nature of the flood tide flow interaction with the mooring dolphins and the generation of turbulent wakes. As expected depth-averaged flows were somewhat smaller than the surface values. The duration of the flood and ebb tide streams are approximately equal and hence the tide has a marked flood-ebb asymmetry (flood/ebb ratio = 1.6). The directions of the near surface current vectors are aligned slightly offshore on the north going flood and slightly inshore on the ebb. Representative values of water density and kinematic viscosity are 1023 kgm^{-3} and $0.956 \cdot 10^{-6} \text{ m}^2\text{s}^{-1}$, respectively.

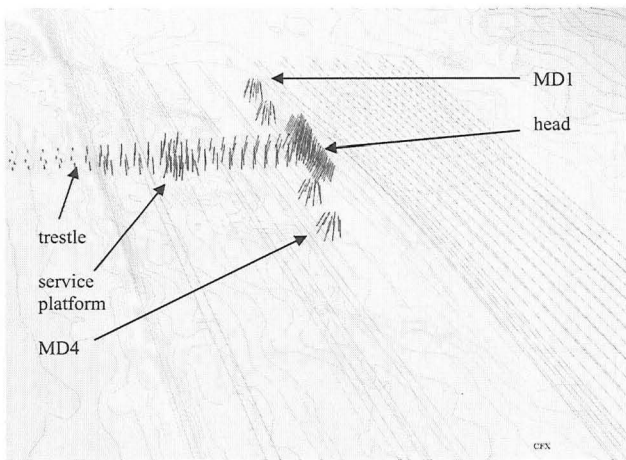


Figure 1. Jetty pile layout showing trestle, service platform, jetty head, and the four pile clusters for the mooring dolphins (MD1 to 4). Modelled flood tide streamlines are shown passing from top to bottom of the figure.

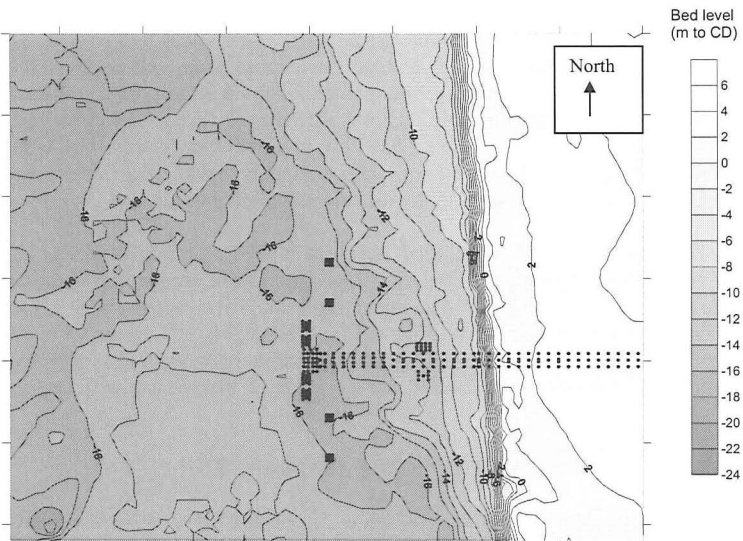


Figure 2. Seabed bathymetry in metres below Chart Datum pre-construction survey – axes tick-marks at 100 m intervals and future installed pile locations shown.



Figure 3. Tidal flow around mooring dolphins at the jetty (flow from right to left).

Sediment mobility

The sediment was loose to medium dense and dense, dark brown/grey, slightly silty to very silty, fine sand. The typical near surface particle size distributions from borehole analysis for the 10th, 50th and 90th percentile grain sizes were 0.08 mm, 0.17 mm and 0.25 mm, respectively, and the median grain size d_{50} was uniform in the top 10 m of the core. The threshold depth-averaged tidal current speed for sediment movement was 0.44 ms^{-1} and hence tidal flow produces strong transport. Since the duration of the flood and ebb flow is approximately equal, the flow asymmetry produces a net sediment transport in the direction of the flood tide.

Bedforms at the jetty included large sandwaves and smaller, irregular, bed waves, furrows and ripples, with the sandwaves indicating predominantly northward transportation of sediments; in agreement with the flow asymmetry. The larger sandwaves had wavelengths of 80 m to 120 m and heights of 1 m to 2.5 m and the sandwave field extended in the flood current direction away from the jetty axis. The post-construction survey also showed the presence of sandwaves with the jetty in place.

OBSERVED SEABED MORPHOLOGICAL CHANGES

The pre-construction survey (Figure 2) showed the seabed contours were sinuous and quite closely spaced in the jetty area and oriented closely parallel to the tide axis. There was a localised depression in the seabed at the proposed location of the jetty head (the positions of the jetty piles at trestle level are marked in Figure 2). A post-construction survey taken three years later provided a comparable coverage apart from close in to the jetty where it was more difficult to manoeuvre the survey vessel. The survey showed significant changes in the seabed in the vicinity of the jetty.

The analysis of bed level changes was undertaken using SURFER™ (see Figure 7). The changes that have taken place were characterised by overall erosion (deepening) of the seabed, by around 2 m to 3 m offshore of the jetty, and a localised pattern of erosion under and around the jetty trestle. The areas of erosion were in a zone north (downstream in the flood tide direction) of the jetty trestle, to a maximum total scour depth of 9.5 m, and an area adjacent to the jetty head, to a maximum total scour depth of 8.5 m; including changes that would have occurred naturally in seabed levels. In contrast there is also an area downstream of the jetty head in the flood tide direction where the bed level change was negligible, and hence siltation was understood to have taken place.

COMPUTATIONAL MODELLING

The mathematical Computational Fluid Dynamics (CFD) code CFX-5™ from AEA Technology (now with ANSYS) was used and the submerged elements of the jetty were represented. The model was filled in with a 3D-mesh of combined tetrads, pyramids and prisms of variable sizes depending on the place of interest. The mesh size varied from 0.5 m wide per element in the proximity of the jetty to 40 m away from the jetty. The mesh was refined around the piles, at the seabed and at the submarine slope. A 0.1 m thick layer of prisms was used adjacent to the seabed to enable a good representation of the friction/turbulent boundary condition. The flow structure and associated turbulence in 3-dimensions was achieved using a $k-\epsilon$ turbulence closure as this offered the best compromise between complexity and run time considerations over the large area that was to be modelled. Because of the deep water a rigid-lid assumption was made and the emphasis placed on obtaining the flow distribution and turbulent stresses near the seabed. On the seabed, the turbulent layer was modelled through a friction law calculation using a bed roughness length of 6 mm. This value is appropriate for rippled sand (Soulsby, 1997). The hydraulic roughness of the steel piles was simulated with the default material value in CFX.

The jetty was placed within an accurate representation of the pre-construction seabed bathymetry over the whole model domain. The water depth varied from 3 m in the shallow eastern area to 45 m in the offshore part of the model domain (Figure 2). The area covered by the model domain extended 2 km from north to south and 1.5 km from east to west. The size of the computational domain was chosen so that the boundaries were sufficiently far from the jetty such that flow in and around the jetty was free from any boundary wall effects.

Tidal scenarios

Boundary conditions were set in order to obtain the required peak velocity at the head of the jetty. Firstly, an incoming mass flow rate was calibrated for both the ebb and the flood scenarios, and secondly a spatially variable velocity profile was set according to the calibrated mass flow and the bathymetry. The profile was weighted with the square root of the local water depth, which is a common approximation used in hydrodynamic modelling of coasts and estuaries. The predicted flow speeds and headings at the jetty head were close to the observed values, i.e. speeds within 10% of the measured values. By comparing the results obtained for the model with the jetty with those for the model without the jetty, using similar mesh geometry, the influence on the flow could be determined directly.

MODEL RESULTS AND COMPARISON WITH OBSERVED BED LEVEL CHANGES

General considerations with and without the jetty

The submarine slope and the gradual rise in the bathymetry beyond the jetty in the flood tide direction exert a controlling influence on the flow, e.g. see flood tide streamlines in Figure 1 and flow vectors in Figure 4. The presence of the jetty and its variable structure density impart non-uniformity on the pattern of velocity and shear stress.

With the jetty in place, on the ebb flow, the water flow was parallel to the jetty head offshore from the service platform, and at a slight angle under the approach trestle where there was local acceleration around and through the piles. Also there was acceleration of the flow inshore of the control room. On the flood tide there was a marked deviation of the flow direction immediately offshore of the jetty head and acceleration in the flow (Figure 4). The flow velocity is considerably reduced to the lee of the service platform, the mooring dolphins and the control room. There is local flow acceleration around and through the trestle between these structures and zones of shear generating turbulence.

The gradual rise in the bathymetry north of the jetty (Figure 2) produced a vertical contraction of the flow under flood conditions and extension under ebb conditions. As a result, the velocity and, therefore, the shear stress north of the jetty alignment are greater on the flood tide than on the ebb tide. In addition, as the flow speed on the flood tide was much larger than the ebb, and this translates to the shear stress acting on the seabed, there was an asymmetric pattern in the flood and ebb flow fields, turbulence, shear stresses and associated sediment transport.

Flood flow with and without the jetty

In terms of near-bed velocity profiles the most significant influence is the appearance of two shadow areas in lee of the jetty head and mooring dolphins 3 and 4 and the service platform piles. The results obtained for the flood conditions with and without the jetty at the offshore (open) and incoming flow boundaries are similar. The influence of the jetty on bed shear stresses is noticeable around the head and north of the jetty (Figure 5).

In addition to creating shadow areas, the jetty tends to decelerate the approaching flow, redirecting it offshore (Figure 1). As a result, the northwards increase in shear stress values produced by the gradual rise of the bathymetry is diminished since less flows pass through the jetty structure. However, two bands of high velocity, turbulent shear and shear stress are evident (1) extending to the north of the trestle between the service platform and the control room, and (2) between the control room and the toe of the submerged cliff.

Finally, adjacent to the jetty head just offshore, the surface velocity profile has been greatly altered. A strong acceleration in the surface and nearbed flow is predicted with non-symmetry to the north (adjacent to mooring dolphins 3 and 4). This zone of acceleration on the flood tide occurs at a similar location to that produced on the ebb (not shown).

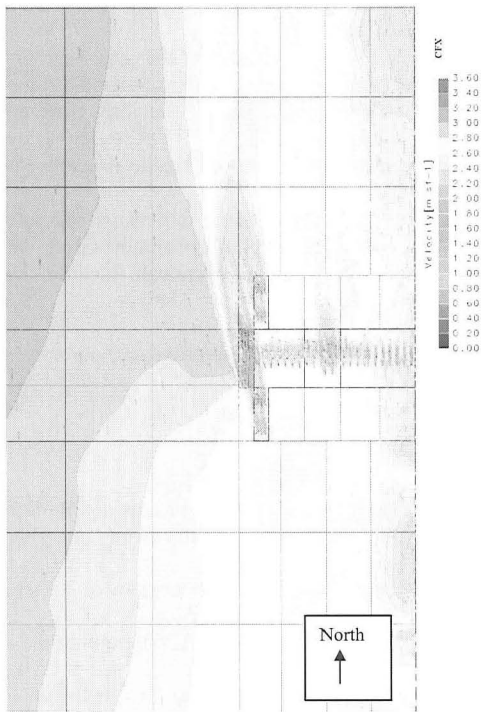


Figure 4. CFX model output for surface current speed contoured with some vectors in m s^{-1} on flood tide.

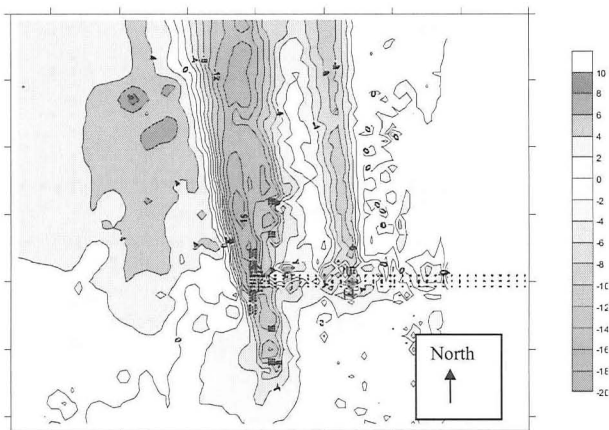


Figure 5. Difference in bed shear stress Nm^{-2} on flood tide (axes tick-marks 100 m spacing).

In terms of shear stress profiles (see Figure 5), the jetty produces four areas of influence (positive values are increased):

- An area of increased shear stress, offshore of the jetty head and increasing in a north northwesterly direction, and inshore of the service platform
- An area of decreased shear stress, north of the jetty head and of the service platform (due to the flow shadow areas)
- An area of decreased shear stress south of the trestle structure (due to deceleration of the approach flow)
- An area of relative decrease in shear stress, in between the service platform and the jetty head and between the service platform and the coast. However, the value of bed shear stress in this area is still high enough to cause significant sediment transport

On the ebb tide similar, but less strong patterns were observed in terms of near-bed velocity distributions.

DISCUSSION

Assessment of flow sheltering and "blockage" effects

The influence of the jetty on the bed shear stress distribution has been shown in Figure 5. Considering the influence for both flood and ebb, there are three observations that can be made:

- There is an increase of the velocity field (therefore of the shear stress) at the offshore side of the jetty head
- Mooring dolphins 3 and 4 are exposed to the full strength of the tidal flow on both flood and ebb
- Mooring dolphins 1 and 2 and the jetty head tend to shelter each other depending on the direction of the flow

Considering the differences between flood and ebb tides, the ebb flow passes through the structure while the flood flow tries to avoid the structure. This is caused by the differences in flow speed and the "blockage" to the flow provided by the jetty. The slight variations in the flood and ebb flow directions combine with the orientation of the pile rows under the jetty head to provide a lower degree of blockage on the ebb tide than the flood tide.

Sediment transport and scour

Sediment transport is related to a high power of the velocity or shear stress (usually 3 to 5 for velocity or 2 to 3 for shear stress, Soulsby 1997). The outcome is that in any unit area of the seabed where the flow is accelerating and transport increasing there will be a tendency for net erosion of the seabed (scour) (Whitehouse, 1998). The opposite effect will be evident if the flow is decelerating (i.e. deposition). The flow, sediment and water depth control the sediment transport, and the structure interaction dictates the way in which the sediment transport deviates from the without-jetty case and how any scour develops.

Tidal asymmetry

The asymmetry in flood and ebb quantities can be interpreted as causing net sediment transport in either the flood or ebb direction (assuming the duration of both

phases of the tide are comparable). When the ratio of peak flood velocity to ebb velocity is larger than 1 this indicates sediment transport is greater in the flood direction, whereas when the ratio is less than 1 then the net transport is in the opposite direction. Prior to the jetty being constructed the ratio (at the site of the jetty head) was predicted as lying between 1.6 and 1.7. The ratio increased rapidly towards the toe of the submerged cliff (values of at least 2.6), indicating that tidal asymmetry was more pronounced in the shallower water.

With the jetty in place the flood-ebb asymmetry adjacent to the jetty head still retains a value of 1.6 but varies spatially in a more complex fashion (Figure 6). The ratio of flood-ebb currents becomes as high as 2.0 in a band running north north-west away from the jetty head and is reduced to much less than 1 in the shadow zone to the north of the jetty head and mooring dolphins 3 and 4. To the south of the service platform and berthing dolphins 1 and 2 the ratio is larger than 3. These changes from the pre-jetty situation will lead directly to local variations in the magnitude and direction of net sediment transport around the jetty.

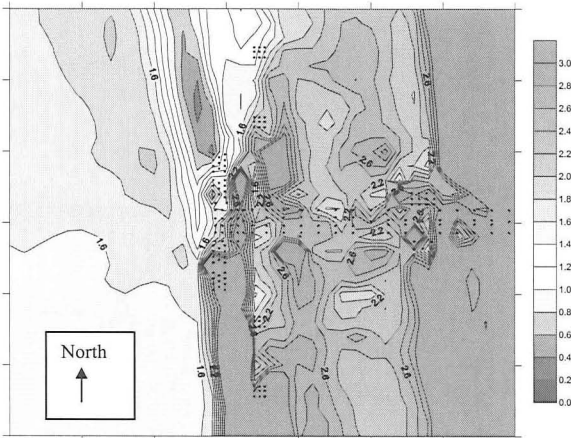


Figure 6. Flood-ebb velocity asymmetry with the jetty in place: Ratio of computed near bed velocity on flood tide to near bed velocity on ebb tide (axes tick-marks 50 m spacing).

Interpreting the scour development

The modelled interaction of the flow with the jetty helps explain the detailed evolution of the bed in the areas where local scour has been observed and where reduced rates of erosion have taken place. The model results discussed above have been used to produce the interpretation diagram presented in Figure 7. The scour depth immediately around the piles was not measured but it is the global scour that was being assessed with both the survey results and the computational modelling. The change in bed level well away from the jetty, in particular offshore to the west, are likely to result from natural tidal processes. It is the combined effect of the regional and local change that causes the observed pattern of change. Part of the local scouring observed to the north of the jetty could result from the reduction in height of

the bedforms observed in this area or a shift in the boundary between small and large sandwaves.

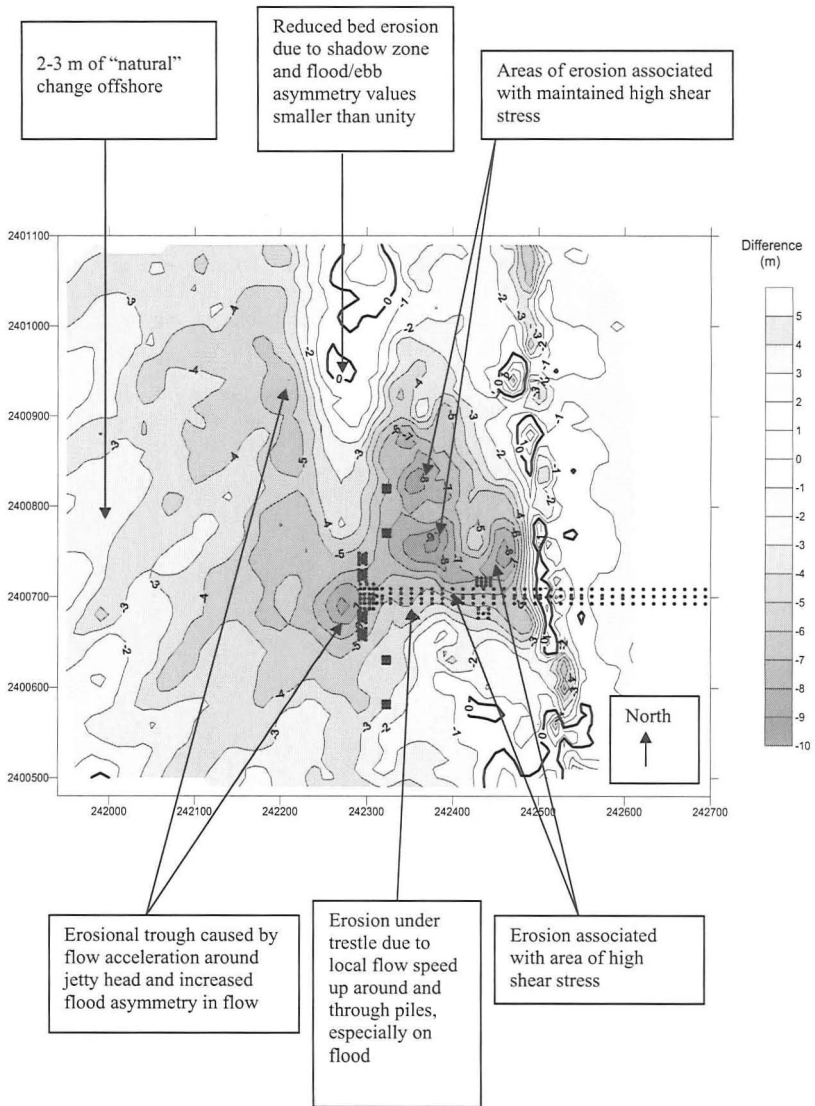


Figure 7. Interpreted bed level changes (post minus pre-construction levels) based on assessment of computational model results (local coordinate axes tick-marks 100 m spacing).

The mechanisms contributing to the observed bed level change arise from (1) local scour associated with the jetty structure, (2) lanes of fast flow and turbulence generation downstream of the jetty in the flood tide direction combined with the locally strong flood velocity asymmetry, causing (3) enhanced sediment transport and the migration of sandwaves over the seabed, and (4) regional scale erosion and deposition of sedimentary material which takes place naturally.

CONCLUSIONS

The CFD modelling approach described in this paper provides a flexible method and the high level of detail required when assessing the interaction of flows with complex piled marine structures. A detailed mesh was used to represent the main features of the pile array set within an accurate representation of the pre-construction seabed bathymetry. The model was set up with boundary conditions to represent the spatial and vertical distribution of steady-state peak flood and ebb tidal flow fields. The resulting flow speed and direction adjacent to the jetty head was compared with site measurements and found to be acceptable for the present assessment; predicted speed was within 10 % of the measured value

Analysis of bathymetric survey data has shown local changes in seabed level around the jetty, with total maximum scour depths to the lee of the jetty on the flood tide of up to 9.5 m in three years and areas of siltation too. The CFD model was run both without and with the jetty in place to determine the flood and ebb tidal flow fields, turbulence and associated bed shear stresses. The nearbed velocity and shear stress are the driving force for sediment transport, and the changes in the pattern of these quantities directly informs the interpretation of the patterns of seabed scour and accretion. The development of the seabed scour pattern around the jetty could be explained from the pattern of flow, turbulent shear and bed shear stress with the jetty in place, and also the predicted asymmetry in flood-ebb flow speeds.

For other projects where complex piled structures are being considered for active sediment transport environments it is concluded that three-dimensional CFD modelling will provide a good diagnostic tool to assess the bed changes that will occur. Direct prediction of the depth of scour at these types of structures will require additional modelling effort and research.

ACKNOWLEDGEMENTS

The material in this paper was published with kind permission of Skanska, Maple Cross, UK. Our colleagues Tom Stevenson and David Robinson plotted model results, and John Baugh reviewed the draft version of this paper. The reviewers provided useful comments which we have addressed.

REFERENCES

- Soulsby, R.L. (1997). *Dynamics of Marine Sands*. Thomas Telford Publications. 250 p.
- Whitehouse, R.J.S. (1998). *Scour at Marine Structures*. Thomas Telford Publications. 216 p.